

**© Copyright 2008**

**Steven Lawrence Miller**

**All Rights Reserved**

**TOWARDS ROOM TEMPERATURE PROCESSED AND COMPLETELY  
FLEXIBLE ORGANIC PHOTOVOLTAICS**

By

STEVEN LAWRENCE MILLER

A dissertation submitted to the Graduate School-New Brunswick

Rutgers, The State University of New Jersey

In partial fulfillment of the requirements

For the degree of

Doctor of Philosophy

Graduate Program in Material Science and Engineering

Written under the direction of

Prof. Manish Chhowalla

And approved by

---

---

---

---

---

New Brunswick, New Jersey

May, 2008

## ABSTRACT OF DISSERTATION

Towards Room Temperature Processed and Completely Flexible Organic Photovoltaics

By STEVEN LAWRENCE MILLER

Dissertation Director: Prof. Manish Chhowalla

This thesis presents the work towards identifying and developing materials and processes necessary to fabricate inexpensive, flexible and room temperature processed organic photovoltaic devices (OPVs). A method for rapidly fabricating and characterizing OPVs utilizing gallium-indium eutectic (liquid at room temperature) to replace thermally evaporated aluminum and a simple halogen light as a replacement for a solar simulator is described. Poly(3-hexylthiophene):phenyl-C<sub>61</sub>-butyric acid methyl ester (P3HT:PCBM) bulk heterojunctions were utilized for absorbing light and generating charge carriers. P3HT:PCBM OPVs using traditional transparent and conducting materials for carrier collection such as indium tin oxide (ITO) coated glass and fabrication processes such as thermal annealing were optimized. Thermal annealing is an integral step in developing the morphology necessary to create high efficiency OPVs, but is detrimental to many flexible (plastic) substrates. In order to overcome this limitation, a technique utilizing room temperature solvent vapor annealing for improving OPV efficiency was developed and the mechanisms leading to such improvement are elucidated through *in situ* and *ex situ* characterization. The analyses revealed that solvent vapor annealing at room temperature leads to comparable changes in morphology and charge transport as thermal annealing.

ITO is expensive and substantially loses conductivity when flexed. As an alternative, single walled carbon nanotube (SWNT) thin film as a transparent and

conducting material was investigated. Using a solution of dispersed SWNTs, networks with densities just above the metallic percolation threshold were deposited with conductivity and transmission properties comparable to ITO. Additionally, they are flexible without a loss in conductivity with bending cycles. OPVs with SWNT thin films as the hole collecting electrodes showed better performance than ITO reference cells. The mechanism for the better performance was attributed to the three dimensional interface between the P3HT:PCBM and the SWNTs which allows efficient capture of holes. The presence of birefringence in SWNT thin films and its influence on OPV properties as a function of angle of illumination is also described. The results presented in this thesis should lead to a better understanding of the P3HT:PCBM system and demonstrate promising solutions towards the realization of flexible, room temperature processed and inexpensive OPVs.

## ACKNOWLEDGEMENTS

I would like to thank my advisor, Prof. Manish Chhowalla, for suggesting research in organic photovoltaics in the first place, and for his help and advice during the last three and a half years. I would also like to thank my co-advisor, Prof. Aurelien Du Pasquier, who taught me the mechanics of laboratory research.

I would further like to thank all of the members of the Nano-materials and Devices Group at Rutgers University for their help. I am indebted to Dr. Giovanni Fanchini who gave me much insight into the physics of disordered systems and taught me to adapt the knowledge learned elsewhere to the work at hand. I owe a special thanks to Dr. Alokik Kanwal for his great friendship, help and suggestions during the entire process. He kept me grounded during the difficult times. I would also like to thank Dr. H. Emrah Unalan for his friendship, help and suggestions.

I am grateful to all of the other fellow graduate students, post-docs, undergraduates and faculty of Rutgers University who assisted me in the process and with whom I had the opportunity to work and spend time with. I enjoyed the discussions about the research projects and beyond.

I would like to express my appreciation to Sheri Fabian for her editorial skills and for proofreading the thesis.

Finally, I must thank my family for their support during this endeavor. Especially, I want to thank my wife, Christine, who was so supportive of my life changing decision to pursue graduate studies at Rutgers.

## Table of Contents

Abstract of Dissertation .....	ii
Acknowledgements .....	iv
Table of Contents .....	v
List of Tables .....	x
List of Figures .....	xi
Chapter 1 Introduction to Organic Photovoltaics .....	1
1.1 Motivation and Background .....	1
1.2 Organic Photovoltaic Devices .....	4
1.2.1 The Solar Spectrum .....	6
1.2.2 Conjugated Polymers .....	7
1.2.3 Physics of Organic Photovoltaic Devices .....	10
1.2.4 Solar Cell Characteristics .....	16
1.2.4.1 Power Conversion Efficiency .....	16
1.2.4.2 Open-Circuit Voltage .....	17
1.2.4.3 Short-Circuit Current .....	18
1.2.4.4 Fill Factor .....	20
1.2.4.5 External Quantum Efficiency .....	20
1.2.5 Band Structure .....	21
1.3 Content of this Thesis .....	24
1.4 References .....	26

## Chapter 2 Development of an Inexpensive Method to Rapidly Test Organic

Photovoltaic Devices .....	29
2.1 Introduction.....	29
2.2 Structure and Materials of P3HT:PCBM Organic Photovoltaics .....	31
2.3 Fabrication and Testing of Devices .....	34
2.3.1 Ga-In Electrodes .....	34
2.3.2 Halogen Lamp for Simulated Solar Spectrum .....	34
2.4 Results and Discussion .....	37
2.4.1 Light Intensity and Spectral Mismatch Correction.....	37
2.4.2 <i>In situ</i> Thermal Annealing and Efficiency Change Monitoring .....	42
2.4.3 Optimal P3HT: PCBM Ratio .....	46
2.4.4 Comparing the Efficiencies Measured with a Halogen Light Source and with an A.M. 1.5 Solar Simulator .....	48
2.4.5 Comparison of Evaporated Aluminum versus Ga-In Electrodes.....	50
2.5 Conclusion .....	51
2.6 References.....	52

## Chapter 3 Investigation of Nanoscale Morphological Changes in Organic Photovoltaics

during Solvent Vapor Annealing .....	54
3.1 Introduction.....	54
3.2 Characterization Techniques.....	56
3.2.1 Raman Spectroscopy.....	57
3.2.2 Photoluminescence .....	60
3.2.3 UV-Vis Spectroscopy .....	61

3.2.4	Atomic Force Microscopy .....	62
3.3	Experimental Details.....	65
3.4	Results.....	70
3.4.1	Photovoltaic Efficiencies .....	70
3.4.2	UV-Vis Spectroscopy .....	72
3.4.3	Atomic Force Microscopy .....	75
3.4.4	Photoluminescence .....	76
3.4.5	Raman Spectroscopy.....	81
3.5	Discussion.....	84
3.6	Conclusions.....	86
3.7	References.....	87
Chapter 4 Single Walled Carbon Nanotube Thin Films as Transparent and Conducting		
Electrodes in Organic Photovoltaic Devices.....		90
4.1	Introduction.....	90
4.2	Single Walled Carbon Nanotubes.....	91
4.3	Review of Single Walled Carbon Nanotube Thin Films .....	101
4.3.1	Purification of SWNTs .....	102
4.3.2	Preparation of SWNT Thin Films.....	105
4.3.3	Characterization of SWNT Thin Films.....	108
4.4	SWNT Thin Films as Transparent and Conducting Electrodes in OPVs .....	115
4.5	Birefringence in SWNT Thin Film OPVs .....	122
4.6	Hole Mobility.....	127
4.7	Conclusions.....	132



4.8	References.....	133
Chapter 5 Conclusions and Future Work.....		136
5.1	Conclusions.....	136
5.2	Suggestions for Future Research .....	139
Appendix A Tauc Method for Optical Band Gap Measurements.....		142
A.1	Tauc Gap and Tauc Plot.....	142
A.2	References.....	145
Appendix B Mott-Gurney Square Law (Child's Law for Solids).....		146
B.1	Derivation of the Mott-Gurney Square Law .....	146
B.2	References.....	148
Appendix C Procedures for the Fabrication and Characterization of P3HT:PCBM Organic Photovoltaic (OPV) Devices.....		149
C.1	Fabrication of P3HT:PCBM OPVs.....	149
C.1.1	Cleaning and Preparation of the Substrate and Bottom Contact.....	149
C.1.2	P3HT:PCBM Solution Preparation and Deposition .....	150
C.1.3	Evaporation of Top Contact.....	152
C.2	Characterization of P3HT:PCBM OPVs .....	152
Appendix D Equipment and Apparatus .....		155
D.1	Solar Simulator .....	155
D.2	Current Meter/DC Voltage Source .....	156
D.3	Thermal Evaporator .....	157
D.4	External Quantum Efficiency Apparatus.....	158
D.5	Glove Box .....	159

D.6 Atomic Force Microscope.....	160
Curriculum Vita .....	161

## List of Tables

<b>Table 2.1</b> Efficiencies before and after annealing and optimal annealing temperatures as a function of type of solvent, P3HT:PCBM composition and spin coating speed.	43
<b>Table 2.2</b> Photovoltaic parameters efficiency ( $\eta$ ), fill factor (FF), short-circuit current ( $I_{sc}$ ) and open-circuit voltage ( $V_{oc}$ ) of P3HT: PCBM solar cells at various P3HT: PCBM ratios, measured under 100 mW/cm <sup>2</sup> halogen white light, with Ga-In top contact.....	48
<b>Table 2.3</b> Photovoltaic parameters efficiency ( $\eta$ ), fill factor (FF), short-circuit current ( $I_{sc}$ ) and open-circuit voltage ( $V_{oc}$ ) of the same P3HT: PCBM solar cell, measured under 100 mW/cm <sup>2</sup> halogen white light or 100 mW/cm <sup>2</sup> A.M. 1.5 solar simulator.....	49
<b>Table 2.4</b> Photovoltaic parameters efficiency ( $\eta$ ), fill factor (FF), short-circuit current ( $I_{sc}$ ) and open-circuit voltage ( $V_{oc}$ ) of the same P3HT: PCBM solar cell, measured under 100 mW/cm <sup>2</sup> A.M. 1.5 solar simulator, using either an Al or Ga-In top contact.....	51
<b>Table 3.1</b> Summary of optical bandgaps for P3HT:PCBM composite thin films before and after solvent vapor annealing using the Tauc method and the $E_{04}$ values.....	74
<b>Table 4.1</b> Solar cell parameters at 100 mW cm <sup>2</sup> illumination for the reference cell on ITO-PET substrate and the best solar cell on SWNT-glass substrate.....	120
<b>Table 4.2</b> Hole mobilities for P3HT:PCBM with SWNT network electrodes and ITO reference electrodes. ....	131

## List of Figures

<b>Figure 1.1</b> The basic device structure of organic photovoltaics. Indium Tin Oxide (ITO) acts as a transparent and conducting electrode. ....	3
<b>Figure 1.2</b> A two-layer heterojunction device. Charge transfer occurs at the donor/acceptor interface.....	5
<b>Figure 1.3</b> The standard Air Mass 1.5 (AM1.5) global solar spectrum. <sup>16</sup> .....	7
<b>Figure 1.4</b> Schematic diagram of $\sigma$ and $\pi$ bonds in trans-polyacetylene, showing $p_z$ orbitals which overlap to provide the $\pi$ bonds. <sup>17</sup> .....	8
<b>Figure 1.5</b> Illustration of the semiconducting conjugated polymer P3HT. The red line shows the alternating single and double bonds of the conjugated backbone.....	9
<b>Figure 1.6</b> Exciton dissociation at the donor-acceptor interface. The electron goes to the acceptor while the hole stays on the donor. <sup>25</sup> .....	11
<b>Figure 1.7</b> Illustration of $C_{60}$ and [6,6]-phenyl $C_{61}$ -butyric acid methyl ester (PCBM), which are used as acceptor molecules in bulk heterojunction photovoltaic devices. ....	12
<b>Figure 1.8</b> (a) Photovoltaic device with a nanostructure/polymer active layer. The enlarged region shows the separation and subsequent transport of carriers. (b) Energy diagram of the nanocomposite indicating that the carriers can separate if the exciton binding energy is lower than the difference in electron affinity ( $\Delta E_a$ ) between the two materials.....	13
<b>Figure 1.9</b> Band structure and charge carrier movement of P3HT:PCBM device under short-circuit conditions. The open-circuit voltage ( $V_{OC}$ ) of this device is the energy difference between the HOMO level of the P3HT and the LUMO level of the PCBM...	15
<b>Figure 1.10</b> Diagram showing current-voltage curve of photovoltaic device, including the following parameters: short circuit current ( $I_{SC}$ ), open circuit voltage ( $V_{OC}$ ), maximum power point current ( $I_{MPP}$ ), and the maximum power point voltage ( $V_{MPP}$ )....	16
<b>Figure 1.11</b> Schematic showing variation of $V_{OC}$ . $V_{OC1}$ shows the difference between the HOMO level of the donor and the LUMO level of the acceptor. $V_{OC2}$ shows the difference between the work functions of the electrodes.....	18
<b>Figure 1.12</b> Graph of measured EQE or IPCE for a pristine and a thermally annealed P3HT:PCBM photovoltaic device. ....	21
<b>Figure 1.13</b> The MIM model of the current-voltage characteristics under different working conditions. Under (a) open circuit, the $V_{OC}$ is equal to the difference between the work functions of the electrode, (b) short-circuit, holes are transported to the anode	

and electrodes to the cathode, (c) reverse bias the diode functions as a photodetector, and (d) forward bias the diode can function as a light emitting diode.....	23
<b>Figure 2.1</b> Schematic of P3HT:PCBM organic photovoltaic device.....	33
<b>Figure 2.2</b> Schematic of apparatus constructed for testing P3HT:PCBM photovoltaic devices using Ga-In eutectic as the top electrode and a halogen lamp as the solar simulator. The heat from the light source allows for testing and <i>in-situ</i> thermal annealing .....	36
<b>Figure 2.3</b> Absorption spectrum of P3HT:PCBM (ratio=1:1) layer spin-coated on glass, spectral output of the halogen light source used to test them, and AM 1.5 solar spectrum. ....	38
<b>Figure 2.4</b> Fill factor versus short-circuit current of a P3HT:PCBM 1:1 photovoltaic device measured with a halogen light source. The arrows indicate the value of the short-circuit current measured in sunlight and the corresponding estimated fill factor. ..	39
<b>Figure 2.5</b> Log-Log plot of light intensity versus short-circuit current for P3HT: PCBM 1:1 solar cell measured with halogen light source. Uncorrected values of light intensity (dots) and corrected values (squares) intercepting data point in sunlight.....	41
<b>Figure 2.6</b> Repeated I-V cycles under 2400 W/m <sup>2</sup> white light annealing (A) and evolution of conversion efficiency (B) for same P3HT: PCBM 1:1 device spin coated from 10 g/L chloroform solution. ....	46
<b>Figure 2.7</b> I-V curves at various light intensities of ITO-PEDOT: PSS/P3HT: PCBM/In-Ga solar cells with P3HT: PCBM ratio of 2:1 (A), 3:2 (B) and 1:1 (C). ....	47
<b>Figure 2.8</b> I-V curves at 100 mW/cm <sup>2</sup> of simulated sunlight for the same ITO/PEDOT:PSS/P3HT:PCBM 1:1/Ga device measured with a halogen light source (—) or under A.M. 1.5 conditions (---).....	49
<b>Figure 2.9</b> I-V curves at 100 mW/cm <sup>2</sup> of A.M 1.5 simulated sunlight for the same ITO/PEDOT:PSS/P3HT:PCBM 1:1/Ga device measured with aluminum top contact (—) or Ga-In top contact (---).....	50
<b>Figure 3.1</b> Diagram shows the basic scattering process for a single vibration. The energy of Rayleigh scattered light is equal to the incident light. Stokes and anti-Stokes scattered light is less and greater, respectively, than the incident light by the difference between the ground and excited vibrational states. <sup>22, 23</sup> .....	58
<b>Figure 3.2</b> Raman spectrum of a P3HT thin film on a PET substrate. The characteristic Raman active bands of P3HT and the chemical bond(s) associated with their origin are indicated. <sup>24, 26</sup> Raman active bands of PET are indicated with an asterisk. <sup>27</sup> .....	60

<b>Figure 3.3</b> Schematic of atomic force microscope. Raster scanning of the tip and cantilever over a sample surface results in a topographical map of the sample with nanometer resolution.....	63
<b>Figure 3.4</b> Schematic of the experimental configuration used to perform solvent vapor annealing while simultaneously measuring the PL and Raman features.....	66
<b>Figure 3.5</b> Log-log plot of PL intensity vs. laser excitation power for P3HT:PCBM thin films. The red plots show a linear relationship between PL and laser power using 633nm (1.96eV) excitation (close to the P3HT bandgap). The blue plots show a sub-linear relationship using 785nm (1.57eV) excitation (less than the P3HT bandgap), suggesting PL is the result of defect mediated states.....	68
<b>Figure 3.6</b> Schematic of radiative recombination mechanism of polaron-exciton pairs into Franck-Condon (FC) states (adapted from Ref. <sup>29</sup> ). Changes in P3HT nuclear geometry upon excitation to the Franck-Condon excited state ( $S_1(FC)$ ) result in the formation of a new equilibrium excited state ( $S_1(eq)$ ) and the subsequent decay to $S_0(FC)$ resulting in PL are shown. The total difference between the equilibrium and Franck-Condon levels is the polaron-exciton correlation energy ( $2U$ ).....	70
<b>Figure 3.7</b> (a) Current density versus the voltage plot for P3HT: PCBM photovoltaic devices before (red squares) and after 2 minutes of solvent vapor annealing (blue circles). (b) External quantum efficiency (EQE) measurements for as deposited, solvent annealed and thermally annealed devices. ....	71
<b>Figure 3.8</b> (a) Comparison of absorption spectra of P3HT and P3HT: PCBM in solution and as deposited thin solidified films. (b) Comparison of absorption spectra of as deposited thin films and solvent vapor annealed thin films of P3HT and P3HT: PCBM. 73	
<b>Figure 3.9</b> (a) AFM height image of as deposited and (b) solvent vapor annealed P3HT: PCBM thin films. The z-range of images (a) and (b) are 6 nm and 11 nm respectively. (c) is a phase image of the P3HT:PCBM sample shown in (b). ....	75
<b>Figure 3.10</b> Combined PL and Raman spectroscopy results of pure P3HT and P3HT:PCBM before and after solvent annealing. The peaks marked with asterisks (*, **) correspond to PET and ITO, respectively. The $715\text{ cm}^{-1}$ , $1380\text{ cm}^{-1}$ and $1440\text{ cm}^{-1}$ Raman peaks indicated by squares are assigned to the P3HT C-S-C ring deformation, C-C skeletal stretching and C=C ring stretching, respectively. <sup>24</sup> .....	77
<b>Figure 3.11</b> (a) The sequence for determining the correlation energy ( $2U$ ) from the P3HT:PCBM PL peak is shown. The Raman peaks were manually removed from the broad PL spectrum and smoothing was performed. A Gaussian curve fit was obtained to identify the peak position. (b) The Gaussian fit of the PL peak for P3HT:PCBM before (black) and after (blue) solvent vapor annealing. The difference in the peak position is the change in $2U$ or $\sim 0.015\text{eV}$ .....	79
<b>Figure 3.12</b> Summary of the PL intensity versus the annealing time for pure P3HT and P3HT:PCBM.....	81

**Figure 3.13** (a) The 1350-1500  $\text{cm}^{-1}$  Raman region of P3HT and P3HT:PCBM devices before and after solvent vapor annealing. (b) Summary of the FWHM of the 1440  $\text{cm}^{-1}$  Raman C=C peak versus the annealing time for pure P3HT and P3HT:PCBM. .... 83

**Figure 3.14** Energy level diagram based on our measurements before and after solvent vapor annealing. The P3HT LUMO level shifts downward as indicated by the red arrows, increasing the possibility of electron transfer into PCBM and hole transfer into ITO, as indicated by the black arrows. .... 85

**Figure 4.1** Three allotropes of carbon: (a) graphite, (b) diamond and (c) single walled carbon nanotube. .... 92

**Figure 4.2** Schematics of single wall carbon nanotubes: (a) armchair, (b) zig-zag and (c) chiral.<sup>20, 21</sup> .... 93

**Figure 4.3** Relation between the hexagonal carbon lattice and the chirality of carbon nanotubes. The construction of a carbon nanotube from a single graphene sheet is shown. By rolling up the sheet along the wrapping vector C, that is, such that the origin (0,0) coincides with point C, a nanotube indicated by indices (11,7) is formed. Wrapping vectors along the dotted lines lead to tubes that are zigzag or armchair. All other wrapping angles lead to chiral tubes with wrapping angle specified relative to either the zigzag direction ( $\theta$ ) or to the armchair direction ( $\phi=30^\circ-\theta$ ). Dashed lines indicated by vector T are perpendicular to C and run in the direction of the tube axis. The solid vector H is perpendicular to the armchair direction and specifies the direction of nearest-neighbor hexagon rows, as indicated by the black dots. The angle between T and H is the chiral angle  $\phi$ .<sup>22</sup> .... 94

**Figure 4.4** Schematic of the structure of graphene unit cell (the areas within dashed borders) in real space (left) and reciprocal space (right).<sup>24</sup> .... 96

**Figure 4.5** (a) 3D energy diagram of graphene. The valence and conduction bands touch at the six points at the Fermi level called K-points. (b) Contour plot of the graphene valence states for a SWNT with zero chiral angle. Parallel lines are spaced  $2/D$  indicate  $k$  vectors allowed by the cylindrical boundary condition. Each line is a 1D subband. Lower energies are marked with red and higher energies are marked with blue.<sup>26</sup> .... 97

**Figure 4.6** Schematic of reciprocal space for (a) armchair, (b) zigzag and (c) chiral SWNTs. For (a) armchair SWNTs the K-lines are parallel in the  $k_y$  direction, always intersect the K-points and are thus always metallic. For (b) zigzag SWNTs the K-lines are parallel in the  $k_x$  direction, only intersect the K-points when the condition in Eq. 4.1 ( $n-m=3q$ ) is met and are metallic when this is the case. The K-lines for (c) chiral SWNTs have many orientations, will also intersect the K-points when the condition in Eq. 4.1 is met and are metallic in this case. The circular inset in (c) is enlarged in figure (d). It shows the relationship of allowed K-lines to Fermi level. The points of closest approach to K are  $K_1$  and  $K_2$ .<sup>24</sup> .... 99

<b>Figure 4.7</b> Electronic density of states for (a) (10,0) zigzag SWNT and (b) (9,0) zigzag SWNT. The SWNT represented in (a) shows a small energy gap between the first singularities with no density of states at the Fermi level and is thus semi-conducting, whereas (b) shows a finite density of states at the Fermi level and is thus metallic. The dotted line is the density of states for 2D a graphene sheet. <sup>23</sup> .....	100
<b>Figure 4.8</b> TGA curves for as received and purified HiPCO SWNTs showing that the catalyst content in the raw SWNTs is ~25% compared to being only ~2% after purification. Also, the decomposition temperature of purified SWNTs is higher. ....	104
<b>Figure 4.9</b> TEM images of HiPCO SWNTs (a) before and (b) after purification. <sup>26</sup> .....	105
<b>Figure 4.10</b> Image of the vacuum filtration apparatus used to prepare the SWNT thin films. <sup>26</sup> .....	107
<b>Figure 4.11</b> Schematic of the SWNT thin film deposition process. After filtration, the MCE membrane is covered with a glass slide and drying papers, compressively loaded and dried at 70 °C for at least 1 hour. The membrane is then dissolved in acetone and washed with methanol. The as-deposited films are dried with nitrogen prior to processing them for devices. <sup>26</sup> .....	108
<b>Figure 4.12</b> Scanning electron micrographs of SWNT thin films showing how different filtration volumes and SWNT concentrations affect the film density. <sup>26</sup> .....	109
<b>Figure 4.13</b> Plot of the relationship between the conductivity of various SWNT thin films and the relative volume fraction of the SWNTs. The curve is a fit using the percolation theory. <sup>26</sup> .....	110
<b>Figure 4.14</b> (a) UV-Vis and (b) transmission characteristics at $\lambda=550$ nm for SWNT thin films deposited from filtration volumes ranging from 10 mL to 60 mL with 2mg/L suspension. ....	112
<b>Figure 4.15</b> (a) SWNT thin film surface resistivity as a function of filtration volume and (b) SWNT thin film transmittance versus sheet resistance for the thin films in (a). ....	114
<b>Figure 4.16</b> Schematic of P3HT:PCBM OPV, with ITO (a) and SWNT thin film (b) as the hole collecting electrodes. ....	116
<b>Figure 4.17</b> (a) Efficiency, (b) fill factor (FF), (c) short-circuit current (I <sub>sc</sub> ) and (d) open-circuit voltage (V <sub>oc</sub> ) at various illumination intensities for P3HT:PCBM OPVs with SWNT thin films and ITO as a hole collecting electrode. ....	117
<b>Figure 4.18</b> I-V curves at 100mW/cm <sup>2</sup> halogen white light and in the dark of reference solar cell on ITO-glass and the best solar cell using a SWNT thin film. Log I-V characteristics are shown in the inset. ....	118
<b>Figure 4.19</b> Energy level diagram adjusted in relation to the vacuum level for the SWNT/PEDOT:PSS/P3HT:PCBM/Ga-In device. The arrows indicate hole and electron	



flows. <i>m</i> -SWNTs and <i>s</i> -SWNTs refer to metallic and semiconducting SWNTs, respectively. Energy diagram was constructed using References <sup>43-45</sup> .....	120
<b>Figure 4.20</b> SEM images of SWNT films deposited on Glass, from 50 ml SWNT solution (a) and 10 ml SWNT solution (b). The arrows on image (a) indicate the presence of voids that illustrate the three-dimensional nature of the coating. ....	121
<b>Figure 4.21</b> (a) Transmittance of ITO and SWNT thin films on glass as a function of the photon energy (E) at four incidence angles $\theta=0-70^\circ$ . (b) Angular dependency of the transmittances for ITO and SWNT thin films at $\lambda=550\text{nm}$ showing the cosine dependence of $\theta$ for SWNT thin films and independence of $\theta$ for ITO. ....	124
<b>Figure 4.22</b> Schematic of an OPV using ITO and a SWNT thin film as transparent electrode and the angular dependency of its transmission. ....	125
<b>Figure 4.23</b> Angular dependency of the relative efficiency ( $\eta$ ) of OPVs using SWNT thin film and ITO as a hole collecting electrode, plotted as (a) $\eta$ and (b) $\gamma = \eta/(\eta_0 \cos\theta)$ . ....	126
<b>Figure 4.24</b> Log-log plot of the J-V characteristics of hole injection P3HT:PCBM devices with the incorporation of SWNT networks on ITO and ITO only. ....	130
<b>Figure A.1</b> The dependence of $(\alpha\hbar\omega)^{1/2}$ on photon energy for P3HT:PCBM from which the optical band gap is estimated. The <i>x</i> -intercept of the fitted line gives the optical band gap of the material. ....	144
<b>Figure D.1</b> Newport solar simulator with AM 1.5 output up to $200 \text{ mW/cm}^2$ (2 suns). A special apparatus was fabricated and affixed to a goniometer to facilitate testing of OPV devices. ....	155
<b>Figure D.2</b> Hewlett Packard 4140B pA Meter/DC Voltage Source used to apply bias to and measure current across OPV devices under light and dark conditions. ....	156
<b>Figure D.3</b> Edwards 306A Coating System (thermal evaporator) used to deposit aluminum contacts on OPV devices. It should be noted that this equipment was not working when acquired. It was completely rebuilt and commissioned by the author as part of the work contained in this dissertation. ....	157
<b>Figure D.4</b> External quantum efficiency apparatus utilizes monochromatic light to measure the incident photon to current conversion efficiency by wavelength. ....	158
<b>Figure D.5</b> Nitrogen filled glove box used for the preparation of solutions, spin coating and annealing of OPV devices. ....	159
<b>Figure D.6</b> Digital Instruments Nanoscope IV atomic force microscope used to obtain height, amplitude and phase images of OPV device surfaces. ....	160

## Chapter 1

### Introduction to Organic Photovoltaics

#### 1.1 Motivation and Background

The late Professor Richard Smalley, Nobel Prize winner for the discovery of C<sub>60</sub>, argued that energy generation will be the most important technological challenge of this century. As the world's population reaches nearly ten billion by 2050,<sup>1</sup> the ability to provide clean water and food to developing communities will hinge on the ability to generate power locally. Further, decreasing oil reserves and unwanted greenhouse emissions have become driving forces behind the need for more “green” and renewable energy sources. A significant amount of research is currently devoted to the generation of energy through solar cells, a renewable energy source. The advantage of energy created through solar cells is that, unlike renewable energy from water or wind driven turbines, that require complex systems to convert mechanical energy to electrical energy, solar cells convert solar energy directly to electricity.

The most common form of solar cells are based on the photovoltaic (PV) effect in which radiation impinging on a two layer semiconductor device (usually a silicon p-n junction) induces a voltage between the layers, capable of driving a current through an external circuit. Power conversion efficiencies of up to 25% have been obtained for state-of-the-art single crystal silicon solar cells and over 40%<sup>2</sup> for multi-junction solar cells. However, these cells require energy intensive processing steps leading to relatively high production costs and high pay back periods.

On the other hand, solar cells based on organic materials can in principle be produced over large areas on inexpensive substrates using less energy intensive

methods such as printing, roll coating, or doctor blading. Thus, solution processed organic photovoltaics (OPVs) are promising as a source of affordable renewable energy. If indeed OPVs can be fabricated inexpensively, then the energy payback period is expected to be significantly less than for silicon and other inorganic solar cells such as copper indium gallium selenide, even at relatively low power conversion efficiencies. Presently, the state-of-the-art OPV cells have an efficiency of  $\sim 5\%$ <sup>3-5</sup>, with simulations indicating that efficiency up to  $10\%$ <sup>6</sup> is feasible. An increase in efficiency to  $10\%$  along with solution production processing provides a potentially cost effective alternative to their inorganic counterparts which require expensive vacuum and thermally intensive production techniques. An additional advantage of OPVs is that they are potentially light weight and flexible, allowing their use in wide ranging mobile applications.

There are challenges however that must be overcome before the full potential of these devices can be realized. For example, presently the OPV device consists of two inorganic electrodes: the transparent and conducting indium tin oxide (ITO) and the aluminum (Al) layer on top, as shown in Figure 1.1. Therefore, although the organic layer is flexible, the OPV device is not. Furthermore, although OPV devices can be fabricated on plastic substrates, thermal annealing of the devices up to  $150^{\circ}\text{C}$  is required to optimize the efficiency. However, heating of plastic substrates is detrimental for the lifetime of the devices. Our primary objective for the research conducted in this dissertation was to move towards a truly flexible OPV device processed entirely at room temperature. We attempted to achieve this by first replacing the ITO layer with a solution processed transparent and conducting single walled carbon nanotube (SWNT) thin film deposited at room temperature (Chapter 4). Secondly, we developed a room

temperature solvent vapor annealing method in place of the thermal annealing in order to enhance the efficiency of OPVs (Chapter 3). We demonstrate through *in-situ* and *ex-situ* analysis that solvent vapor annealing has the same consequences as thermal annealing for enhancing the transport of charge carriers and improving the absorption characteristics of the OPV device.

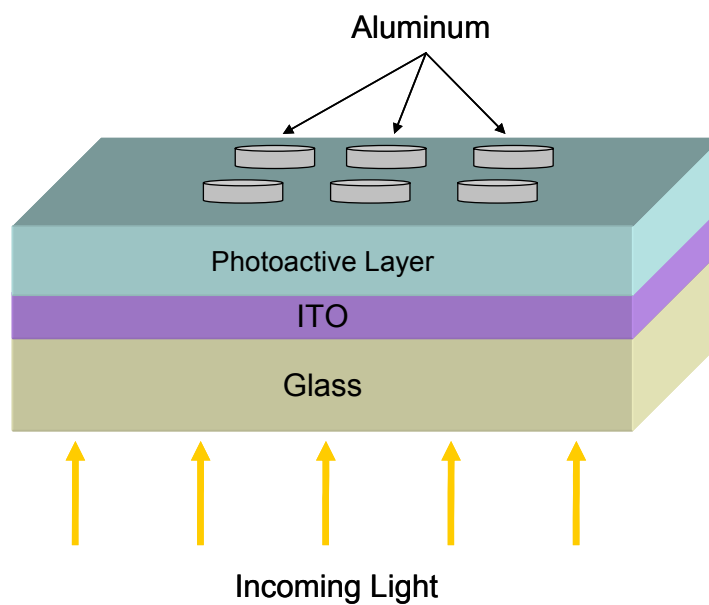


**Figure 1.1** The basic device structure of organic photovoltaics. Indium Tin Oxide (ITO) acts as a transparent and conducting electrode.

## 1.2 Organic Photovoltaic Devices

The foundation for a new class of polymeric optoelectronics had been established when it was discovered that the chemical doping of conjugated polymers could substantially improve their conductivity.<sup>7</sup> Tang<sup>8</sup> realized that charge separation at a heterojunction between an organic electron donor and acceptor through exciton dissociation should lead to a photovoltaic effect. Based on this, organic photovoltaic devices, with two conjugated organic layers (copper phthalocyanine and a perylene tetracarboxylic derivative) forming the heterojunctions, with power conversion efficiencies of approximately 1% were demonstrated.<sup>8</sup> Figure 1.2 shows a typical sandwich structure device, also called a two-layer heterojunction device, where an interface between a donor and acceptor material occurs. Although OPVs were realized with the bilayer device, several persistent limitations prevented a dramatic increase in efficiency. Specifically, since charge dissociation occurred at the interface, loss due to exciton recombination (diffusion length  $\sim 10\text{nm}$ ) was prevalent. Furthermore, since carrier mobility in the organic layers was low, dissociated charge losses due to traps was also high.<sup>9</sup> In order to enhance exciton dissociation and carrier mobilities, an interpenetrating network of electron donors and acceptors, referred to as bulk heterojunctions, was developed.

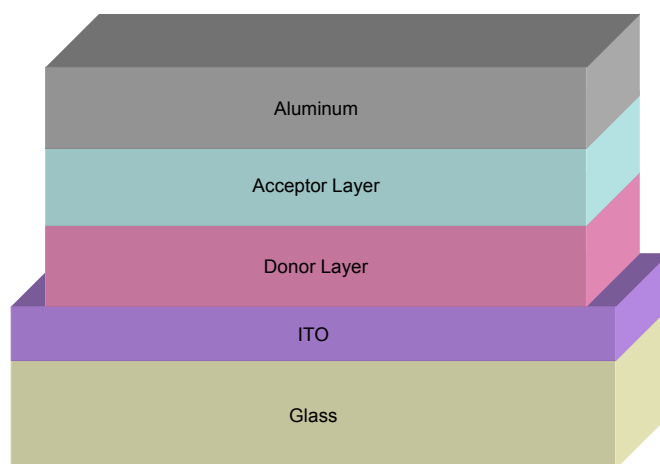


**Figure 1.2** A two-layer heterojunction device. Charge transfer occurs at the donor/acceptor interface.

The discovery of the  $C_{60}$  molecule and the continued development of conjugated polymers paved the way for the development of bulk heterojunction solar cells.<sup>10</sup> Soon after the discovery of the  $C_{60}$  molecule, it was found that it had a very high electron affinity.<sup>11, 12</sup> Furthermore, since  $C_{60}$  molecules could be partially dissolved in solvents in which the polymers were also soluble, a stable solution of the two was possible. The devices could then be deposited from solution. The uniform dispersion of  $C_{60}$  molecules in the conjugated polymers allowed the creation of uniform bulk heterojunctions throughout the polymer matrix. The initial results for the  $C_{60}$ /polymer OPVs were not impressive ( $\eta < 0.1\%$ ).<sup>13</sup> The main problem with the initial experiment was that  $C_{60}$  in fact did not dissolve totally and that the mobility of the polymer was not high. Subsequent development of a modified  $C_{60}$  molecule (referred to as phenyl- $C_{61}$ -butyric acid methyl ester [PCBM]) and a high hole mobility polymer (poly(3-hexylthiophene) [P3HT]) and improvements in processing<sup>14, 15</sup> of the materials have increased the efficiency of the state-of-the-art devices up to  $\sim 5\%$ .<sup>5</sup> Therefore, the

further understanding and characterization of the P3HT:PCBM system is the basis of this dissertation.

### **1.2.1 The Solar Spectrum**

The first step in optimizing photovoltaic devices is understanding the characteristics of the solar radiation which drives them. The intensity of solar radiation that falls on an area above the atmosphere of the earth is approximately  $1353 \text{ W/m}^2$ , referred to as the solar constant. The solar radiation is emitted from the sun's photosphere at a temperature of 6000 K, which gives it a spectral distribution closely resembling that of a black body at the corresponding temperature. Passing through the earth's atmosphere the solar radiation is attenuated by scattering from air molecules (Rayleigh), aerosols (Mie) and dust particles, as well as absorption by air molecules, in particular oxygen, ozone, water vapor, and carbon dioxide. This gives a characteristic fingerprint to the solar radiation spectrum on the earth's surface, as shown in Figure 1.3.

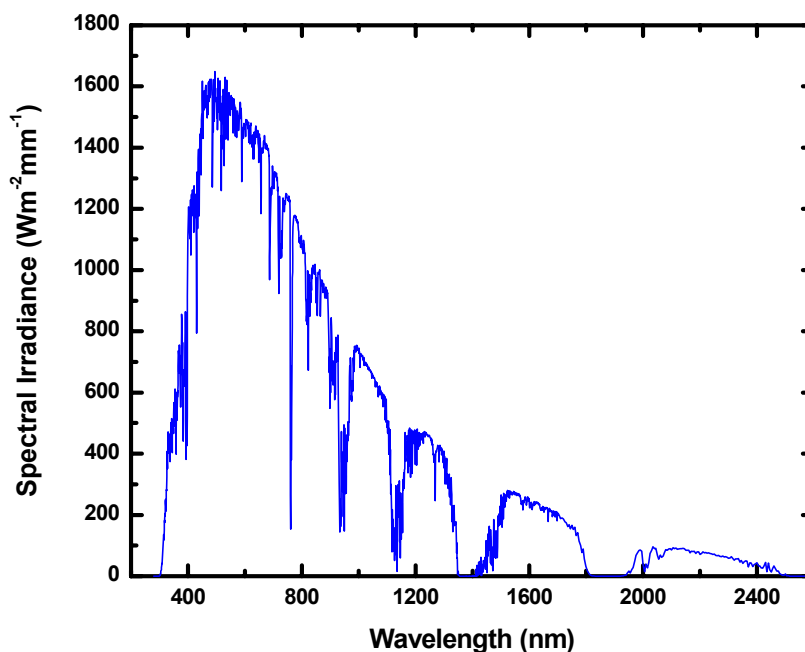


**Figure 1.3** The standard Air Mass 1.5 (AM1.5) global solar spectrum.<sup>16</sup>

AM1.5 represents an optical path which is 1.5 times the thickness of the atmosphere, which is achieved when the sun is at an angle of  $48.2^\circ$  above the horizon and results in a solar flux of  $963\text{W/m}^2$ . This angle of incidence is commonly encountered in temperate zones and thus the AM 1.5 spectrum shown in Figure 1.3 is taken as the standard condition for solar testing.

### 1.2.2 Conjugated Polymers

Conjugated polymers are organic molecules with repeating structural units attached to each other by alternating single (covalent  $\sigma$  bonds) and double (one  $\sigma$  and one  $\pi$ ) carbon-carbon bonds. The alternation of the single and double bonds, as shown



in Figure 1.4, between carbon atoms is referred to as conjugation. It is this conjugation which gives the polymers their unique electrical properties as discussed below.

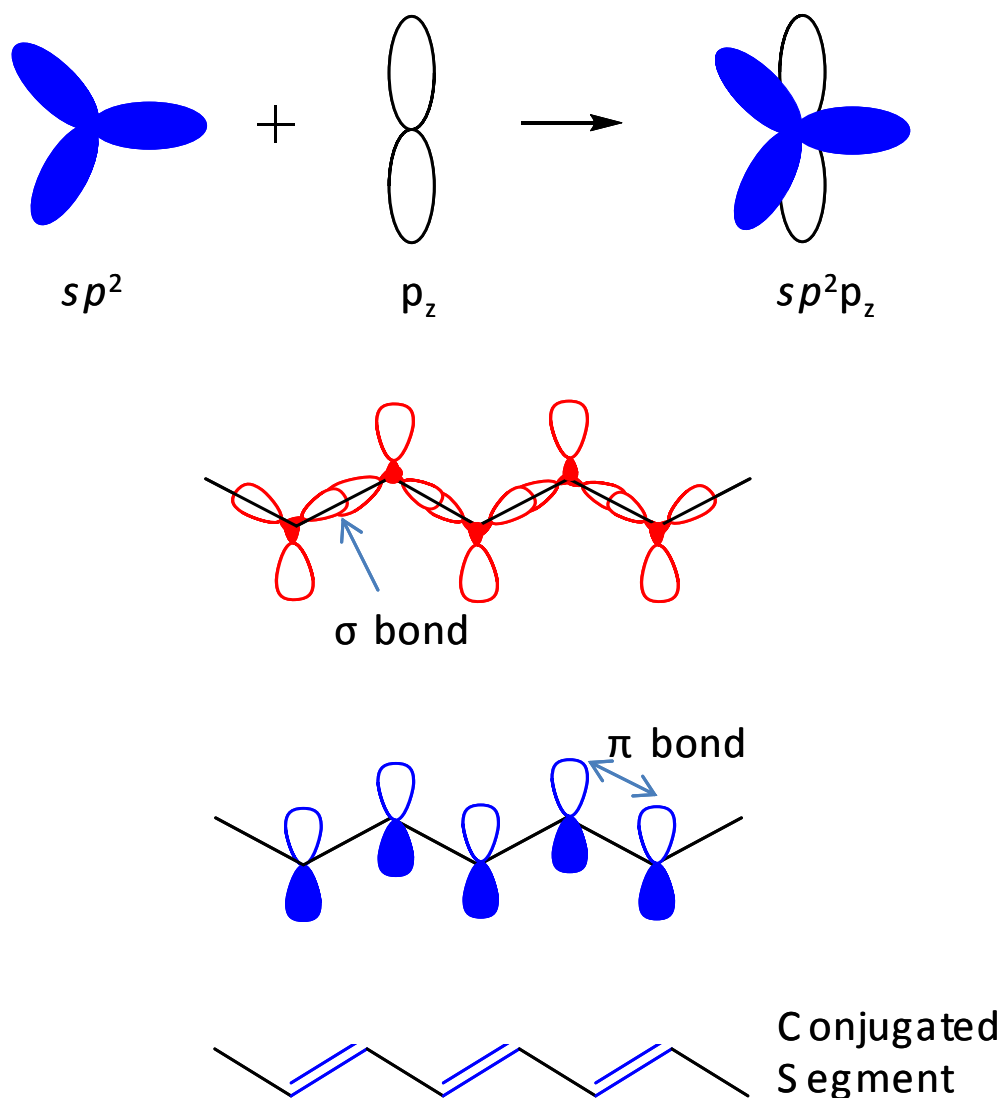


**Figure 1.4** Schematic diagram of  $\sigma$  and  $\pi$  bonds in trans-polyacetylene, showing  $p_z$  orbitals which overlap to provide the  $\pi$  bonds.<sup>17</sup>

The electronic structure of carbon is  $1s^2 2s^2 2p^2$  of which the four valence electrons are used in bonds. These electrons exhibit hybridization, with one of the 2s and two of the 2p electrons forming three  $sp^2$  hybridized orbitals. Figure 1.4 shows how the remaining fourth valence electron forms the  $p_z$  orbital, constituting the  $\pi$  bond.

The molecular  $p_z$  orbitals constituting the  $\pi$  bonds overlap and delocalize over the entire molecule.

In conjugated polymers which are semiconducting, such as P3HT which is shown in Figure 1.5, the overlap of the  $p_z$  orbital wavefunctions splits their degeneracy and produces two orbitals: a bonding  $\pi$  orbital and an antibonding  $\pi^*$  orbital. As the number of delocalized electrons on the polymer chain increase, the overlap creates energy bands similar to those found in inorganic semiconductors.

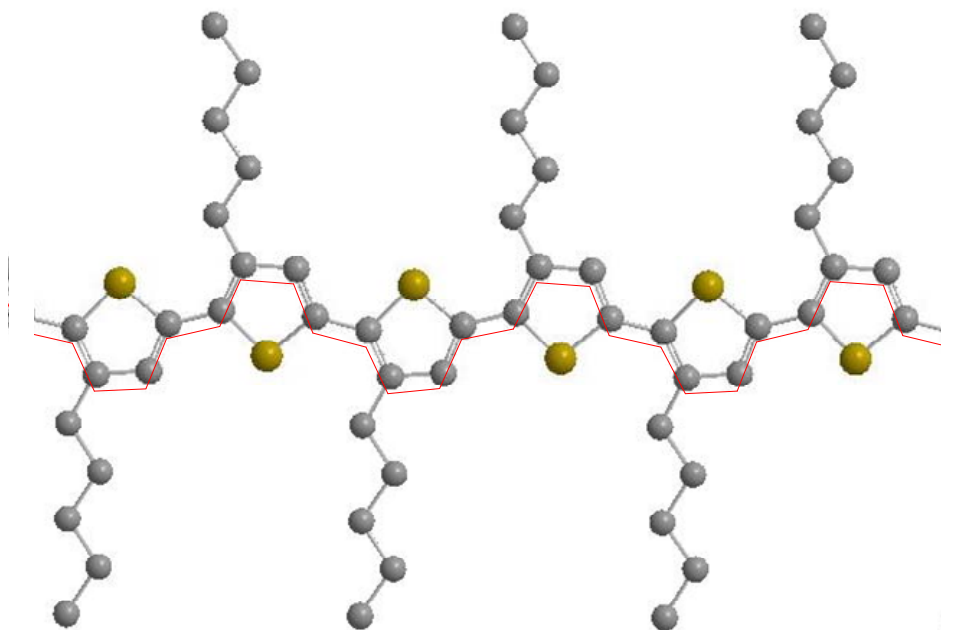


**Figure 1.5** Illustration of the semiconducting conjugated polymer P3HT. The red line shows the alternating single and double bonds of the conjugated backbone.

Analogous to the valence and conduction bands, the occupied  $\pi$  band forms the Highest Occupied Molecular Orbital (HOMO) and the unoccupied  $\pi^*$  band forms the Lowest Unoccupied Molecular Orbital (LUMO), respectively. The difference between the HOMO and LUMO is the bandgap ( $\sim 2\text{eV}$  for most semiconducting polymers), representing the minimum energy of the photons that can be absorbed. The width of the

bands and the bandgap of these polymers is a function of the number of delocalized electrons on the polymer chain and the length of the conjugated segments due to quantum confinement and the exclusion principle. Semiconducting conjugated polymers can become metallic by doping. The doping process is somewhat different than in inorganic semiconductors, as it involves oxidation of the  $\pi$  bonds, and adsorption of counter-anions on the polymer. Oxidation by oxygen and moisture is a well researched degradation mechanism in OPVs.<sup>18-21</sup> This is the reason why device encapsulation is often necessary to obtain better lifetime.

### 1.2.3 Physics of Organic Photovoltaic Devices

The conversion of photons into electricity in OPVs is fundamentally different from inorganic devices. In inorganic materials, photon absorption results in the direct generation of charge carriers, while in organic materials, the absorption of a photon results in the generation of bound electron-hole pairs (excitons).<sup>22</sup> When a photon of the appropriate energy is absorbed by the material, a ground state electron undergoes a  $\pi$ - $\pi^*$  transition, elevating the electron from the HOMO to the LUMO. However, the electron and resulting hole are bound by their Coulomb attraction and their motion is coupled. The binding energy for an exciton in poly(p-phenylene vinylene) (PPV) and polythiophene (PT) is  $\sim 0.4$  eV, for example.<sup>23</sup> Therefore, before the charge carriers can be transported and collected, the exciton must be dissociated. The dissociation of excitons can occur wherever the difference between the electron affinities of two materials will generate a sufficient local electric field. Through the study of the role of oxygen in the photoconductivity of PPV<sup>24</sup> where it acts as an electron trap, it was

realized that electron acceptor molecules could be introduced into the polymer matrix where they would act as dissociation centers.

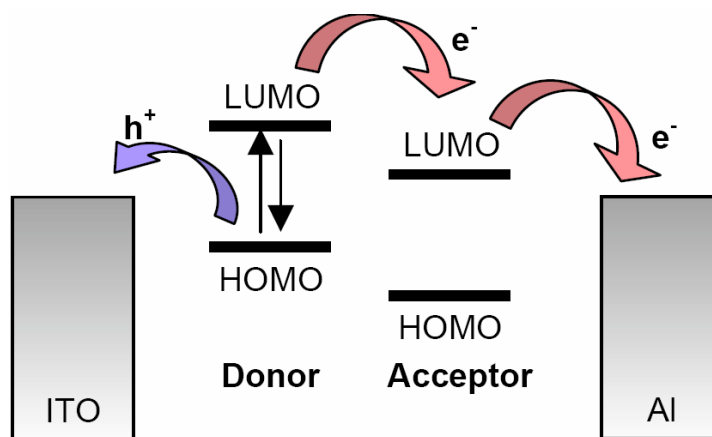


**Figure 1.6** Exciton dissociation at the donor-acceptor interface. The electron goes to the acceptor while the hole stays on the donor.<sup>25</sup>

This process causes the bound charges to separate and is referred to as photoexcited charge transfer. The interfaces are analogous to semiconductor heterojunctions. However, if the difference between the electron affinities is not adequate, or if the exciton is not sufficiently close to the junction, the exciton will recombine emitting a photon or transfer its energy to the polymer matrix. In a similar fashion to an interface created by the introduction of a different material, the interface of the polymer/electrode can serve the same function. The energy diagram of exciton dissociation at the donor/acceptor interface and transport of holes and electrons to their respective electrodes in a typical organic photovoltaic device is shown in Figure 1.6. To summarize, the process of converting light to current is accomplished in four steps: 1) Absorption of a photon leading to the formation of an exciton (bound electron-hole pair), 2) Diffusion of the exciton through the polymer matrix to the heterojunction, 3)

Charge separation through exciton dissociation, and 4) Charge transport to the anode and cathode.<sup>26</sup>

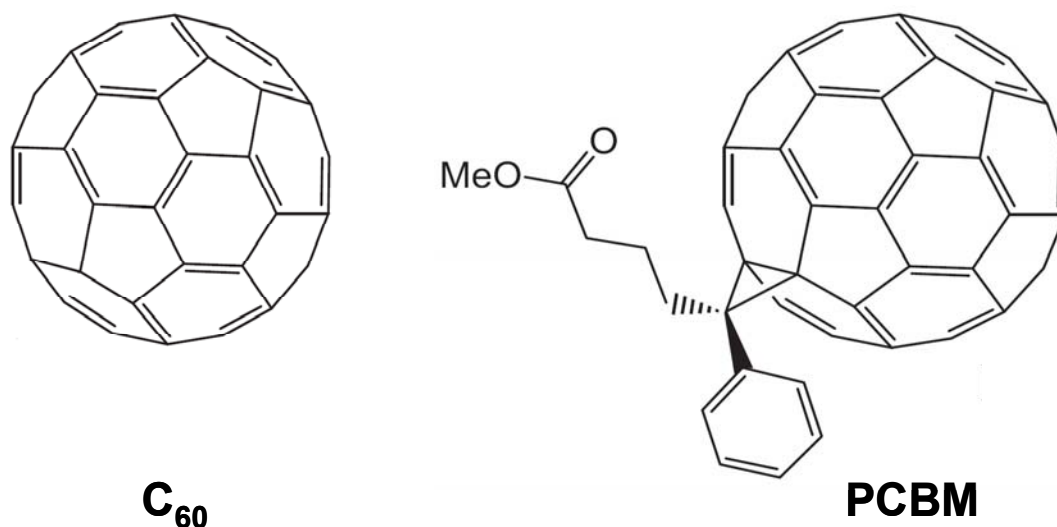


**Figure 1.7** Illustration of C<sub>60</sub> and [6,6]-phenyl C<sub>61</sub>-butyric acid methyl ester (PCBM), which are used as acceptor molecules in bulk heterojunction photovoltaic devices.

Since exciton dissociation is most effective at the heterojunction, it is clear that the exciton should be formed within its diffusion length of the interface in order to prevent recombination. The creation of sufficient heterojunctions to prevent recombination must be balanced by the maximization of the photon absorption by the active layer. Maximum absorption typically occurs at a thickness of ~100 nm of the photoactive layer, while exciton diffusion length is on the order of 10 nm.<sup>23</sup> This problem has been overcome by dispersing the nano-sized acceptor materials in a donor polymer matrix to create nano-scale bulk heterojunctions.

Figure 1.8 shows the mechanism by which excitons are dissociated and charge transfer occurs. The blending of materials in appropriate proportions creates heterojunctions within the diffusion length of the exciton. At the interface between the polymer and nanostructure, electrostatic forces result from the differences in electron

affinities. When the difference in electron affinities ( $\Delta E_a$ ) is greater than the binding energy of the exciton, generation of photoinduced charge carriers can occur.

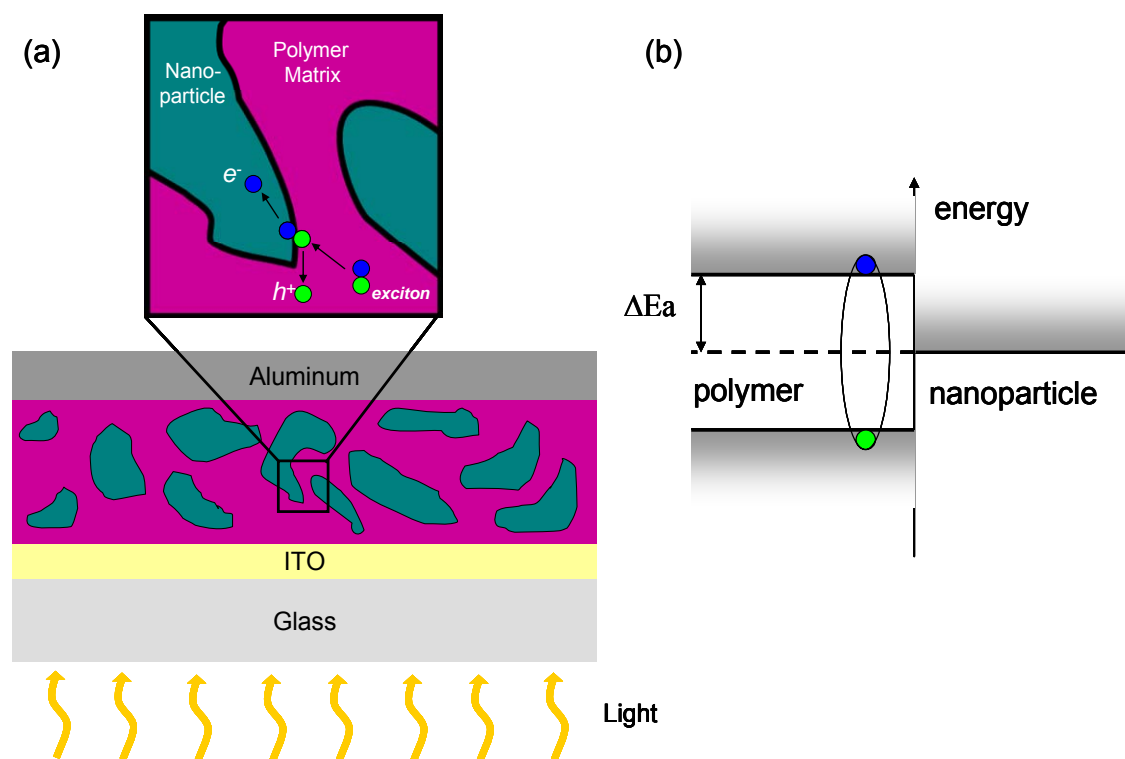


**Figure 1.8** (a) Photovoltaic device with a nanostructure/polymer active layer. The enlarged region shows the separation and subsequent transport of carriers. (b) Energy diagram of the nanocomposite indicating that the carriers can separate if the exciton binding energy is lower than the difference in electron affinity ( $\Delta E_a$ ) between the two materials.

The first report of a bulk heterojunction photovoltaic device was in 1994 when Yu et al. embedded  $C_{60}$  into an organic semiconducting polymer (MEH-PPV).<sup>27</sup> In 1995 Yu repeated this device fabrication using methano-functionalized  $C_{60}$ , (PCBM) and achieved a quantum efficiency of 29% and a power conversion efficiency of 2.9%.<sup>28</sup> The functionalizing of  $C_{60}$  with an ester to yield PCBM (see Figure 1.7) improved the solubility of the acceptor in solvents and reduced the tendency of  $C_{60}$  to crystallize in the polymer. Since then, only modest improvements in efficiency have

been achieved. The main impediment to achieving higher efficiencies appears to be the inefficient transport of charge carriers through the matrix. Specifically, hole mobilities in the polymer and electron transport through the acceptor molecule need to be improved.

The final stage of the light to electric current conversion process is the conduction of charge carriers to the anode (holes) and cathode (electrons). In the bulk heterojunction device, holes are transported via continuous pathways through the polymer matrix. The holes are transported through the matrix to a higher energy via the electric field created by the difference between the ionization potential of the polymer (the difference between the HOMO and the vacuum level) and the work function of the anode (the energy needed to expel an electron from the metal electrode). The electrons “percolate” or hop through the matrix via the dispersed acceptor molecules, transported to a lower energy level by the electric field created by the difference between the LUMO level of the acceptor molecule and work function of the cathode.

While the pathways through the polymer are continuous, they are not direct. The mobility of p-type polythiophenes have been reported as high as  $0.01\text{-}0.1\text{ cm}^2/\text{Vs}$ .<sup>29,30</sup> Although these mobilities are adequate, enhancement would improve the overall characteristics of the photovoltaic devices. Electron mobility is currently considered to be one of the factors preventing further progress in power conversion efficiency of organic photovoltaics. One of the key impediments to electron mobility is the presence of electron traps such as oxygen. Further, the percolation process is not well understood and electron transport is hindered by the presence of structural traps in the form of incomplete pathways.

P3HT and PCBM are the donor and acceptor materials, respectively, utilized in the current state-of-the-art photovoltaic devices. Figure 1.9 shows the band diagram for P3HT:PCBM bulk heterojunction devices under open-circuit conditions. Movement of charge carriers through the device follows the mechanism described above: holes are transported through the HOMO of the P3HT and electrons through the LUMO of the PCBM. It is assumed that Fermi level pinning of the aluminum contact to the PCBM creates the equivalent of an ohmic contact.<sup>31</sup> A more detailed description of how this band structure is derived will follow in this chapter and throughout the thesis.

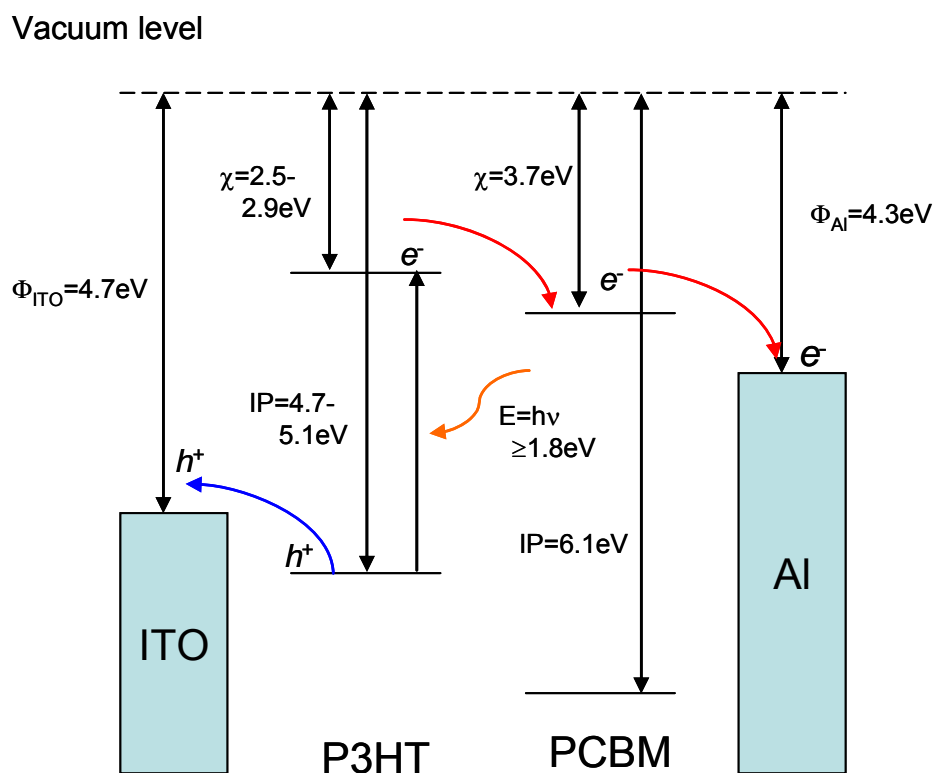


**Figure 1.9** Band structure and charge carrier movement of P3HT:PCBM device under short-circuit conditions. The open-circuit voltage ( $V_{\text{oc}}$ ) of this device is the energy difference between the HOMO level of the P3HT and the LUMO level of the PCBM.



### 1.2.4 Solar Cell Characteristics

The basic evaluation method for photovoltaic devices is measuring the current-voltage (I-V) characteristic. Figure 1.10 shows the typical shape and key elements of the I-V curve for a photovoltaic device under illumination.

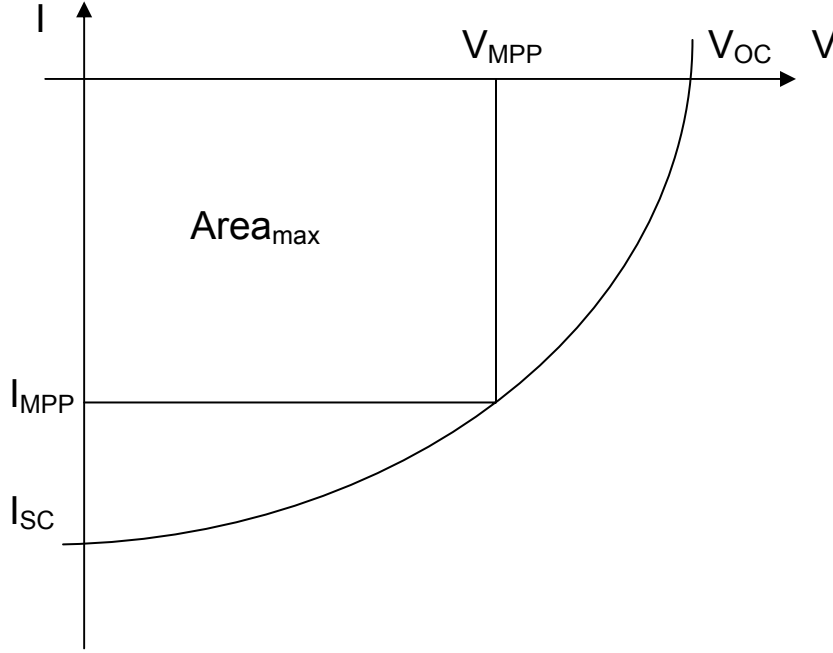


**Figure 1.10** Diagram showing current-voltage curve of photovoltaic device, including the following parameters: short circuit current ( $I_{SC}$ ), open circuit voltage ( $V_{OC}$ ), maximum power point current ( $I_{MPP}$ ), and the maximum power point voltage ( $V_{MPP}$ ).

#### 1.2.4.1 Power Conversion Efficiency

The power conversion efficiency,  $\eta$ , is the ratio of the electrical power generated by the device at its maximum power point to the input power from incident light. It is defined as:

$$\eta = \frac{P_{out}}{P_{in}} = \frac{V_{OC} \cdot I_{SC} \cdot FF}{P_{in}} \quad \text{Eq. 1.1}$$

#### 1.2.4.2 Open-Circuit Voltage

In photovoltaic devices, the open-circuit voltage ( $V_{oc}$ ) is the maximum possible voltage, in sunlight or equivalent, across the device when no current is flowing. This is also referred to as the no load condition. The open-circuit voltage is a key parameter in determining the power conversion efficiency, as shown above.

In devices based on a single layer of a conjugated polymer, the  $V_{oc}$  usually follows the metal-insulator-metal (MIM) model, and is determined by the difference between the work functions of the anode and cathode,<sup>32,33</sup> as indicated in Figure 1.11 ( $V_{OC2}$ ). However, it was demonstrated by Brabec et al.<sup>31</sup> that in bulk-heterojunction devices the  $V_{OC}$  is rather insensitive to the work function of the cathode and is directly related to the electron affinity of the electron acceptor molecule. This result supports the model where the open-circuit voltage of the bulk-heterojunction cell is directly related to the difference between the HOMO level of the donor and the LUMO level of the acceptor, as shown in Figure 1.11 ( $V_{OC1}$ ).

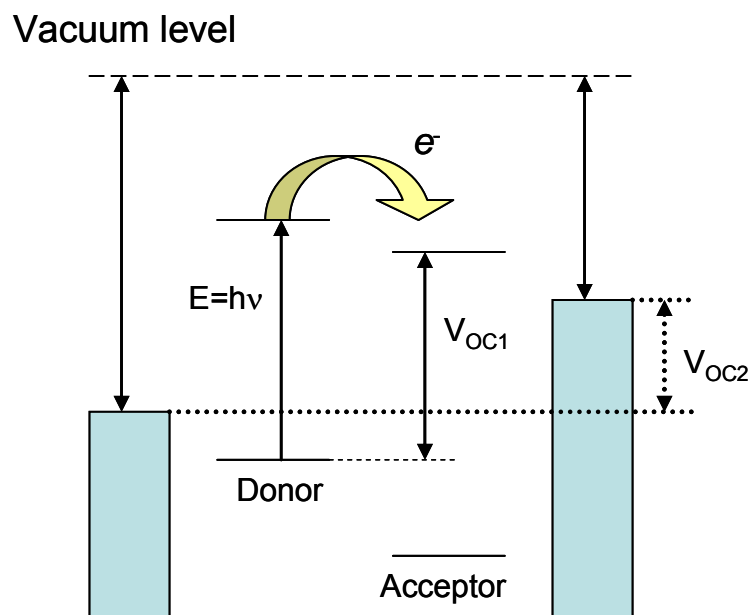


**Figure 1.11** Schematic showing variation of  $V_{OC}$ .  $V_{OC1}$  shows the difference between the HOMO level of the donor and the LUMO level of the acceptor.  $V_{OC2}$  shows the difference between the work functions of the electrodes.

This deviation from the MIM model was identified as a result of the Fermi level pinning between the cathode material and the fullerene reduction potential through charged interfacial states.<sup>31,34</sup> Additional evidence for the Brabec et al.<sup>31</sup> model is supported by the work of Kymakis et al. where they showed that the  $V_{OC}$  in P3OT and SWNT cells depended on the work function of the SWNTs in the blend and not on the work function of the electrode materials.<sup>35</sup>

### 1.2.4.3 Short-Circuit Current

The short-circuit current,  $I_{SC}$ , is the current when there is no potential across the photovoltaic device. The short-circuit current is a key parameter in determining the power conversion efficiency, as shown in Eq.1.1.

The short-circuit current in bulk-heterojunction devices depends on several parameters which closely follows the four principal steps in converting light into electrical current described in section 1.2.3. As current can be defined as the amount of charge passing through a hypothetical plane in an infinitesimally small amount of time ( $I=dq/dt$ ), it is apparent how each of these steps contributes to the short-circuit current. The absorption of light and formation of excitons provides a “baseline” for the number of potential charge carriers which may be harvested, and thus, short-circuit current will increase proportionally with the increase in irradiance and/or absorption of irradiance. Diffusion of excitons and charge separation are related and control the properties of bulk heterojunction devices through creation of charge carriers which are then transported to the electrodes, and is often measured by quantum efficiency. Thus, higher quantum efficiency will result in higher short-circuit currents. Charge transport is a drift process by which the charge carriers move to their respective electrodes in the presence of the built-in electric field resulting from the difference in the work functions of the electrodes.<sup>36</sup> The product,  $\mu\tau$ , of mobility and lifetime of the charge carriers determines the diffusion length and thus, the limit of the short-circuit current. A thin active layer will minimize recombination losses (higher  $\tau$ ), but will result in fewer photons absorbed and a lower photocurrent. Thicker layers will maximize absorption, but if such layers exceed the diffusion length of the charge carriers, a lower photocurrent will again be realized.<sup>37</sup>

#### 1.2.4.4 Fill Factor

The fill factor is defined as:

$$FF = \frac{V_{MPP} \cdot I_{MPP}}{V_{OC} \cdot I_{SC}} \quad \text{Eq. 1.2}$$

where the product of  $V_{MPP}$  and  $I_{MPP}$  is the maximum power point (MPP) of the illuminated device, as determined from the current-voltage characteristics, illustrated in Figure 1.10 in section 1.2.4.

The fill factor is the ratio of the peak power to the product  $I_{SC} \cdot V_{OC}$  and is always less than one. It is a parameter which characterizes the quality of the device and the closer the fill factor is to one, the better the quality of the device.

#### 1.2.4.5 External Quantum Efficiency

The external quantum efficiency (EQE), also referred to as the incident photon conversion efficiency (IPCE), is the ratio of charge carriers collected by a photovoltaic device to the number of incident photons, and is thus always a value between zero and one. As shown in Figure 1.12, the EQE demonstrates the photovoltaic devices ability to convert photons by wavelength. Photons with energy below the bandgap of the material would have an EQE equal to zero.

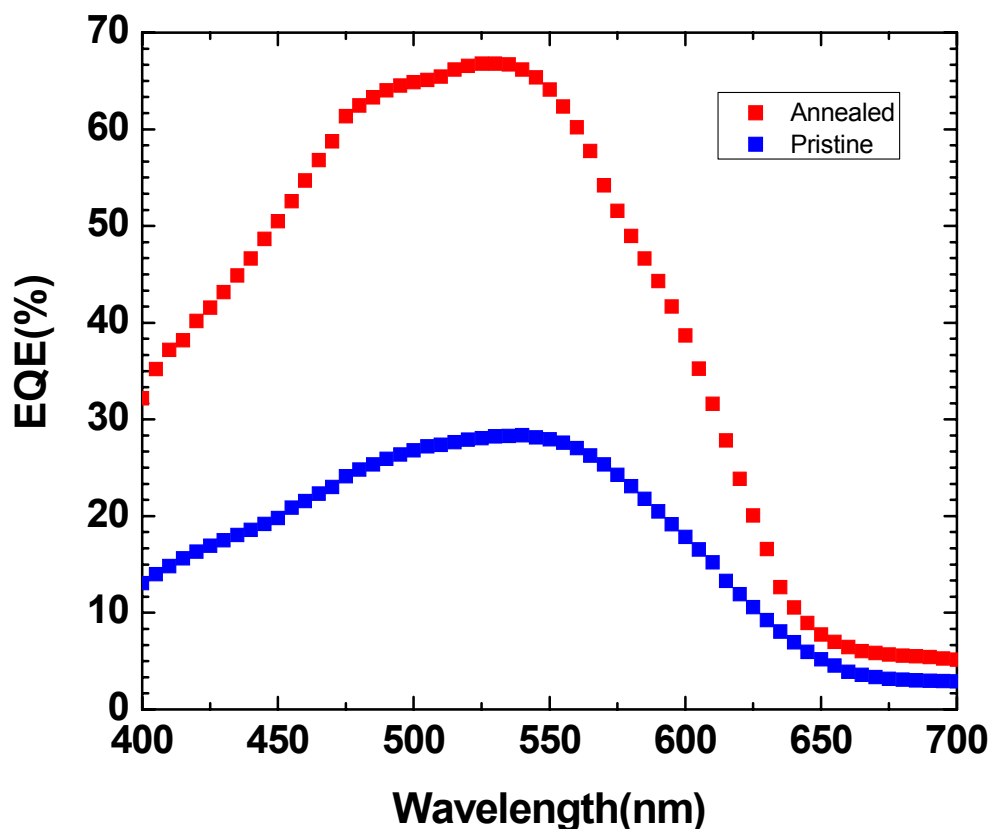


**Figure 1.12** Graph of measured EQE or IPCE for a pristine and a thermally annealed P3HT:PCBM photovoltaic device.

### 1.2.5 Band Structure

Understanding the band structure is crucial in interpreting the current-voltage characteristics of the OPV devices. Let us first consider the simplest device based on a single layer of a conjugated polymer between two electrodes with asymmetric workfunctions which follows the MIM diode model. The band structure of the MIM polymer diode under different working conditions is shown in Figure 1.13(a-d). Under the open circuit condition [Figure 1.13(a)], the photogenerated current is zero and the separated charge carriers show no preferred direction. This is also referred to as the

flatband condition. Under short-circuit [Figure 1.13(b)], the energy bands of the polymer are tilted which causes preferential transport of the holes to the ITO anode and the electrons to the Al cathode under illumination. Figure 1.13(c) shows the polymer MIM diode under reverse bias. In this case, the application of a negative voltage to the ITO increases the internal electric field, allowing better dissociation of excitons and selective transport of charge carriers to their respective electrodes. Thus, under illumination, the heterojunction is very sensitive and can also serve as a photodetector.<sup>13,38</sup> Under forward bias, Figure 1.13(d), where the applied voltage is higher than the open-circuit voltage of the device, the energy bands are tilted such that charge carriers can tunnel through the barrier. Holes are thus injected from the anode to the  $\pi$ -band and electrons are injected to the  $\pi^*$ -band and current is dominated by the recombination of holes and electrons. The device emits light if the recombination of electrons and holes is radiative.<sup>39</sup>

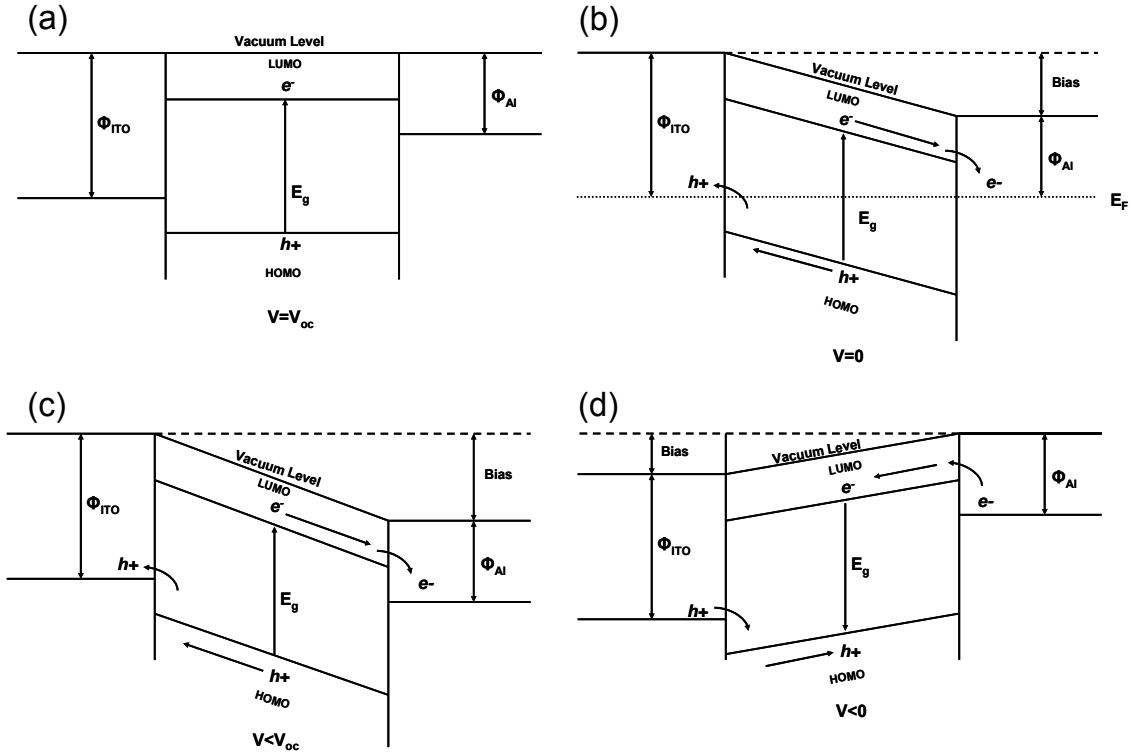


**Figure 1.13** The MIM model of the current-voltage characteristics under different working conditions. Under (a) open circuit, the  $V_{OC}$  is equal to the difference between the work functions of the electrode, (b) short-circuit, holes are transported to the anode and electrons to the cathode, (c) reverse bias the diode functions as a photodetector, and (d) forward bias the diode can function as a light emitting diode.



### 1.3 Content of this Thesis

This thesis describes our efforts towards optimizing P3HT:PCBM photovoltaics. Our aim was to not only understand the fundamental variables that govern performance, but also to provide technological insight into improving the processing of devices. Towards this end, in Chapter 2 the structure, fabrication and physics of poly(3-hexylthiophene)-[6-6]phenyl-C<sub>61</sub>-butyric acid methyl ester (P3HT:PCBM) organic photovoltaics, including aspects such as photoexcitation, charge separation, charge transport and charge collection are described. The solar spectrum and its relation to the absorption characteristics of P3HT are considered through the use of a halogen lamp and a solar simulator for the characterization of OPVs. The primary purpose of this study was to provide a simple and quick method for evaluating OPVs. We developed a technique in which indium-gallium eutectic was used as the cathode for OPVs. The use of In-Ga allowed quick testing of OPVs without the need to perform Al evaporation. Since In-Ga is semi-liquid at room temperature and has a similar work function, it could be used to rapidly evaluate the OPVs.

In Chapter 3, work which aims to understand and to improve the nanoscale morphology of P3HT:PCBM photovoltaic devices is presented. Thermal annealing of PV devices is commonly carried out to optimize device performance. As a part of this dissertation research, a new room temperature solvent vapor annealing method has been developed for improving the efficiency of OPVs. The nanoscale morphological changes that occur during the solvent vapor annealing treatment have been

characterized using *in-situ* photoluminescence and Raman spectroscopies along with *ex-situ* atomic force microscopy and UV-Vis microscopy.

A detailed background of individual and thin films of SWNTs and their use as transparent and conducting electrode in place of ITO is presented in Chapter 4. The methods for the dispersion of SWNTs and the preparation of SWNT thin films are also described. The optoelectronic properties of SWNT thin films characterized using UV-Visible spectroscopy in transmission and conductivity measurements are reported in detail. Having better understood the properties of P3HT:PCBM OPVs from works described in Chapters 1-3, in Chapter 4 we incorporated SWNT thin films as the hole conducting electrode. The use of solution processed SWNT thin films will allow development towards truly flexible OPVs. Evidence of birefringence through ellipsometry and variable angle transmission in SWNT thin films and the impact on PV devices is also presented.

The overall conclusions and recommendations for future work are provided in Chapter 5.

## 1.4 References

- <sup>1</sup> According to the Population Division of the Department of Economic and Social Affairs of the United Nations Secretariat, World Population Prospects: The 2006 Revision and World Urbanization Prospects: The 2005 Revision (<http://esa.un.org/unpp>) the estimated world population will be approximately 9.2 Billion people.
- <sup>2</sup> R. R. King, D. C. Law, K. M. Edmondson, et al., Applied Physics Letters **90**, 183516 (2007).
- <sup>3</sup> J. Y. Kim, S. H. Kim, H. H. Lee, et al., Advanced Materials **18**, 572 (2006).
- <sup>4</sup> W. Ma, C. Yang, X. Gong, et al., Advanced Functional Materials **15**, 1617 (2005).
- <sup>5</sup> M. Reyes-Reyes, K. Kim, and D. L. Carroll, Applied Physics Letters **87** (2005).
- <sup>6</sup> M. C. Scharber, D. Mühlbacher, M. Koppe, et al., Advanced Materials **18**, 789 (2006).
- <sup>7</sup> C. K. Chiang, C. R. Fincher, Y. W. Park, et al., Physical Review Letters **39**, 1098–1101 (1977).
- <sup>8</sup> C. W. Tang, Applied Physics Letters **48**, 183 (1986).
- <sup>9</sup> J. J. M. Halls, C. A. Walsh, N. C. Greenham, et al., Nature **376**, 498–500 (1995).
- <sup>10</sup> M. F. Durstock, R. J. Spry, J. W. Baur, et al., Journal of Applied Physics **94**, 3253 (2003).
- <sup>11</sup> R. F. Curl and R. E. Smalley, Science %R 10.1126/science.242.4881.1017 **242**, 1017 (1988).
- <sup>12</sup> R. E. Haufler, J. Conceicao, L. P. F. Chibante, et al., J. Phys. Chem. **94**, 8634 (1990).
- <sup>13</sup> N. S. Sariciftci, D. Braun, C. Zhang, et al., Applied Physics Letters **62**, 585 (1993).
- <sup>14</sup> Y. Kim, S. A. Choulis, J. Nelson, et al., Journal Of Materials Science **40**, 1371 (2005).
- <sup>15</sup> X. N. Yang, J. Loos, S. C. Veenstra, et al., Nano Letters **5**, 579 (2005).
- <sup>16</sup> Derived from the ASTM G173-03 Tables obtained from the Renewable Resource Data Center website at <http://rredc.nrel.gov/solar/spectra/am1.5/>.
- <sup>17</sup> E. Kymakis, Ph.D. thesis, Engineering, University of Cambridge, 2003

- 18 J. C. Hummelen, J. Knol, and L. Sanchez, *Proceedings of SPIE* **4108**, 76 (2001).
- 19 K. Kawano, R. Pacios, D. Poplavskyy, et al., *Solar Energy Materials & Solar Cells* **90**, 3520 (2006).
- 20 F. C. Krebs, J. E. Carle, N. Cruys-Bagger, et al., *Solar Energy Materials & Solar Cells* **86**, 499 (2004).
- 21 H. Neugebauer, C. Brabec, J. C. Hummelen, et al., *Solar Energy Materials & Solar Cells* **61**, 35 (2000).
- 22 M. Chandross, S. Mazumdar, S. Jeglinski, et al., *Physical Review B* **50** (1994).
- 23 E. M. Conwell and H. A. Mizes, *Physical Review B* **51**, 6953 (1995).
- 24 E. Frankevich, A. Zakhidov, K. Yoshino, et al., *Physical Review B* **53**, 4498 (1996).
- 25 H. Spanggaard and F. C. Krebs, *Solar Energy Materials & Solar Cells* **83**, 125 (2004).
- 26 H. Hoppe and N. S. Sariciftci, *Journal of Material Research* **19**, 1924 (2004).
- 27 G. Yu, K. Pakbaz, and A. J. Heeger, *Applied Physics Letters* **64**, 3422 (1994).
- 28 G. Yu, J. Gao, J. C. Hummelen, et al., *Science* **270**, 1789 (1995).
- 29 J.-F. Chang, B. Sun, D. W. Breiby, et al., *Chemistry of Materials* **16**, 4772 (2004).
- 30 B. S. Ong, Y. L. Wu, P. Liu, et al., *Journal of the American Chemical Society* **126**, 3378 (2004).
- 31 C. J. Brabec, A. Cravino, D. Meissner, et al., *Advanced Functional Materials* **11**, 374 (2001).
- 32 I. D. Parker, *Journal of Applied Physics* **75**, 1656 (1994).
- 33 J. Liu, Y. Shi, and Y. Yang, *Advanced Functional Materials* **11**, 420 (2001).
- 34 V. D. Mihailechi, P. W. M. Blom, J. C. Hummelen, et al., *Journal of Applied Physics* **94**, 6849 (2003).
- 35 E. Kymakis and G. A. J. Amaratunga, *Applied Physics Letters* **80**, 112 (2002).
- 36 I. H. Campbell, T. W. Hagler, D. L. Smith, et al., *Physical Review Letters* **76**, 1900 (1996).

- <sup>37</sup> T. Wellinger, P. D. r. n. U. Lemmer, and D.-P. A. Colsmann, (Light Technology Institute, Department of Electrical Engineering and Information Technology, Universität Karlsruhe (TH), 2005), p. 58.
- <sup>38</sup> L. S. Roman, M. R. Andersson, T. Yohannes, et al., *Advanced Materials* **9**, 1164 (1997).
- <sup>39</sup> M. Pope, H. P. Kallmann, and P. Magnate, *Journal of Chemical Physics*, 2042 (1963).

## Chapter 2

### Development of an Inexpensive Method to Rapidly Test Organic Photovoltaic Devices

#### 2.1 Introduction

Having introduced the basics of organic photovoltaics (OPVs) in Chapter 1, the structure, fabrication and influence of processing parameters on poly(3-hexylthiophene:phenyl-C<sub>61</sub>-butyric acid methyl ester (P3HT:PCBM) devices will be presented in more detail here. At the beginning of this project, basic equipment such as a AM 1.5 solar simulator for evaluation of OPVs, thermal evaporator for making aluminum (Al) contacts, and glove box for the preparation of materials was not available. Therefore, in order to initiate work on OPVs while the aforementioned equipment was being commissioned, an alternative method that allowed quick evaluation of devices was developed with Professor Aurelien Du Pasquier. This fast, simple and inexpensive method for testing the photovoltaic characteristics of organic devices utilized Ga-In eutectic and a halogen light source instead of evaporated aluminum and a solar simulator, respectively. It allowed testing of large numbers of devices rapidly. Although this method does not yield the maximum efficiency values due to non-optimized device structure, it does allow for the comparison of the influence of various OPV parameters. Using this method, the fabrication parameters such as P3HT:PCBM ratio for organic solar cells spin-coated from chloroform and chlorobenzene solutions were investigated and optimized. A method to correct the spectral mismatch of the halogen light source with the solar spectrum was also proposed in order to correlate our results with those from the literature which used AM 1.5

simulators. The results obtained from this study were essential to our understanding of the influence of various processing and device parameters. The knowledge obtained from this work of optimized parameters was utilized in subsequent experiments using a glove box, AM 1.5 solar simulator and evaporated Al contacts to obtain devices with efficiencies of up to 3%.

In this chapter, we will describe each component of the OPV device and provide a brief motivation for the use of P3HT and PCBM as the photoactive components. Subsequent to this, we will describe how a halogen lamp can be used in place of an AM 1.5 simulator and provide a mechanism to overcome the mismatch with the solar spectrum. Afterwards, the use of Ga-In eutectic as the top electrode is described. The results from OPVs with variable P3HT:PCBM ratios measured using our inexpensive and quick testing method are also reported in this chapter. Finally, the results from OPVs fabricated with Ga-In electrodes and tested under a halogen lamp are correlated with devices fabricated from evaporated Al electrodes and measured under AM 1.5 radiation in order to determine the feasibility of the alternative method. Our results indicate that the method described is a cost effective way to measure a large number of OPVs quickly and relatively accurately.

## 2.2 Structure and Materials of P3HT:PCBM Organic Photovoltaics

The P3HT:PCBM devices studied in this thesis utilized a sandwich structure where the active layer (P3HT:PCBM) lies between two electrodes with asymmetric workfunctions. Figure 2.1 shows the structure of a typical OPV device studied here and widely by others.<sup>1</sup> Each layer of this device consists of indium tin oxide (ITO) on glass, Poly(3,4-ethylenedioxythiophene):poly(styrenesulfonate) [PEDOT:PSS], P3HT:PCBM layer and Al top contact. The ITO layer serves as the transparent and conducting anode for hole collection. ITO coated float glass was purchased from Delta Technologies, Ltd. The ITO film was between 60 and 100nm thick with a sheet resistance of 15-25  $\Omega/\square$  at a nominal transmittance of greater than 78%. To prepare the OPV devices, ITO glass was cleaved into 25mm x 25mm chips, cleaned in sonicated baths of acetone and methanol, and then blown dry with nitrogen gas.

Prior to the deposition of the P3HT:PCBM layer on ITO, PEDOT:PSS is deposited by spin coating. PEDOT:PSS is an intrinsically conducting polymer which is commercially available in an aqueous solution. The PEDOT:PSS layer is used widely in OPVs between the ITO and P3HT:PCBM layer to create a smoother interface. In addition to improving the interface, PEDOT:PSS has favorable hole transport properties with a workfunction of 5.0 to 5.2eV,<sup>2,3</sup> which lies below that of ITO ( $\sim 4.7\text{eV}$ ), favoring hole collection. For the purposes of this study, PEDOT:PSS was diluted with methanol or isopropanol (in 1:1 and 1:2 ratios) and spin coated at 1000-3000 rpm to give a  $\sim 50\text{nm}$  thick layer.

As described in Chapter 1, the current state-of-the-art OPVs rely on a bi-continuous network of donor and acceptor materials (bulk heterojunctions) which



provide interfaces with sufficient differences in electron affinity to promote the separation of charge carriers from excitons formed by the donor layer. In our devices, we have chosen the widely utilized P3HT and PCBM as the donor and acceptor materials, respectively, for several reasons. First, their properties allow for sufficient interfacial area so that there is a high probability of exciton diffusion to an interface, allowing charge separation and preferential charge transport through the matrix. Second, P3HT has a relatively low band gap with published values from 1.9-2.1eV<sup>4-6</sup> which fits relatively well with the solar spectrum compared to other conjugated polymers. P3HT is also soluble in many solvents including chloroform, chlorobenzene and toluene. Furthermore, it has HOMO and LUMO values of ~4.7-5.1eV and ~2.5-2.9eV,<sup>6</sup> respectively, which allows for favorable band alignment with the acceptor materials PCBM with HOMO and LUMO values of 5.5eV and 3.8eV, respectively<sup>6</sup> (see Figure 1.8 in Chapter 1). Finally, P3HT has the highest hole mobility amongst solution processed conjugated polymers. PCBM is also highly soluble in the same solvents as P3HT, allowing for the preparation of homogeneous blend solutions which can be spin coated or drop cast onto the devices. The HOMO and LUMO bands of PCBM are complimentary to those of P3HT for transport of electrons to the top electrode. The P3HT:PCBM blend layers are typically 100-200nm thick.

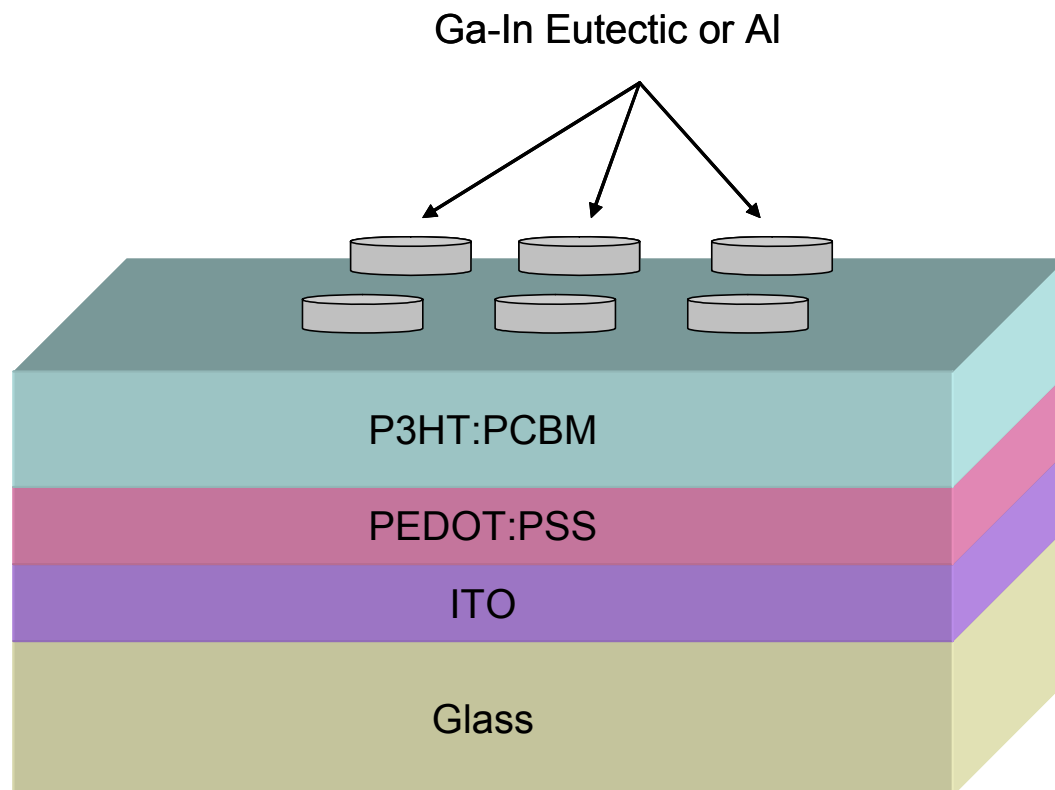


**Figure 2.1** Schematic of P3HT:PCBM organic photovoltaic device.

Since the P3HT:PCBM layer in OPVs is thin, and because P3HT has lower charge mobility than its inorganic counterparts, the cathode must cover a large area of the active surface of the device and provide uniform contact to the organic layer. Thus, thermal evaporation is the preferred method for depositing Al electrodes. Aluminum is most commonly used in OPVs because its work function of  $\sim 4.3\text{eV}$  creates the internal electric field necessary for preferential charge transport of holes to the anode and electrons to the cathode along with the necessary band alignment to extract electrons from PCBM (see Figure 1.12 in Chapter 1). However, other metals or conductors with a similar work function can also serve as the electron collecting cathode.

## **2.3 Fabrication and Testing of Devices**

### **2.3.1 Ga-In Electrodes**

Organic thin films for photovoltaics can be deposited easily and inexpensively from solutions by simple methods such as spin coating or drop casting. However, in order to characterize OPV devices, two items are required: a vacuum evaporator and a solar simulator, expensive pieces of equipment that require an investment on the order of several tens of thousands of dollars. Therefore, although the use of Ga-In eutectic as the top electrode is not commercially practical, it has advantages for laboratory scale testing of solar cells. Pure gallium melts at 30°C, and has a work function of 4.2 eV, very close to that of aluminum (4.3 eV), making it suitable as the cathode in OPVs. Even more convenient is Ga-In eutectic, which melts at 15.7°C and is thus a liquid at room temperature. To facilitate the use of a liquid metal as an electrode, a rubber o-ring of 3mm diameter was used to contain a Ga-In droplet and control the contact area on top of the P3HT:PCBM layer, resulting in a photoactive area of 0.07 cm<sup>2</sup>. Ga-In eutectic is a cheaper solution because electrodes can be placed on the device in air without any vacuum equipment. One limitation of Ga-In eutectic is that a lithium fluoride layer cannot be used below the electrodes. Approximately 1nm of lithium fluoride is generally used to create an ohmic and hole blocking contact between the P3HT:PCBM layer and the Al electrodes.

### **2.3.2 Halogen Lamp for Simulated Solar Spectrum**

Solar simulation requires a costly xenon arc lamp, with a high-voltage igniter, stable power supply, and AM 1.5 filter. Radiation emitted from a xenon arc is the

closest to natural sunlight with a color temperature of around 5800 K. Halogen light sources have some advantages over xenon light sources: they are inexpensive and readily available, their intensity output can be fully controlled with a variable power supply, and their small form factor makes them easy to use in a controlled atmosphere such as a glove-box. However, their color temperature of 3000K is severely mismatched with the solar spectrum, resulting in overestimated conversion efficiencies. We have used a halogen lamp indoors to obtain I–V curves of OPV diodes to extract the fill factor. Then, a portable multi-meter was used outdoors under natural sunlight to obtain the short-circuit current and open-circuit voltage of the device. The intensity of the natural sunlight was obtained from a calibrated solar cell. Then, the fill factor measured indoors at similar current was used to calculate a very good approximation of the cell conversion efficiency:

$$\eta = (FF_{\text{indoors}} * I_{\text{sc}_{\text{outdoors}}} * V_{\text{oc}_{\text{outdoors}}}) / \text{Light intensity}_{\text{outdoors}}.$$

Finally, the output of the halogen light source can be recalibrated in sunlight equivalents to perform all measurements indoors.

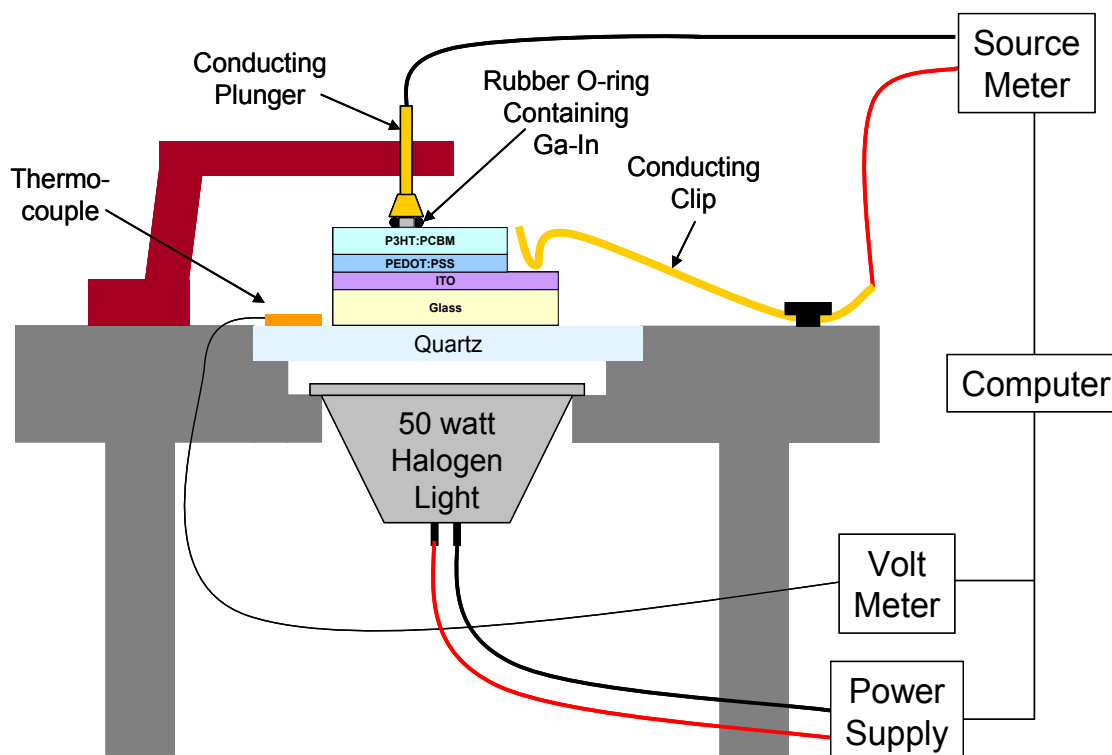


**Figure 2.2** Schematic of apparatus constructed for testing P3HT:PCBM photovoltaic devices using Ga-In eutectic as the top electrode and a halogen lamp as the solar simulator. The heat from the light source allows for testing and *in-situ* thermal annealing.

The I–V measurements were performed in air at 25°C, between -0.2 and +1V at 100mV/s, with an EG&G 273A potentiostat–galvanostat, using an especially programmed Labview™ software. The light source consisted of a 50W MR16 halogen light bulb computer controlled by an HP6038A power supply. The light source intensity was calibrated in W/m<sup>2</sup> as a function of the power input with a reference Si solar cell (Daystar solar meter). A special apparatus, shown schematically in Figure 2.2, was designed and fabricated in Professor Aurelien Du Pasquier’s laboratory to incorporate the halogen lamp source and the Ga-In eutectic top electrode. As will be discussed later in this and future chapters, thermal annealing of OPV devices is crucial in improving

their efficiency. The set up in Figure 2.2 allows the use of the halogen lamp to uniformly heat the samples up to 135°C.

## **2.4 Results and Discussion**

### **2.4.1 Light Intensity and Spectral Mismatch Correction**

When an illumination source not matching the solar spectrum is used in the measurement of solar cells, two errors are introduced. First, the integrated light intensity over the entire spectrum (power density in  $\text{W/m}^2$ ) may be incorrect if the sensor used has a responsivity curve that is not matched for the source used. Secondly, because the device being measured also has an associated responsivity curve, the spectral mismatch with the solar spectrum, shown in Figure 2.3, may cause the measured efficiency to differ from that of sunlight, even if the integrated light intensity is the same. It is clear from the curves in Figure 2.3 that current generated by a P3HT:PCBM solar cell should be different when measured with a halogen light source at an equivalent illumination intensity from a AM 1.5 solar simulator. Thus, we have developed a method to recalibrate our light source and correct both errors at the same time.

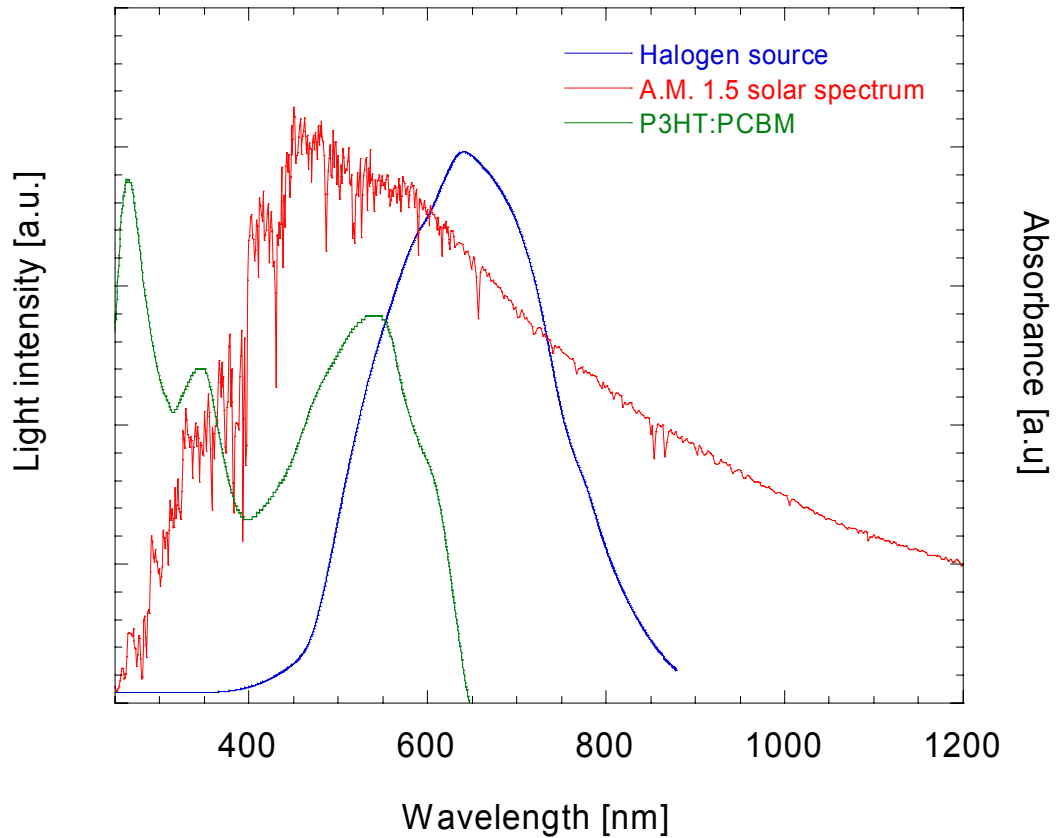


**Figure 2.3** Absorption spectrum of P3HT:PCBM (ratio=1:1) layer spin-coated on glass, spectral output of the halogen light source used to test them, and AM 1.5 solar spectrum.

The power output of the halogen light source was obtained with a power meter utilizing a calibrated Si solar cell. Since the output of the meter correlates the responsivity of the solar cell to the solar spectrum, the value of the illumination from the halogen light source in  $\text{W/m}^2$  is erroneous. However, it does correctly measure the changes in the illumination intensity (by varying the power supplied to the halogen light source), since they are proportional to the short-circuit current. Several I–V curves were measured for a P3HT:PCBM device at various levels of illumination from the halogen light source. From these I–V curves, the fill factor versus short-circuit current

relationship shown in Figure 2.4 was derived. The same P3HT:PCBM solar cell was then measured outdoors, and the short-circuit current and open-circuit voltage were obtained with a portable multi-meter. Simultaneously the sunlight illumination of  $99\text{mW}/\text{cm}^2$  was also measured with the calibrated Si solar cell. Therefore, if the fill factor is not sensitive to the spectral composition of the light source, then it can be estimated for the P3HT:PCBM device using the data in Figure 2.4, as indicated by the vertical line. The position of the vertical line in Figure 2.4 is determined by the short-circuit current measured outdoors. The validity of the assumption regarding the relationship between fill factor values and spectral composition has been verified with an AM 1.5 solar simulator and discussed later.

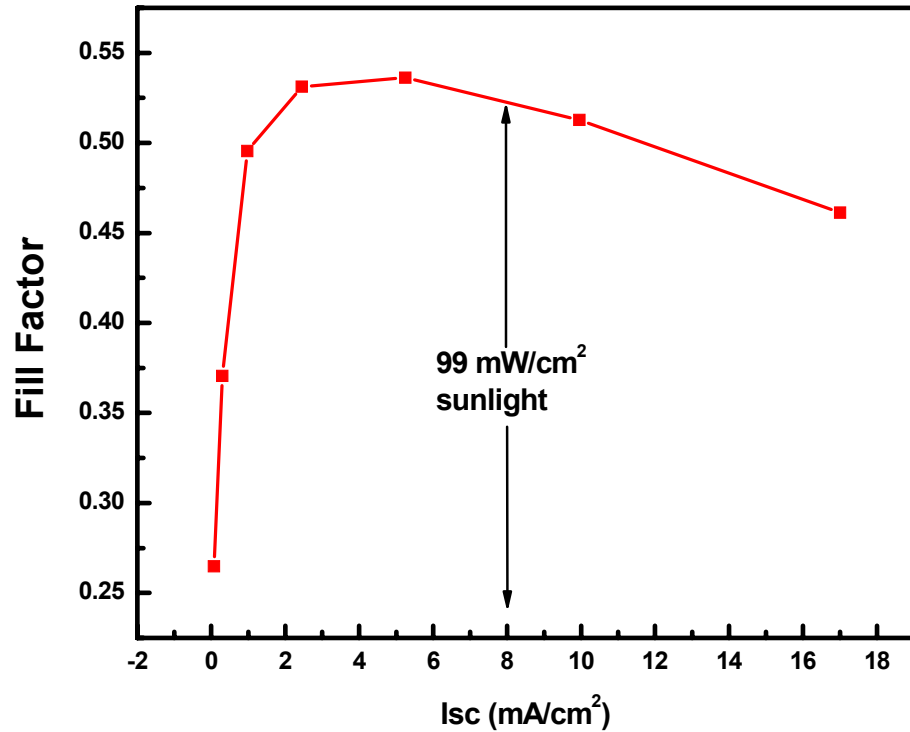


**Figure 2.4** Fill factor versus short-circuit current of a P3HT:PCBM 1:1 photovoltaic device measured with a halogen light source. The arrows indicate the value of the short-circuit current measured in sunlight and the corresponding estimated fill factor.



Thus, the sunlight efficiency of the cell can then be calculated by:

$$\eta = FF_{\text{indoors}} * I_{\text{sc}_{\text{outdoors}}} * V_{\text{oc}_{\text{outdoors}}} / \text{Light intensity}_{\text{outdoors}}$$

However, the short-circuit current versus light intensity of the halogen lamp is uncorrected with respect to the solar radiation. In order to correct this, the  $\text{Log}(I_{\text{sc}})$  versus  $\text{Log}(I_{\text{hal}})$  data were plotted, as shown in Figure 2.5. The corrected values were obtained by translating the experimental data horizontally while maintaining the same slope to intercept the experimental point obtained in sunlight (indicated by the gray square in the plot). This assumes that the variation of short-circuit current with light intensity is independent of wavelength. Finally, the output of the halogen light source as function of its input power was recalibrated with the new  $\text{Log}(I_{\text{sc}})$  versus  $\text{Log}(I_{\text{sun}})$  curve, resulting in higher power for the halogen light source. After this correction was performed, the short-circuit currents were obtained at  $100 \text{ mW/cm}^2$  simulated by the halogen light source and  $100 \text{ mW/cm}^2$  of sunlight.

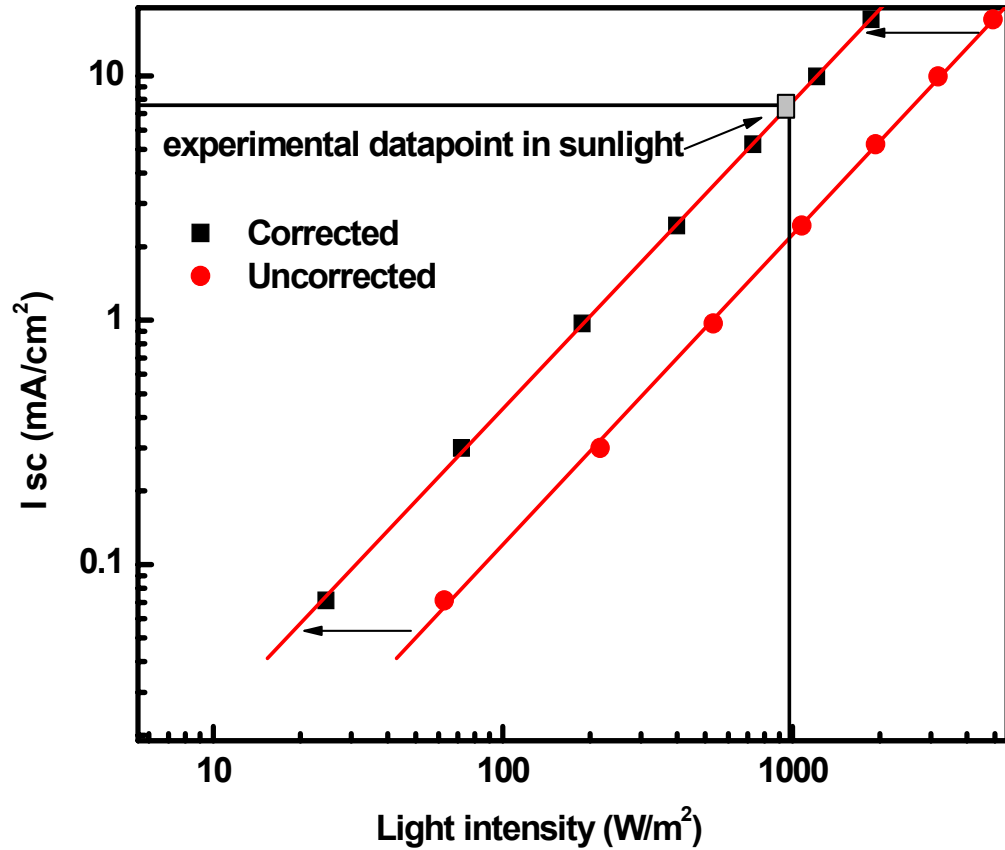


**Figure 2.5** Log-Log plot of light intensity versus short-circuit current for P3HT:PCBM 1:1 solar cell measured with halogen light source. Uncorrected values of light intensity (dots) and corrected values (squares) intercepting data point in sunlight.

While the above methodology relies upon several assumptions regarding the relationship between illumination intensity, spectral composition of the light sources and solar cell performance characteristics, it utilizes a simple 35 watt halogen bulb and variable power supply as opposed to an expensive AM 1.5 solar simulator (>\$20,000). Despite the short comings of the method, the light source and analysis methodology was found to be useful for comparison of materials and processing conditions used in the development of organic photovoltaic devices, especially in the initial stages of the project.

### 2.4.2 *In situ* Thermal Annealing and Efficiency Change Monitoring

The dramatic and irreversible improvement in power conversion efficiency of P3HT:PCBM OPVs after thermal annealing has been reported in many studies.<sup>7-10</sup> This enhancement has generally been attributed to improved nanostructured ordering in the P3HT:PCBM material leading to better charge carrier generation and hole mobility through increased P3HT crystallinity.<sup>10-16</sup> Alternatives to thermal annealing and the morphology of P3HT:PCBM OPVs will be examined in detail in Chapter 3.

There are numerous published combinations of temperature and time used to anneal P3HT:PCBM OPVs, with optimal temperatures ranging from 50°C<sup>7</sup> to 140°C<sup>9</sup>, and optimal times from 1 minute to 15 minutes. Furthermore, some researchers perform annealing in air, others in inert atmosphere, and some combine annealing with electrical polarization.<sup>16</sup> In order to get a better insight into the optimum conditions necessary to improve the properties of OPVs fabricated at Rutgers, we embarked on a detailed study to investigate a wide range of parameters. We found that the optimal annealing conditions were dependent on variables such as layer thickness, film composition, solvent used and film deposition method. The dependence of annealing treatment on P3HT:PCBM ratio and type of solvent used was investigated in order to determine the most suitable conditions for our devices. Specifically, we used chloroform and chlorobenzene as the solvents at two different P3HT:PCBM ratios (1:1 and 1:2). In addition, we also deposited the layers at three different spin speeds. The results from this study are summarized in Table 2.1 which lists the efficiency values of the various types of films investigated before and after thermal annealing using a halogen lamp. A thermocouple attached to the testing apparatus was used to monitor

the temperature as indicated in Figure 2.2. It can be seen from Table 2.1 that films deposited from chlorobenzene or with low PCBM concentrations require lower annealing temperatures to maximize their efficiency than those obtained from chloroform and high PCBM concentrations.

**Table 2.1** Efficiencies before and after annealing and optimal annealing temperatures as a function of type of solvent, P3HT:PCBM composition and spin coating speed.

Solvent	Spin speed	1000 rpm	1500 rpm
	Composition	a/b (c)	a/b (c)
Chlorobenzene	1:1 (20 g/L)	0.05/0.33 (80)	0.12/0.55 (70)
Chlorobenzene	2:1 (20 g/L)	0.33/0.67 (60)	0.21/0.8 (55)
Chloroform	1:1 (10 g/L)	0.22/1.52 (75)	0.23/0.86 (75)
Chloroform	2:1 (10 g/L)	0.17/0.83 (60)	0.14/0.59 (70)

- a. Efficiency before annealing (%)
- b. Efficiency after annealing (%)
- c. Best annealing temperature (°C)

A halogen lamp at  $\sim 2400 \text{ W/m}^2$  was used as the heat source and the efficiency evolution was monitored through repeated I-V cycles, as shown in Figure 2.6. In Figure 2.6a, the diode characteristics of a typical device as a function of illumination time with the halogen lamp are shown. In Figure 2.6b, the efficiency of the device as a function of time is plotted. The maximum annealing temperature was controlled by the illumination time. The monitoring of the efficiency in real time (as shown in Figure 2.6b) allows the determination of the optimal annealing temperature. The measurements were stopped when the efficiency reached a plateau, as seen in Figure 2.6b. To investigate the temperature dependence, the measurements were conducted at longer illumination times (higher temperature). It should be mentioned that the change in efficiency with annealing time is irreversible and the devices retain the maximum

efficiency when cooled to room temperature and retested. Returning to Figure 2.6a, it can be seen that the short-circuit current increases with annealing time which leads to an enhancement in efficiency. The mechanism responsible for the changes in  $I_{sc}$  with annealing will be discussed further in Chapter 3.

In addition to the increase in  $I_{sc}$ , the open-circuit voltage of the device is found to decrease with annealing time. The variation of the  $V_{oc}$  with annealing varies from study to study. Some researchers<sup>15, 17</sup> found it to increase with annealing, while others<sup>10</sup> found it to decrease as we do. Several arguments can be made to explain the decrease in open-circuit voltage. First, it can be seen in Figure 2.6(a) that above the  $V_{oc}$ , the dark current for the device after thermal annealing is significantly larger than as-fabricated. Since the total current at  $V_{oc}$  is zero, an increase in dark current should lead to a decrease in  $V_{oc}$ , assuming that the photo-current remains unchanged in this regime. Second, studies have shown that loading and aggregation of PCBM can lead to changes in  $V_{oc}$  values.<sup>18</sup> We believe the decrease in  $V_{oc}$ , as shown in Figure 2.6(a), may be the result of the aggregation of the PCBM in the nanophase. This view is consistent with that held by Reyes-Reyes et al. who have shown similar results.<sup>10</sup> The aggregation of PCBM and ordering of the P3HT can be observed by AFM.<sup>10, 19</sup> After annealing, the formation of clusters are most likely the result of PCBM aggregation. In our work related to solvent vapor annealing which will be described in the next chapter, we show AFM images which suggest the development of fibril-like structures and decreased contrast. This is also consistent with the work by Reyes-Reyes et al.<sup>10</sup> where it is suggested that aggregated PCBM may lie under a thin layer of P3HT. This supports the

view held by others that aggregate morphology is a likely explanation for variations in  $V_{oc}$ .

The optimal annealing temperature we found in this study with our inexpensive set up was  $\sim 80^{\circ}\text{C}$ . This is substantially lower than what is generally reported in the literature and what was found in future studies (see Chapter 3). Annealing temperatures ranging from  $120^{\circ}\text{C}$  to  $150^{\circ}\text{C}$ <sup>9, 10, 20, 21</sup> are usually found to yield the best results. The temperature measured in this study is likely to be underestimated because we use a thermocouple to measure the temperature away from the actual device, as indicated in Figure 2.2. Usually annealing is performed in an oven where the entire device is uniformly heated to the desired temperature. Nevertheless, the set-up allows us to compare devices and process parameters.

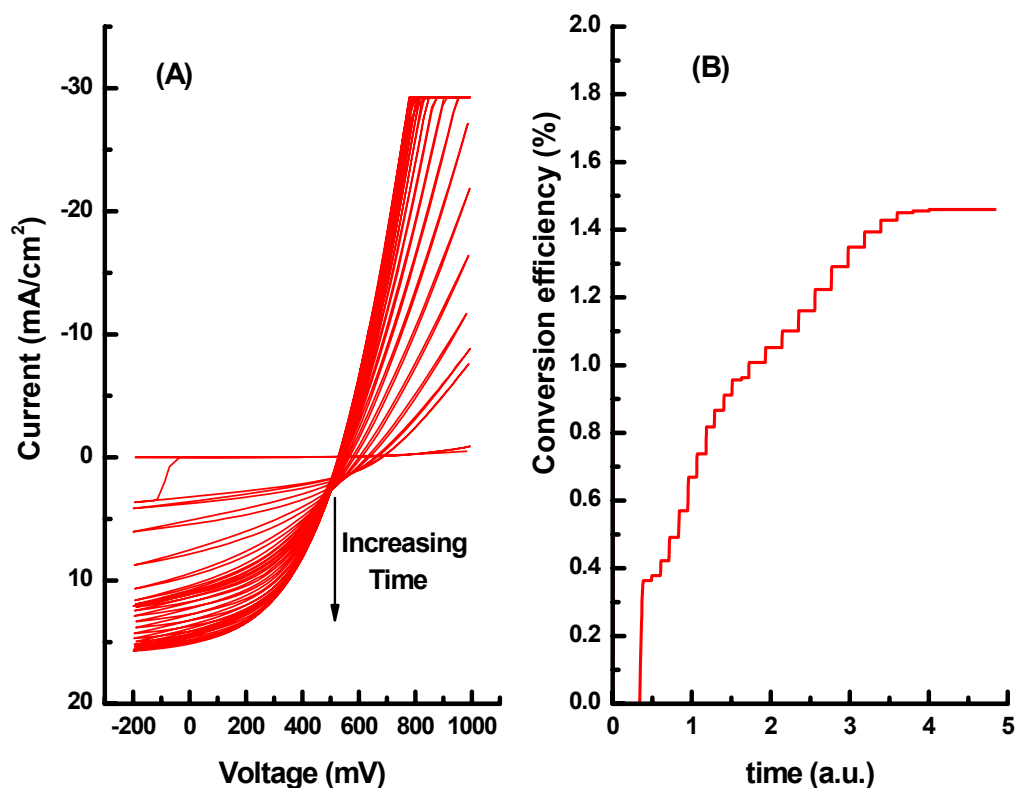


**Figure 2.6** Repeated I-V cycles under 2400 W/m<sup>2</sup> white light annealing (A) and evolution of conversion efficiency (B) for same P3HT:PCBM 1:1 device spin coated from 10 g/L chloroform solution.

### 2.4.3 Optimal P3HT:PCBM Ratio

There are contradictory reports on the optimal P3HT:PCBM ratio, with values ranging from 1:2 to 2:1. For instance, Inoue et al.<sup>22, 23</sup> reported an efficiency of 4% using a P3HT:PCBM ratio of 2:1 and toluene as the solvent. Chirvase et al.<sup>24</sup> reported an efficiency of ~2.4% with an optimum P3HT:PCBM ratio of 1:1 to 1:0.9 using chloroform as solvent. As the morphology of the phases is strongly dependent on processing conditions such as the solution concentration, solvent nature and annealing conditions, it is not surprising to find such discrepancies. The goal in all of these studies and for OPV devices in general is to maximize electron and hole mobilities by forming two inter-percolated phases of P3HT and PCBM while maintaining sufficient interfacial area to facilitate exciton dissociation and charge transfer. Also, the optimized P3HT:PCBM ratio can be determined by methods such as photoluminescence quenching<sup>6</sup> or measuring electron and hole mobilities,<sup>25</sup> but the correlations with actual device performance are not always straightforward. Since specific conditions vary from laboratory to laboratory, the only way to acquire certitude on the best composition was to perform a study on our own devices. We therefore tested three P3HT:PCBM compositions, 2:1, 3:2 and 1:1 and evaluated their device performance.

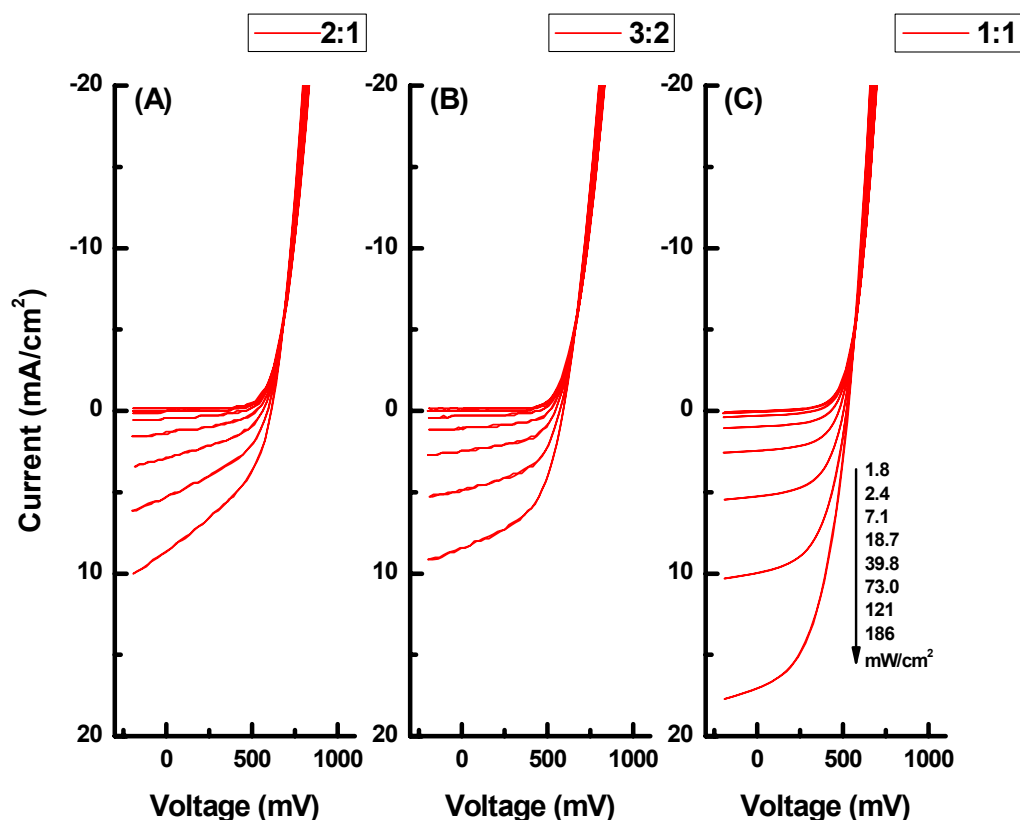


**Figure 2.7** I-V curves at various light intensities of ITO-PEDOT: PSS/P3HT: PCBM/In-Ga solar cells with P3HT: PCBM ratio of 2:1 (A), 3:2 (B) and 1:1 (C).

All devices were prepared on ITO coated glass with a layer of PEDOT:PSS as described in Section 2.2. P3HT:PCBM was deposited by spin coating at approximately 1000 rpm from 8-10 g/L chloroform solutions. The I-V characteristics of devices from the three compositions are shown in Figure 2.7. Eight measurements at varying light intensities are shown for each device. It can be clearly seen from the curves that the  $I_{sc}$  is dramatically higher for the 1:1 composition. The device characteristics obtained from the I-V curves are summarized in Table 2.2 and represent the best obtained for each composition. The maximum conversion efficiency we obtained was 2.1% at P3HT:



PCBM ratio of 1:1. These results are in good agreement with those published by Chirvase et al.<sup>24</sup>

**Table 2.2** Photovoltaic parameters efficiency ( $\eta$ ), fill factor (FF), short-circuit current (Isc) and open-circuit voltage (Voc) of P3HT: PCBM solar cells at various P3HT: PCBM ratios, measured under 100 mW/cm<sup>2</sup> halogen white light, with Ga-In top contact.

P3HT:PCBM Ratio	$\eta_{\text{halogen}}^*$ (%)	FF	Isc (mA/cm <sup>2</sup> )	Voc (mV)
2:1	0.98	0.39	4.31	588
3:2	1.23	0.48	4.7	561
1:1	2.14	0.52	8.0	515

#### 2.4.4 Comparing the Efficiencies Measured with a Halogen Light Source and with an A.M. 1.5 Solar Simulator

In order to correlate our measurements with those from other groups, we compared the results measured with an AM 1.5 simulator and evaporated Al contacts. We used the optimal formulation and spin coating conditions previously determined to fabricate additional devices. They were first annealed and tested under the halogen light source at 100 mW/cm<sup>2</sup>, then taken the next day to an Oriel Solar Simulator and measured again under 100 mW/ cm<sup>2</sup> (~1 sun). The I-V curves in Figure 2.8 clearly show similar photocurrents. The lower photocurrents with the A.M 1.5 solar simulator can be attributed to aging of the device (1 day) between the two measurements due to oxygen and moisture exposure, as is widely reported in the literature.<sup>26-29</sup>

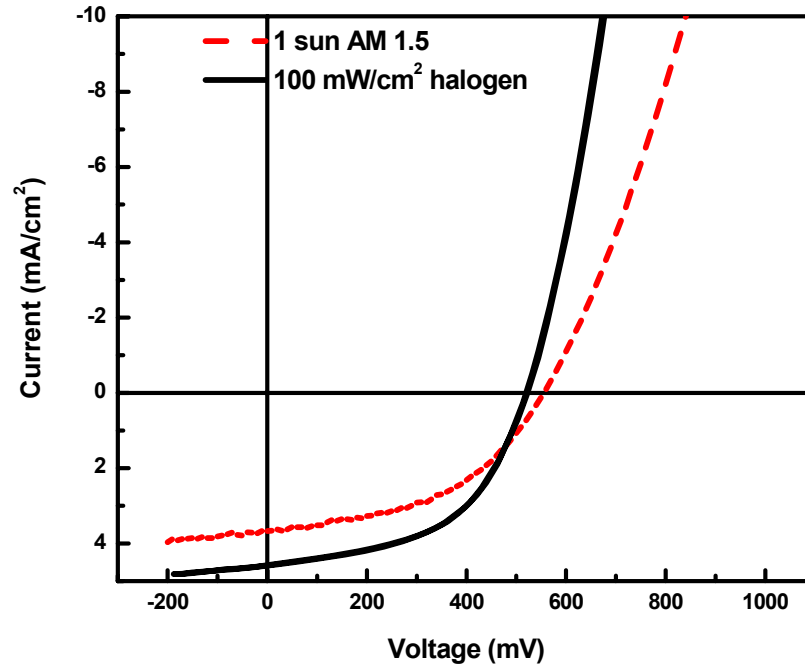


**Figure 2.8** I-V curves at  $100 \text{ mW/cm}^2$  of simulated sunlight for the same ITO/PEDOT:PSS/P3HT:PCBM 1:1/Ga device measured with a halogen light source (—) or under A.M. 1.5 conditions (---).

The solar cell parameters measured under the two light sources are summarized in Table 2.3. We observe a lower fill factor and lower  $I_{sc}$ , but higher  $V_{oc}$  with the solar simulator. These results in an efficiency of 0.89% versus 1.24% measured with the halogen light source. We conclude that our assumption that the fill factor did not change with wavelength was incorrect, and there is a spectral mismatch coefficient of  $\sim 0.71$  to correct the efficiency measured with the halogen light source.

**Table 2.3** Photovoltaic parameters efficiency ( $\eta$ ), fill factor (FF), short-circuit current ( $I_{sc}$ ) and open-circuit voltage ( $V_{oc}$ ) of the same P3HT: PCBM solar cell, measured under  $100 \text{ mW/cm}^2$  halogen white light or  $100 \text{ mW/cm}^2$  A.M. 1.5 solar simulator.

	$\eta$ (%)	FF	$I_{sc}$ ( $\text{mA/cm}^2$ )	$V_{oc}$ (mV)
AM 1.5 1 sun	0.89	0.46	3.65	560
Halogen 1 sun	1.24	0.51	4.55	530

### 2.4.5 Comparison of Evaporated Aluminum versus Ga-In Electrodes

We applied the previously described conditions to spin-coat more films, on which two  $0.24 \text{ cm}^2$  circular Al contacts were thermally evaporated, under less than  $10^{-6}$  torr vacuum. In order to obtain a fair comparison with the devices using In-Ga contact, approximately half of the P3HT:PCBM surface on each device was left undisturbed so that it could be tested with Ga-In contacts. Then, the devices were tested with an Oriel Solar simulator under  $100 \text{ mW/cm}^2$  light intensity, using either Al or Ga-In contacts. The I-V plots from devices with the two different contacts are plotted in Figure 2.9. From our results, we systematically observed an increase in short-circuit current and higher open-circuit-voltage with the aluminum contacts, but lower fill factors.

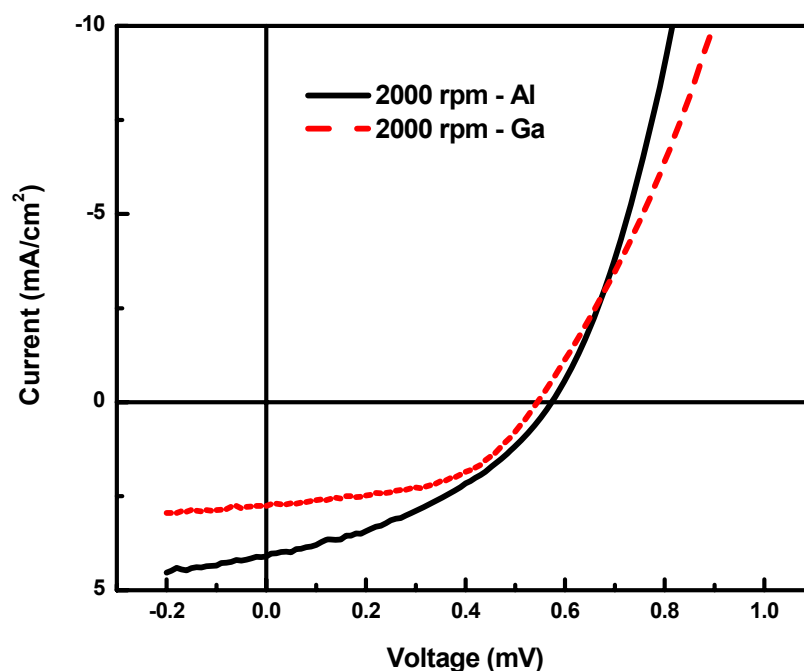


**Figure 2.9** I-V curves at  $100 \text{ mW/cm}^2$  of A.M 1.5 simulated sunlight for the same ITO/PEDOT:PSS/P3HT:PCBM 1:1/Ga device measured with aluminum top contact (—) or Ga-In top contact (---).

The fill factor deviation between the two devices could be attributed to the active area difference ( $0.07 \text{ cm}^2$  for Ga-In versus  $0.24 \text{ cm}^2$  for Al), because the series resistance decreases the fill factor in larger area devices. These differences, summarized in Table 2.4, resulted in overall higher efficiencies measured with the Al top contact.

**Table 2.4** Photovoltaic parameters efficiency ( $\eta$ ), fill factor (FF), short-circuit current (Isc) and open-circuit voltage (Voc) of the same P3HT: PCBM solar cell, measured under  $100 \text{ mW/cm}^2$  A.M. 1.5 solar simulator, using either an Al or Ga-In top contact.

	$\eta$ (%)	FF	Isc ( $\text{mA/cm}^2$ )	Voc (mV)
Al contact	0.97	0.38	4.02	580
Ga-In contact	0.82	0.51	2.71	550

## 2.5 Conclusion

We have demonstrated that cells can be tested with an inexpensive white halogen lamp which resulted in overestimated values of the conversion efficiency. We attributed this to the fact that the spectrum of halogen light source is a better match to the absorption of P3HT:PCBM than the AM 1.5 spectrum. A methodology to correct these values by using sunlight and a multi-meter was developed. On the other hand, we found that devices measured with an Al top contact yielded higher efficiencies than those measured with a Ga-In top contact. While finished devices cannot use a Ga-In top contact, its use at the research laboratory is extremely convenient for fast characterization of photovoltaic effect in bulk heterojunctions. This enables rapid evaluation of optimal device composition and depositions conditions. Then, aluminum evaporation can be used to generate finished prototypes and test them under A.M. 1.5 simulated solar conditions.

## 2.6 References

- <sup>1</sup> C. J. Brabec, Solar Energy Materials & Solar Cells **83**, 273–292 (2004).
- <sup>2</sup> T. M. Brown, J. S. Kim, R. H. Friend, et al., Applied Physics Letters **75**, 1679 (1999).
- <sup>3</sup> M. K. Fung, S. L. Lai, S. W. Tong, et al., Applied Physics Letters **81**, 1497 (2002).
- <sup>4</sup> E. Bundgaard and F. C. Krebs, Solar Energy Materials and Solar Cells **91**, 954 (2007).
- <sup>5</sup> L. J. A. Koster, V. D. Mihailetschi, and P. W. M. Blom, Applied Physics Letters **88**, 093511 (2006).
- <sup>6</sup> D. Chirvase, Z. Chiguvare, M. Knipper, et al., Synthetic Metals **138**, 299 (2003).
- <sup>7</sup> N. Camaioni, G. Ridolfi, G. Casalbore-Miceli, et al., Advanced Materials **14**, 1735 (2002).
- <sup>8</sup> Y. Kim, S. A. Choulis, J. Nelson, et al., Journal Of Materials Science **40**, 1371 (2005).
- <sup>9</sup> Y. Kim, S. A. Choulis, J. Nelson, et al., Applied Physics Letters **86**, N.PAG (2005).
- <sup>10</sup> M. Reyes-Reyes, K. Kim, and D. L. Carroll, Applied Physics Letters **87** (2005).
- <sup>11</sup> T. Erb, U. Zhokhavets, G. Gobsch, et al., Advanced Functional Materials **15**, 1193 (2005).
- <sup>12</sup> J. Huang, G. Li, and Y. Yang, Applied Physics Letters **87**, 112105 (2005).
- <sup>13</sup> H. Kim, W.-W. So, and S.-J. Moon, Solar Energy Materials and Solar Cells **91**, 581 (2007).
- <sup>14</sup> Y. Kim, E. Oh, H. Lim, et al., Applied Physics Letters **88** (2006).
- <sup>15</sup> W. Ma, C. Yang, X. Gong, et al., Advanced Functional Materials **15**, 1617 (2005).
- <sup>16</sup> F. Padinger, R. S. Rittberger, and N. S. Sariciftci, Advanced Functional Materials **13**, 85 (2003).
- <sup>17</sup> X. N. Yang, J. Loos, S. C. Veenstra, et al., Nano Letters **5**, 579 (2005).
- <sup>18</sup> J. K. J. van Duren, X. Yang, J. Loos, et al., Advanced Functional Materials **14**, 425 (2004).

- <sup>19</sup> G. Li, V. Shrotriya, Y. Yao, et al., *Journal of Applied Physics* **98**, 043704 (2005).
- <sup>20</sup> C. J. Brabec, V. Dyakonov, J. Parisi, et al., *Organic Photovoltaics: Concepts and Realization* (Springer-Verlag, Heidelberg, 2003).
- <sup>21</sup> S.-S. Sun and N. S. Sariciftci, *Organic photovoltaics; mechanisms, materials, and devices* (Taylor & Francis, London, 2005).
- <sup>22</sup> K. Inoue, R. Ulbricht, P. C. Madakasira, et al., *Synthetic Metals* **154**, 41 (2005).
- <sup>23</sup> K. Inoue, R. Ulbricht, P. C. Madakasira, et al. *Material Research Society Symposium Proceedings* (2004), 836
- <sup>24</sup> D. Chirvase, J. Parisi, J. C. Hummelen, et al., *Nanotechnology* **15**, 1317 (2004).
- <sup>25</sup> E. von Hauff, V. Dyakonov, and J. Parisi, *Solar Energy Materials & Solar Cells* **87**, 149 (2005).
- <sup>26</sup> K. Kawanoa, R. Pacios, D. Poplavskyy, et al., *Solar Energy Materials & Solar Cells* **90**, 3520 (2006).
- <sup>27</sup> J. C. Hummelen, J. Knol, and L. Sanchez, *Proceedings of SPIE* **4108**, 76 (2001).
- <sup>28</sup> F. C. Krebsa, J. E. Carle', N. Cruys-Bagger, et al., *Solar Energy Materials & Solar Cells* **86**, 499 (2004).
- <sup>29</sup> H. Neugebauer, C. Brabec, J. C. Hummelen, et al., *Solar Energy Materials & Solar Cells* **61**, 35 (2000).

## Chapter 3

### Investigation of Nanoscale Morphological Changes in Organic Photovoltaics during Solvent Vapor Annealing

#### 3.1 Introduction

The motivation for this thesis is that organic photovoltaics are promising alternatives to their inorganic counterparts<sup>1</sup> because if they can be prepared simply from solution on inexpensive substrates then the economic benefits should compensate for their lower efficiency. As has been described in Chapter 1 and 2, the most successful organic photovoltaic system to date exploits the properties of the soluble fullerene derivative, phenyl-C<sub>61</sub>-butyric acid methyl ester (PCBM), as an electron acceptor and a conducting polymer, poly(3-hexylthiophene) (P3HT), as an electron donor.<sup>1-14</sup> Efficiencies of solar cells based on bulk heterojunctions of P3HT and PCBM have been reported to range from 3-5%<sup>7,9</sup> when devices are prepared on rigid substrates in inert environments. There is great experimental interest in P3HT:PCBM and other organic photovoltaic devices because theoretical studies have predicted efficiencies as high as 11%.<sup>15</sup>

As was shown in Chapter 2 and by others,<sup>9, 16, 17</sup> thermal annealing of P3HT:PCBM bulk heterojunction devices is a critical step for improving their efficiency. It has been demonstrated (through post experimental analysis) that thermal annealing strongly affects the morphology of the nanocomposite layer via de-mixing of PCBM<sup>18</sup> and stacking of P3HT in coplanar conjugated segments.<sup>4</sup> In thermal annealing, relatively high temperatures ranging from 120 °C to 150 °C are often used,<sup>1, 2, 9, 17</sup> which limits the use of some inexpensive plastic substrates, such as polystyrene and acetates.

Recently, Dickey et al<sup>19</sup> reported an improvement in the performance of organic 3-ethyl-silylethynyl anthradithiophene (TES ADT) transistors via room temperature solvent vapor annealing (that is, exposing the deposited organic layers to solvent vapor). The beneficial effect of better structural order attained in TES ADT through solvent vapor annealing at room temperature suggests that the same method could also improve the performance of P3HT:PCBM solar cells. Indeed, recently it has been reported that exposing P3HT:PCBM photovoltaic devices to solvent vapor along with a subsequent thermal annealing step leads to an improvement in efficiency.<sup>20</sup> The improvement is better than thermal annealing alone. It has also been demonstrated that slow evaporation of the solvent leads to a dramatic improvement in performance.<sup>7</sup> The latter may be comparable to solvent vapor annealing since the slow evaporation soaks the organic layer in the solvent vapor, allowing the P3HT:PCBM to rearrange in an ordered manner. Electroluminescence of P3HT has also been shown to improve with exposure to  $\text{CHCl}_3$  vapor.<sup>21</sup> However, although the use of solvent vapor annealing to improve device performance has been previously reported, little is known about any morphological transformations that may occur during such a process, and on the spectroscopic signatures which might be used to recognize them.

In this Chapter, the mechanisms responsible for the improvement in P3HT:PCBM photovoltaic cell efficiency by solvent vapor annealing are elucidated. *In-situ* Raman and photoluminescence spectroscopies were utilized to monitor structural and optoelectronic changes in the P3HT:PCBM during the annealing. In addition, *ex-situ* ultraviolet-visible (UV-Vis) spectroscopy and atomic force microscopy (AFM) were employed to characterize the P3HT:PCBM nano-composites. Specifically, the



structural changes occurring during solvent vapor annealing of P3HT:PCBM solar cells in solvent vapor at room temperature are described. The efficiencies of the devices tested in this study increased from 0.8% (for as fabricated devices) to 2.6% (with some devices achieving efficiencies up to 3.0%) after solvent vapor annealing. These values are comparable to those routinely obtained after thermal annealing. Furthermore, both the morphological changes and the maximum efficiency of P3HT:PCBM devices were found to saturate within 30 seconds to 3 minutes of exposure to the solvent vapor.

### **3.2 Characterization Techniques**

In Chapter 2, the importance of the processing parameters on P3HT:PCBM organic photovoltaics (OPVs) were demonstrated. In particular, thermal annealing was shown to be a critical process resulting in the morphological changes necessary to achieve high efficiencies. One of the objectives of this chapter is to understand the morphological changes occurring in the P3HT:PCBM layer by using a number of characterization techniques, including Raman spectroscopy, photoluminescence spectroscopy, atomic force microscopy and UV-Vis spectroscopy. In order to adequately interpret the data obtained from these analytical techniques, it is important to understand the basic mechanisms governing the operation of each. Below, we describe each technique in sufficient detail so that subsequently presented data can be easily interpreted.

### 3.2.1 Raman Spectroscopy

Raman spectroscopy is a powerful technique for understanding molecular composition and structure of materials. This technique measures the wavelength and intensity of inelastically scattered light from the sample to obtain information about the rotational and vibrational modes of the material. When a sample is illuminated with a monochromatic light source, most of the scattering occurs elastically (Rayleigh scattering, see Figure 3.1), but a small number of incident photons are inelastically scattered, undergoing an energy gain or loss associated with the vibrational energy of the material. This process occurs when incident photons interact with the electrons in the sample, exciting them to higher virtual energy levels. Figure 3.1 shows the basic scattering process for a single vibration. The scattering process starts with the excitation of the ground level vibrational state to a higher energy state and the subsequent decay to an excited level vibrational state. When this occurs, the scattered light has lost energy to lattice vibration. This is referred to as Stokes scattering (see green and red arrows in Figure 3.1) and the associated change in energy or wavelength is referred to as the Stokes shift. Inversely, when the scattering process starts with an excited level vibrational state and the subsequent decay to the ground level vibrational state, the scattered light has gained energy from the lattice. This is referred to as anti-Stokes scattering and the associated change in energy or wavelength is referred to as the anti-Stokes shift,<sup>22, 23</sup> as indicated by the green and blue arrows in Figure 3.1.

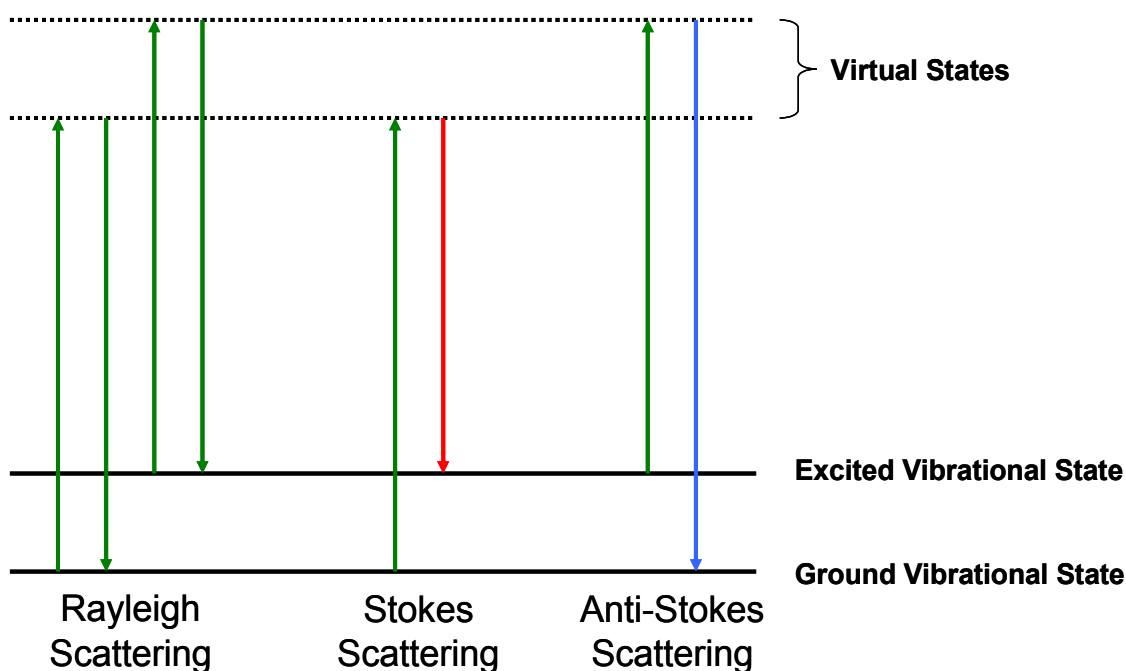


**Figure 3.1** Diagram shows the basic scattering process for a single vibration. The energy of Rayleigh scattered light is equal to the incident light. Stokes and anti-Stokes scattered light is less and greater, respectively, than the incident light by the difference between the ground and excited vibrational states.<sup>22, 23</sup>

Due to the dynamics of the scattering process, Raman scattering is considerably weaker than Rayleigh scattering, where only one in every  $10^6$ - $10^8$  photons which scatter are Raman scattered. Furthermore, as the majority of atoms or molecules are expected to be in the ground vibrational state at room temperature, as predicted by the Boltzmann equation, anti-Stokes scattering is generally weaker than Stokes scattering.<sup>23</sup>

Complex molecules have multiple vibrational modes which are determined by the number of vibrational degrees of freedom, given by the formula  $3N-6$  for all molecules (except  $3N-5$  for linear molecules), where  $N$  is the number of atoms in the molecule.<sup>23</sup> Not all vibrational modes are Raman active. The basic selection rule is that if a vibration results in a change in the polarizability of a molecule, then that mode will

generally be Raman active. If a vibration results in a change in a molecules dipole moment, then the mode is considered infrared (IR) active.

As complex molecules are often made up of many more common groups of atoms with known chemical bonds (aromatic C-H, C=C, for example), the basic “fingerprint” of a molecules may be identified through the existence of specific Raman bands with relative intensities specific to that molecule. This can be demonstrated by viewing the Raman spectrum of a P3HT thin film on poly(ethylene terephthalate) (PET) shown in Figure 3.2. The peaks related to specific bonds and vibrational modes can be clearly observed, giving the overall fingerprint of P3HT. However, Raman peaks of PET are also observed in the spectrum. Therefore, often it is necessary to perform Raman spectroscopy on the substrate alone in order to identify the peaks from the sample. Alternatively, a non-Raman active substrate can be chosen. In addition to verifying or determining molecular structure, the width of Raman peaks can provide information regarding the ordering of molecules. Disordered materials contain unique components which each contribute a portion of the Raman signal which, when averaged, form the single broad peak observed. Therefore, broader peaks, measured at their full width half maximum (FWHM), generally indicate higher levels of disorder in a system, whereas, sharp peaks are generally indicative of high levels of crystallinity. Alternatively, ordered structures generally have a Lorentzian profile and with increasing disorder, the peaks assume a greater Gaussian component.<sup>24, 25</sup> As P3HT is a highly crystalline polymer, the peaks shown in Figure 3.2 primarily have a Lorentzian profile.

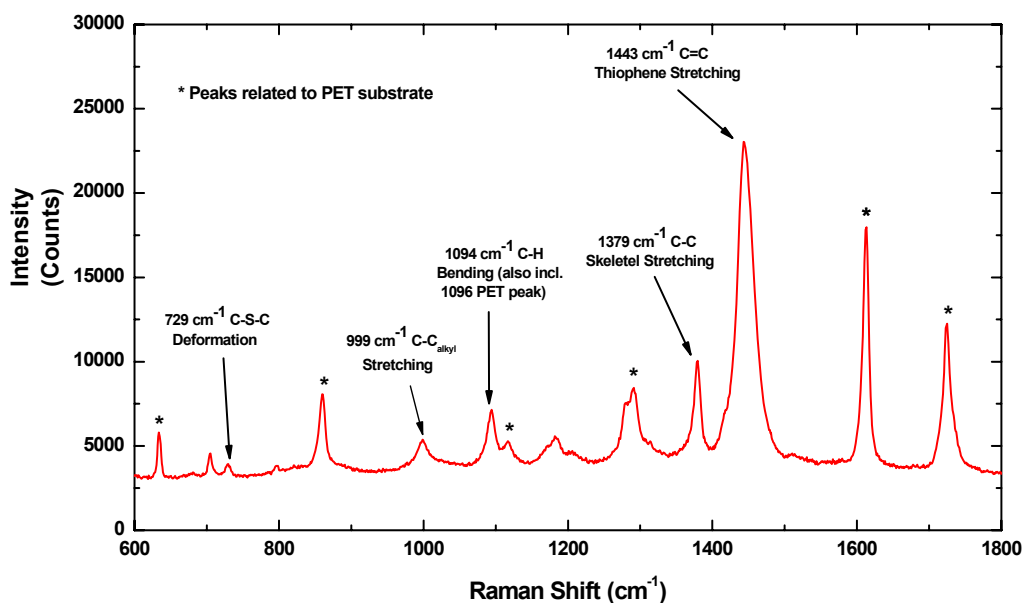


**Figure 3.2** Raman spectrum of a P3HT thin film on a PET substrate. The characteristic Raman active bands of P3HT and the chemical bond(s) associated with their origin are indicated.<sup>24, 26</sup> Raman active bands of PET are indicated with an asterisk.<sup>27</sup>

### 3.2.2 Photoluminescence

Photoluminescence (PL) is the process where the absorption of photons leads to excitation of electrons (referred to as photoexcitation), resulting in the emission of light by a material when the photoexcited electrons decay back to the ground state. The relaxation back to the equilibrium state can occur through either a radiative or non-radiative process. By measuring the energy level of the radiative decay, the band gap and other mid gap (such as defect induced states) energy levels may be identified. Differences between the excitation energy and the resulting PL also provide insight into electronic states, such as exciton decay mechanisms and polaron-exciton binding energies.<sup>28, 29</sup> Since the intensity of PL depends on the dominance of radiative recombination over non-radiative recombination, changes in intensity provide

information regarding the structure of materials and defect levels. PL in conjugated polymers such as P3HT is particularly useful for evaluating their performance in organic electronics. Since charge carriers in P3HT begin as excitons, their recombination or dissociation can be monitored by PL. In organic light emitting diodes (OLEDs), recombination of the electron-hole pair is highly desirable. Thus, the degree of recombination can be determined by PL. In organic photovoltaics, the opposite process is desirable. In order for power to be generated, the created exciton must be dissociated so that current can flow. Therefore, in OPVs, monitoring the PL gives invaluable information regarding the effectiveness of the bulk heterojunction towards exciton dissociation. Thus, in OLEDs, PL enhancement is desired, while in OPVs, PL quenching is the key to achieving high efficiency devices.

### 3.2.3 UV-Vis Spectroscopy

Ultraviolet-visible (UV-Vis) is the spectroscopy of photons in the ultraviolet and visible region of the electromagnetic spectrum. For the purposes of our work, the ultraviolet portion of the spectrum is limited to ~200-400nm in wavelength and the visible portion of the spectrum is from ~400-700nm. Many organic molecules absorb light in the ultraviolet and visible regions. Thus, the absorption spectra can provide information regarding electronic transitions, bandgap and chromic effects.<sup>30</sup> Most UV-Vis absorption in polymers is the result of  $\pi \rightarrow \pi^*$  transitions which require a significantly lower photon energy than  $\sigma \rightarrow \sigma^*$  transitions which occur at energies well above the UV-Vis range. In the case of conjugated polymers, such as P3HT, increased conjugation length results in more delocalized  $\pi$  electrons which decreases the gap

between the HOMO and LUMO levels (the  $\pi \rightarrow \pi^*$  transition energy). This leads to a red shift in the absorption characteristics of P3HT. Since conjugation length is effected by factors such as molecular weight and chain defects, UV-Vis spectroscopy can be an effective tool for evaluating the concentration of trap states and structural integrity.<sup>31</sup>

UV-Vis spectroscopy can also be used in understanding the regioregularity of P3HT. Head-to-tail (HT) regioregular P3HT assumes a more rod-like conformation and, hence, has a longer conjugation length.<sup>30, 32, 33</sup> Thus, the UV-Vis absorption spectra appears red shifted with increasing regioregularity. Additionally, since regioregular P3HT is a coplanar polymer, it has been suggested that ordering of the polymer results in increased inter-chain interactions which increase delocalization of  $\pi$  electrons and decrease the bandgap.<sup>34</sup>

### **3.2.4 Atomic Force Microscopy**

The atomic force microscope (AFM) provides high resolution topographical images of materials. It can have a spatial resolution of less than 1nm and relies on the forces between the AFM tip and the sample to produce images. The sharpness of the AFM tip directly affects the image resolution and typically has a radius of curvature from a few to tens of nanometers. When the tip of the AFM is brought within close proximity of the sample surface, the forces between the tip and sample cause the cantilever to deflect.<sup>35-37</sup> Changes in the surface topography and material result in changes in the cantilever deflection which is measured by reflecting a laser beam onto a photodetector. A piezoelectric scanner rasters the sample underneath the tip, providing

surface topography in the x, y and z-directions. A schematic of an AFM is shown in Figure 3.3.

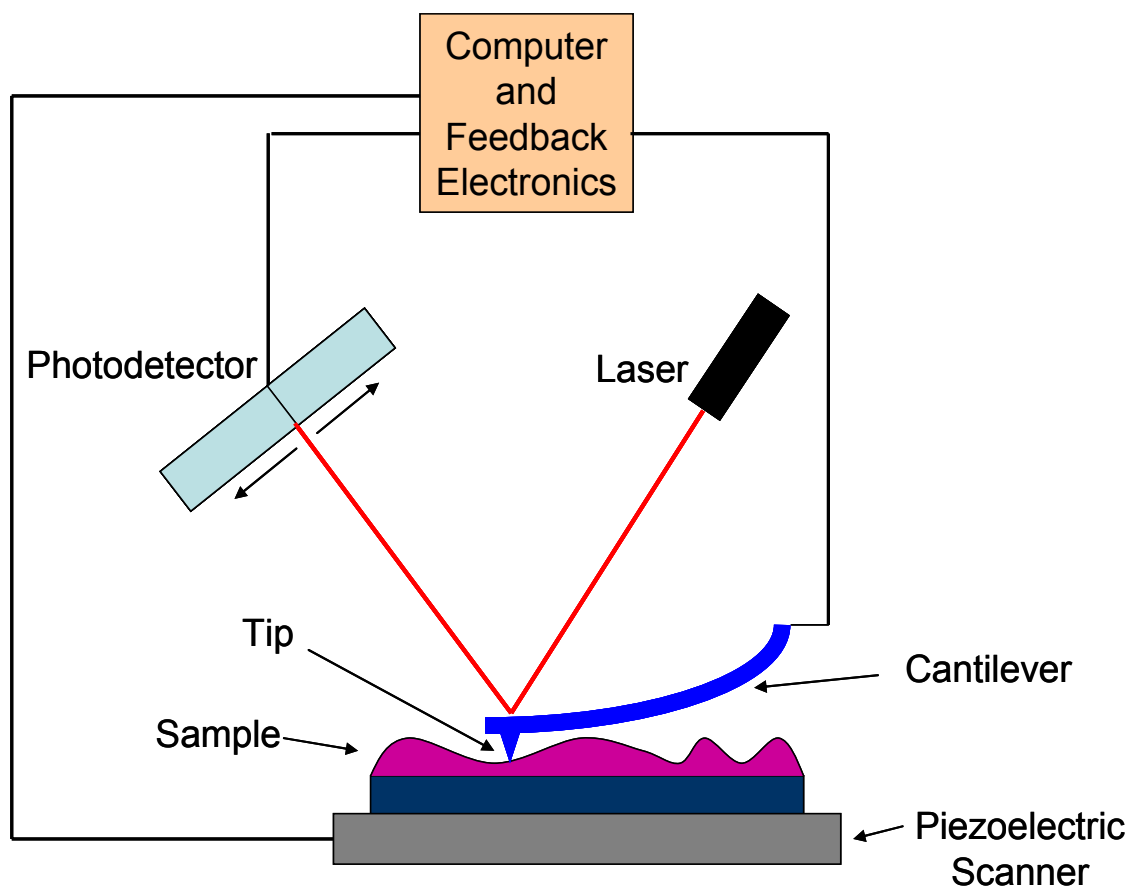


**Figure 3.3** Schematic of atomic force microscope. Raster scanning of the tip and cantilever over a sample surface results in a topographical map of the sample with nanometer resolution.

Since large changes in surface height could result in the collision of the tip and the sample surface, the AFM relies on a feedback loop and the piezoelectric scanner to maintain a constant force on the cantilever.<sup>36, 37</sup> Two of the most common modes of AFM use are contact and tapping. In contact mode, the tip of the AFM is brought into contact with the sample surface and a constant deflection is maintained while the raster-scan is performed. Because the tip is in contact, this method utilizes cantilevers with low spring constants. Contact mode is generally not a good choice for sample which



are highly attractive, such as wet or soft surfaces found in polymeric or biological samples.<sup>35, 36</sup> In tapping mode, also referred to as dynamic force mode, the tip is oscillated above the surface sample. Through the feedback loop, constant frequency, amplitude and phase of the cantilever are maintained. Changes in topography and material affect the tip-sample interaction and, therefore, the phase and amplitude of the cantilever oscillation changes. Through changes brought about by the feedback loop, information about the sample can be obtained. Tapping mode AFM utilizes cantilevers with high force constants, and are good for high lateral resolution and soft samples.<sup>35-37</sup> As the P3HT:PCBM system is relatively soft, tapping mode AFM was utilized in this work. AFM is an effective tool for determining surface roughness which may lead to information regarding the formation of component domains in the nanostructure of the P3HT:PCBM system. We have used the AFM extensively to characterize our samples.

Having described the analytical techniques used in this phase of the study, we now provide details of our work related to solvent vapor annealing of P3HT:PCBM OPV devices. First, the details of the *in-situ* experimental set-up that was especially designed for this work are described. The simple set-up allowed us to perform *in-situ* PL and Raman spectroscopy while doing the solvent vapor annealing. This allowed us to monitor in real time both the structural and electronic changes occurring in the P3HT:PCBM layer. After the experimental details section, results of PL and Raman spectroscopies are detailed. Correlation of the *in-situ* spectroscopic data and *ex-situ* AFM and UV-Vis data to OPV device characteristics are described thoroughly. Finally, a model for charge transport is proposed to summarize our observations.

### 3.3 Experimental Details

The OPV devices used to study the effects of solvent vapor annealing were prepared by depositing a mixture of as-received P3HT (Electronic grade, regioregularity 98.5%, Rieke Metals, Inc.) and PCBM (purity > 99.5%, American Dye Source, Inc.) on to indium-tin oxide (ITO) layer ( $<20 \text{ } \Omega/\square$  resistance,  $>85\%$  transmittance) on Poly(ethylene terephthalate) and glass substrates covered with a 50-nm thick poly(3,4-ethylene dioxy-thiophene):poly(styrenesulfonate) (PEDOT:PSS) layer. Specifically, a 10 mg/mL solution at 1:1 weight ratio of P3HT to PCBM in chloroform or chlorobenzene was spin-coated at 1000 rpm, resulting in a 100 – 120 nm active layer. Thermally evaporated aluminum was used for the top contact electrodes. The photovoltaic characteristics were evaluated under a Newport AM1.5 solar simulator operated at  $100 \text{ mW/cm}^2$ . External quantum efficiency (EQE) measurements were performed using a halogen light source with an Oriel Cornerstone 130 monochromator and Newport 1830-C power meter.

The *in-situ* morphological and optoelectronic changes in the P3HT:PCBM layers while being exposed to the solvent vapor were observed by monitoring the changes in the Raman and PL features using a Renishaw inVia spectrometer operating at 1.57 eV excitation (power: 1mW). Each spectrum was recorded using a 3 second integration time and care was taken to avoid laser soaking of the sample. The experimental configuration used to perform solvent vapor annealing while simultaneously measuring the PL and Raman features is shown in Figure 3.4. A special sample holder was fabricated in which the substrate was placed upside down in the top cap of a Petri dish filled with the solvent. This allowed the laser to pass through the

PET and ITO layers from the top to the P3HT:PCBM layer while being exposed to the solvent vapor. The choice of a low excitation energy ( $E_i = 1.57$  eV)

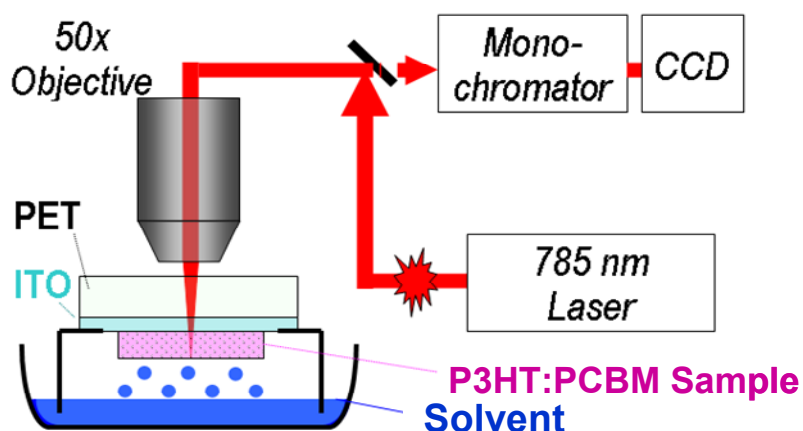


**Figure 3.4** Schematic of the experimental configuration used to perform solvent vapor annealing while simultaneously measuring the PL and Raman features.

strongly favors the observation of the Raman and PL arising from P3HT while suppressing the PL from PCBM which has a much larger optical gap. While 1.57 eV is below the optical absorption edge of P3HT<sup>38</sup>, a broad PL background was identified in both P3HT and P3HT:PCBM samples. Control measurements on PET, ITO and PCBM alone were performed in order to discount the contribution to the PL from these materials in the system. No similar background could be identified in any material other than P3HT. Additionally, all measurements were repeated after annealed samples had been thoroughly dried in air to ensure that there was no contribution to the PL from the solvent. Although the exact origin of the PL in P3HT using 1.57 eV excitation is debatable, it has been shown that a material may be weakly absorbing due to mid-gap defect mediated states resulting in subsequent radiative decay (PL).<sup>39-41</sup> As shown by the blue curves in Figure 3.5, the intensity of the P3HT:PCBM PL background varied sub-linearly with laser power in the 0.05-5 mW range when 1.57 eV excitation was used.

Since the excitation energy was less than the bandgap of P3HT ( $\sim 2\text{eV}$ ), the sub-linear relationship suggests the initial saturation of mid-gap defect mediated states.<sup>39-41</sup> The red curves in Figure 3.5 shows a linear relationship between the PL background and laser power when using  $1.96\text{eV}$  excitation, which is close to the P3HT bandgap, suggesting the PL is the direct result the materials bandgap. Upon solvent vapor annealing, this curve shifts upward, but remains linear, which is consistent with increased absorption of the excitation laser due to a decrease in the P3HT bandgap upon annealing. Specific values for the P3HT bandgap and changes following solvent vapor annealing are discussed in Section 3.4.2. By utilizing the  $1.57\text{eV}$  laser, changes in defect levels and ordering of P3HT could be observed. In Figure 3.5 it can be seen that for the  $1.57\text{eV}$  excitation the curve shifts downward with solvent vapor annealing which is indicative of decreased defects levels and increased ordering in the P3HT. Further discussion of the suppression of the PL is presented in Section 3.4.4.

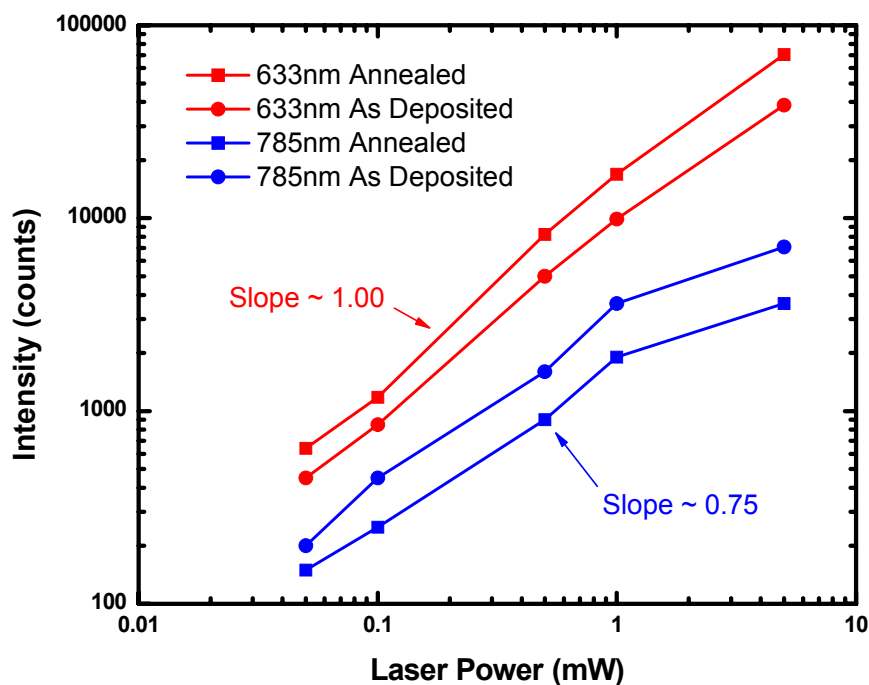


**Figure 3.5** Log-log plot of PL intensity vs. laser excitation power for P3HT:PCBM thin films. The red plots show a linear relationship between PL and laser power using 633nm (1.96eV) excitation (close to the P3HT bandgap). The blue plots show a sub-linear relationship using 785nm (1.57eV) excitation (less than the P3HT bandgap), suggesting PL is the result of defect mediated states.

PL in conjugated thiophenes has been suggested<sup>29, 31, 42</sup> to arise from radiative recombination of polaron-exciton pairs into Franck-Condon (FC) states, as sketched in Figure 3.6. As a result of the absorption of a photon, an electron is promoted from the lowest vibrational level of the P3HT ground (or equilibrium) state ( $S_0(\text{eq})$ ) to a higher vibrational level of the P3HT excited state ( $S_1(\text{FC})$ ). A rearrangement of its nuclear geometry causes the P3HT to immediately dissipate some energy as the electron reaches the lowest vibrational level of the P3HT excited state ( $S_1(\text{eq})$ ). When the P3HT relaxes to the ground state, it does so to higher vibrational level ( $S_0(\text{FC})$ ), emitting a photon with a lower energy (PL) than the absorbing energy. Therefore, the shift of the PL peak

with respect to the excitation energy provides information about the polaron-exciton binding energy, ( $2U$ , as indicated in Figure 3.6).<sup>29</sup> Thus, PL spectroscopy can be a powerful tool for the investigation of the nature, the binding energy, and the degree of confinement of the electronic states in photoexcited P3HT. It should be noted that for some of our *in-situ* Raman and PL measurements reported here, the PEDOT:PSS layer was omitted in order to avoid masking of P3HT features which overlap with those of PEDOT. Additional films of pure P3HT were also deposited and analyzed for comparison. Tapping mode atomic force microscopy (AFM) (Digital Instruments Nanoscope) and optoelectronic measurements (using a Perkin-Elmer Lambda 20 transmittance spectrophotometer for the solutions and a Jobin-Yvon UVISEL spectral ellipsometer coupled with a multilayer model for the solid films) were also performed.

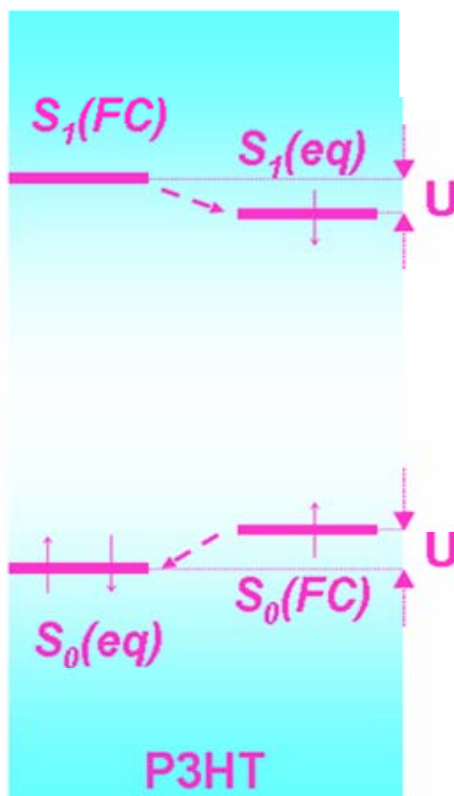


**Figure 3.6** Schematic of radiative recombination mechanism of polaron-exciton pairs into Franck-Condon (FC) states (adapted from Ref. <sup>29</sup>). Changes in P3HT nuclear geometry upon excitation to the Franck-Condon excited state ( $S_1(\text{FC})$ ) result in the formation of a new equilibrium excited state ( $S_1(\text{eq})$ ) and the subsequent decay to  $S_0(\text{FC})$  resulting in PL are shown. The total difference between the equilibrium and Franck-Condon levels is the polaron-exciton correlation energy ( $2U$ ).

### 3.4 Results

#### 3.4.1 Photovoltaic Efficiencies

The current density versus voltage curves under AM1.5 illumination ( $100 \text{ mW/cm}^2$ ) for a photovoltaic device fabricated and solvent vapor annealed using chlorobenzene are shown in Figure 3.7(a). Similar characteristics and improvements in efficiency were also obtained for devices fabricated with and annealed in chloroform. Typical diode characteristics are observed for before and after solvent annealing

measurements. A close observation of the high current region at positive voltages indicates that the vapor annealing leads to an improvement in transport due to ordering of the P3HT (see discussion below). The short circuit current increases by more than two fold (from  $\sim 4.4$  to  $10.9 \text{ mA/cm}^2$ ) while the fill factor increased from 36% to 44%, resulting in an efficiency of approximately 2.6%, comparable to other reports in the literature.<sup>20</sup> Efficiency of thermally annealed (performed under standard conditions up to  $140^\circ\text{C}$  as described in ref.<sup>43</sup>) devices was approximately 2.8%.

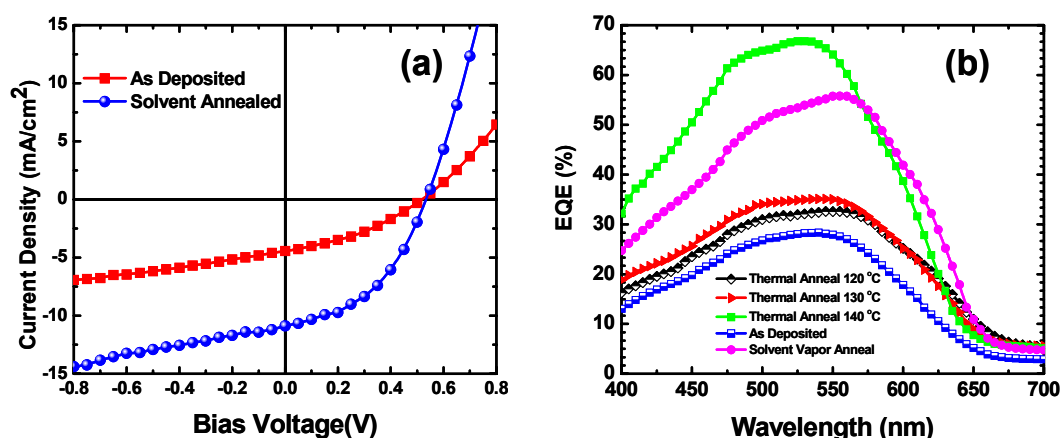


**Figure 3.7** (a) Current density versus the voltage plot for P3HT:PCBM photovoltaic devices before (red squares) and after 2 minutes of solvent vapor annealing (blue circles). (b) External quantum efficiency (EQE) measurements for as deposited, solvent annealed and thermally annealed devices.

The EQE measurements for as deposited, solvent annealed and thermally annealed devices are plotted in Figure 3.7(b). The solvent annealed device shows a maximum EQE of  $\sim 56\%$  (at  $555 \text{ nm}$ ), twice that of the as deposited device which had an EQE of  $\sim 28\%$  (at  $540 \text{ nm}$ ). Similar improvements in EQE can be seen across the entire spectrum below approximately  $650 \text{ nm}$  which suggests improved exciton dissociation and charge transport attributable to increased order in the matrix. While



the maximum EQE for a thermally annealed device was  $\sim 67\%$ , this device required an annealing temperature of  $140^{\circ}\text{C}$  which may not be suitable for most flexible substrates without incurring damage or degrading the material life expectancy. EQE measurements for devices thermally annealed at temperatures less than  $140^{\circ}\text{C}$  were lower than those for solvent annealed devices, as shown in Figure 3.7(b). The highest power conversion efficiency values were obtained on ITO/glass substrates for both annealing treatments. It must also be mentioned that of the numerous devices we tested, both types of annealing treatments (thermal and solvent vapor) yielded similar improvements in efficiency. The maximum value of efficiency we obtained was  $3\%$  but most devices yielded values of  $\sim 2.6\%$ . We have found that efficiencies of devices prepared under similar conditions can vary from  $2.0\%$  to  $3.0\%$ . The wide variation in device performance is typical for our devices and likely related to factors such as aging of raw materials and exposure to air during measurements.

### 3.4.2 UV-Vis Spectroscopy

Information on the mechanism responsible for the enhancement in efficiency by solvent vapor annealing can be inferred from optical characterization. Qualitatively, it was observed that the color of P3HT films spin-coated in the absence of PCBM is purple and does not change upon solvent vapor annealing. In contrast, the P3HT:PCBM films are orange immediately after spin coating but become purple during the first 30 seconds of solvent vapor annealing. These effects can be quantitatively verified using UV-Vis absorption spectroscopy. The optical absorption spectra of as deposited thin films and their respective starting solutions are compared in Figure 3.8(a).

It can be observed that the absorption edges of the P3HT:PCBM solution and thin films are similar. In contrast, the optical absorption edge of the P3HT films is strongly red-shifted. The effect of solvent vapor annealing on the absorption spectra of the thin films is compared in Figure 3.8(b). It can be seen that the spectra of pure P3HT, which are red-shifted during solidification (Figure 3.8(a)), are insensitive to solvent vapor annealing. In contrast, for the P3HT:PCBM films the absorption coefficient above  $\sim 510\text{nm}$  is observed to red-shift upon solvent vapor annealing and is comparable to that of pure P3HT. It can also be observed from Figure 3.8(b) that the absorption features related to PCBM do not change upon solvent vapor annealing and are present only below  $400\text{ nm}$  (i.e.  $> 3\text{ eV}$ ).<sup>34</sup>

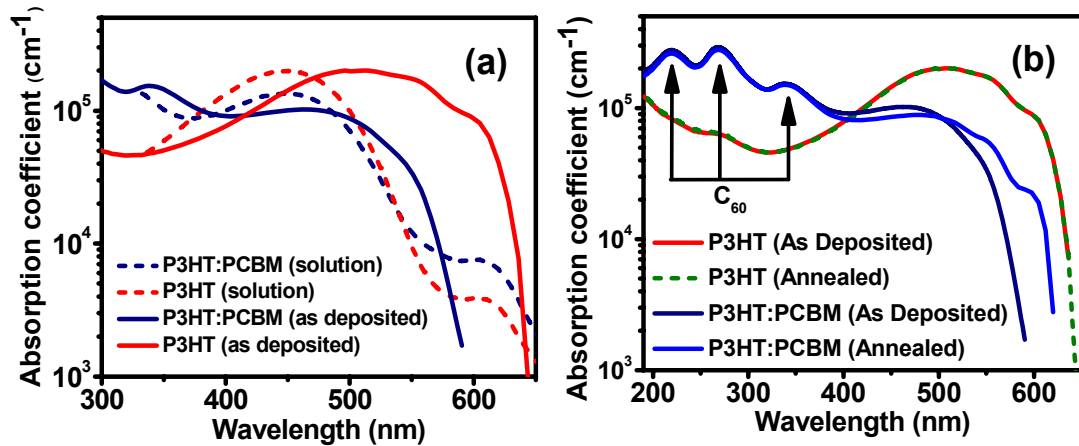


**Figure 3.8** (a) Comparison of absorption spectra of P3HT and P3HT:PCBM in solution and as deposited thin solidified films. (b) Comparison of absorption spectra of as deposited thin films and solvent vapor annealed thin films of P3HT and P3HT:PCBM.

To quantify the effects of solvent vapor annealing, we have utilized the absorption value at  $\alpha=10^4\text{ cm}^{-1}$ , referred to as the  $E_{04}$  gap,<sup>44</sup> for direct evaluation of the bandgap of the P3HT:PCBM composite. The  $E_{04}$  value is often used to define the bandgap in semiconductors because it is a thickness independent quantity representing

the maximum photon energy at which a micrometric film is transparent. Thus, based on the data presented in Figure 3.8(b), the  $E_{04}$  changes from  $\sim 2.17\text{eV}$  for the as-deposited P3HT:PCBM film to  $\sim 2.02\text{eV}$  after solvent vapor annealing, which is very close to the P3HT only value (as-deposited and annealed) of  $1.96\text{eV}$ . Since the optimal thickness of OPVs is generally less than  $200\text{nm}$ , the Tauc method<sup>44</sup> for determining the optical bandgap was also considered. As seen in Table 3.1, the optical bandgap utilizing the Tauc method is consistent with the  $E_{04}$  value. A detailed explanation of the Tauc method can be found in Appendix A.

**Table 3.1** Summary of optical bandgaps for P3HT:PCBM composite thin films before and after solvent vapor annealing using the Tauc method and the  $E_{04}$  values.

Method	P3HT:PCBM As Deposited	P3HT:PCBM Annealed	Change in Bandgap
Tauc Method			
Constant Momentum			
Direct Allowed	2.22eV	2.09eV	0.13eV
Indirect Allowed	2.04eV	1.85eV	0.19eV
Constant Dipole			
Direct Allowed	2.26eV	2.13eV	0.13eV
Indirect Allowed	2.07eV	1.87eV	0.20eV
$E_{04}$	2.17eV	2.02eV	0.15eV

Thus, the changes in the observed optical absorption edges, during solidification and solvent vapor annealing are mainly due to structural modifications in the P3HT, in agreement with observations of Chirvase et al.<sup>6</sup> Further support for the structural changes can also be seen in the development of the shoulder near  $600\text{nm}$  in P3HT:PCBM films which is absent in the as deposited P3HT:PCBM film. However, upon solvent vapor annealing, this shoulder becomes apparent in the film with an absorption coefficient of  $\sim 2 \times 10^4 \text{ cm}^{-1}$ . Higher absorption at this wavelength has been described as a vibronic feature generally explained by increased ordering of intra-chain

interactions and higher crystallization in P3HT.<sup>45, 46</sup> Such structural ordering, although prevented during the deposition of P3HT:PCBM films, is favored during solvent vapor annealing and provides beneficial effects on the photovoltaic device efficiencies.

### 3.4.3 Atomic Force Microscopy

The physical changes in the morphology of the P3HT:PCBM films before and after solvent vapor annealing observed by AFM are shown in Figure 3.9(a) and (b), respectively. In addition, the phase image of a solvent vapor annealed P3HT:PCBM nanocomposite showing fibril like features is shown in Figure 3.9(c). The as deposited thin films appear featureless while clusters of 10-20 nm are prominent on the surface of the solvent annealed films. The AFM image in Figure 3.9(b) is comparable to that of similar morphologies reported in the literature<sup>1, 12</sup> which also show dramatically improved efficiencies. It should be noted that no change in morphology upon solvent vapor annealing was observed by AFM in pure P3HT films which always appear smoother.

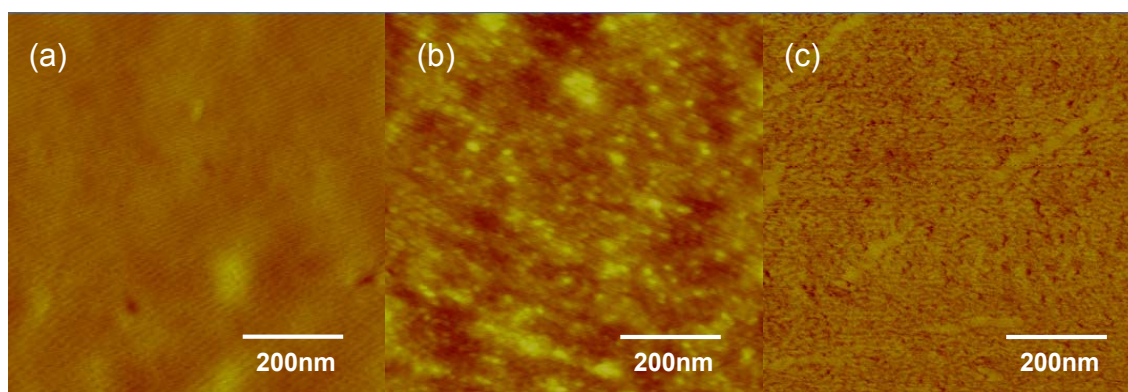


**Figure 3.9** (a) AFM height image of as deposited and (b) solvent vapor annealed P3HT:PCBM thin films. The z-range of images (a) and (b) are 6 nm and 11 nm respectively. (c) is a phase image of the P3HT:PCBM sample shown in (b).

This interpretation of the optical spectra and the AFM images is consistent with

a similar explanation for structural modifications of P3HT:PCBM during thermal annealing.<sup>7, 18</sup> In particular, Yang et al.<sup>18</sup> showed by means of transmission electron microscopy (TEM) that thermal annealing leads to de-mixing of P3HT and PCBM via formation of PCBM-rich regions, allowing the reorganization of the residual P3HT phase in stacked coplanar conjugated segments. The reorganization is prevented in the as deposited P3HT:PCBM films because of the rapid solidification and intercalation of PCBM. In solvent vapor annealed P3HT:PCBM however, ordering can occur via the diffusion of solvent vapor which softens the organic nanocomposite, allowing the migration of PCBM and the subsequent reorganization of P3HT. Indeed, solvent vapor annealing may be comparable to controlled evaporation of the solvent after deposition which has also been demonstrated to improve the solar cell efficiency, presumably by allowing ordering to occur.<sup>7</sup> We suspect that the observed changes in the optical absorption edge may also be due to stacking and subsequent  $\pi$ -conjugation of the P3HT segments.

#### **3.4.4 Photoluminescence**

The PL and Raman spectra of P3HT and P3HT:PCBM films before and after solvent vapor annealing are compared in Figure 3.10. The Raman and PL measurements are performed simultaneously in the Renishaw Raman system. The broad background observed in Figure 3.10 in the P3HT:PCBM sample prior to solvent vapor annealing is the contribution from the PL. The peaks superimposed on the PL background are the Raman peaks from the P3HT and the PET substrate. The Raman peaks will be discussed in the next section. Here we concentrate on the PL to obtain information

about exciton recombination and dissociation. It is clear from Figure 3.10 that the intensity of the PL is strongly suppressed for the P3HT:PCBM sample as a result of solvent vapor annealing. It can also be seen that the polaron-exciton binding energy ( $2U$ ) in the P3HT:PCBM samples is approximately 0.2 eV and does not vary significantly with annealing time and the presence of PCBM.

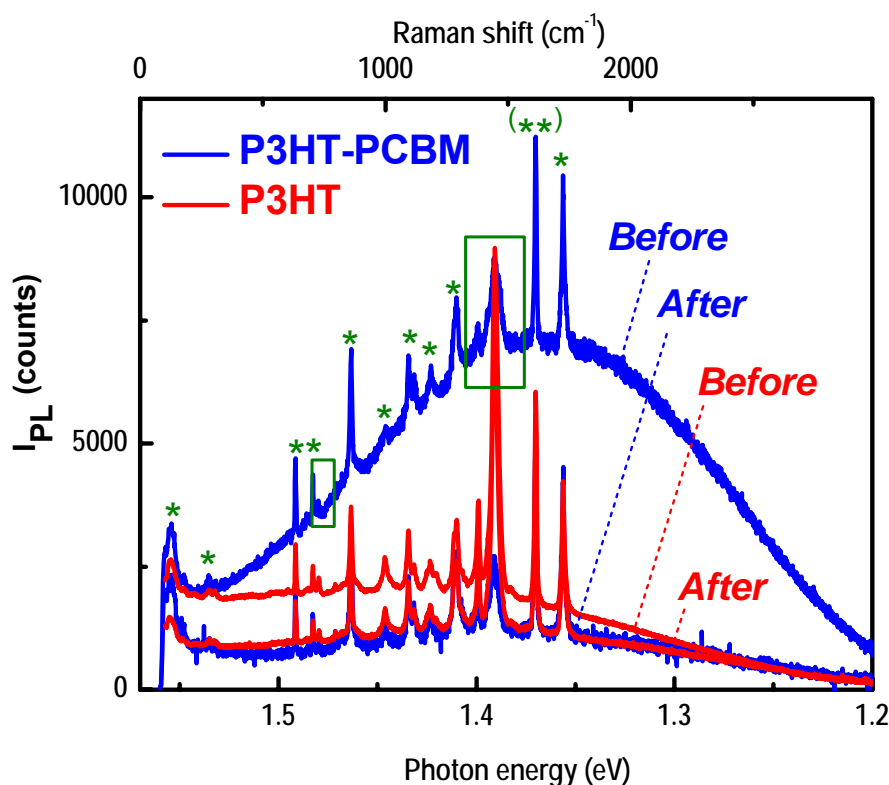


**Figure 3.10** Combined PL and Raman spectroscopy results of pure P3HT and P3HT:PCBM before and after solvent annealing. The peaks marked with asterisks (\*, \*\*) correspond to PET and ITO, respectively. The  $715\text{ cm}^{-1}$ ,  $1380\text{ cm}^{-1}$  and  $1440\text{ cm}^{-1}$  Raman peaks indicated by squares are assigned to the P3HT C-S-C ring deformation, C-C skeletal stretching and C=C ring stretching, respectively.<sup>24</sup>

However, a closer examination and careful fitting of the PL curves show that a small decrease in  $2U$  of approximately 0.015 eV occurs with solvent vapor annealing. The

method for determining this change is shown in Figure 3.11(a) utilizing PL from as-deposited P3HT:PCBM sample as an example. A Gaussian fit to the PL spectrum was utilized to extract the  $2U$  values. However, due to the presence of intense superimposed Raman peaks on top of the PL background, obtaining accurate fits was challenging. Therefore, prior to the fitting, the Raman peaks were subtracted from the PL curves. In Figure 3.11(a), these fits are shown. It was found that a Gaussian fit without the Raman peaks best represents the experimental data. Based on this, the PL data fits for before and after solvent vapor annealing are shown in Figure 3.11(b). It should be mentioned that the Gaussian fits were obtained using the Wire 2.0 Renishaw Raman analysis software. From Figure 3.11(b), a small difference in  $2U$  values before and after solvent vapor annealing can be observed. Although this value is very small, it does provide evidence for higher exciton delocalization, as we discuss below.

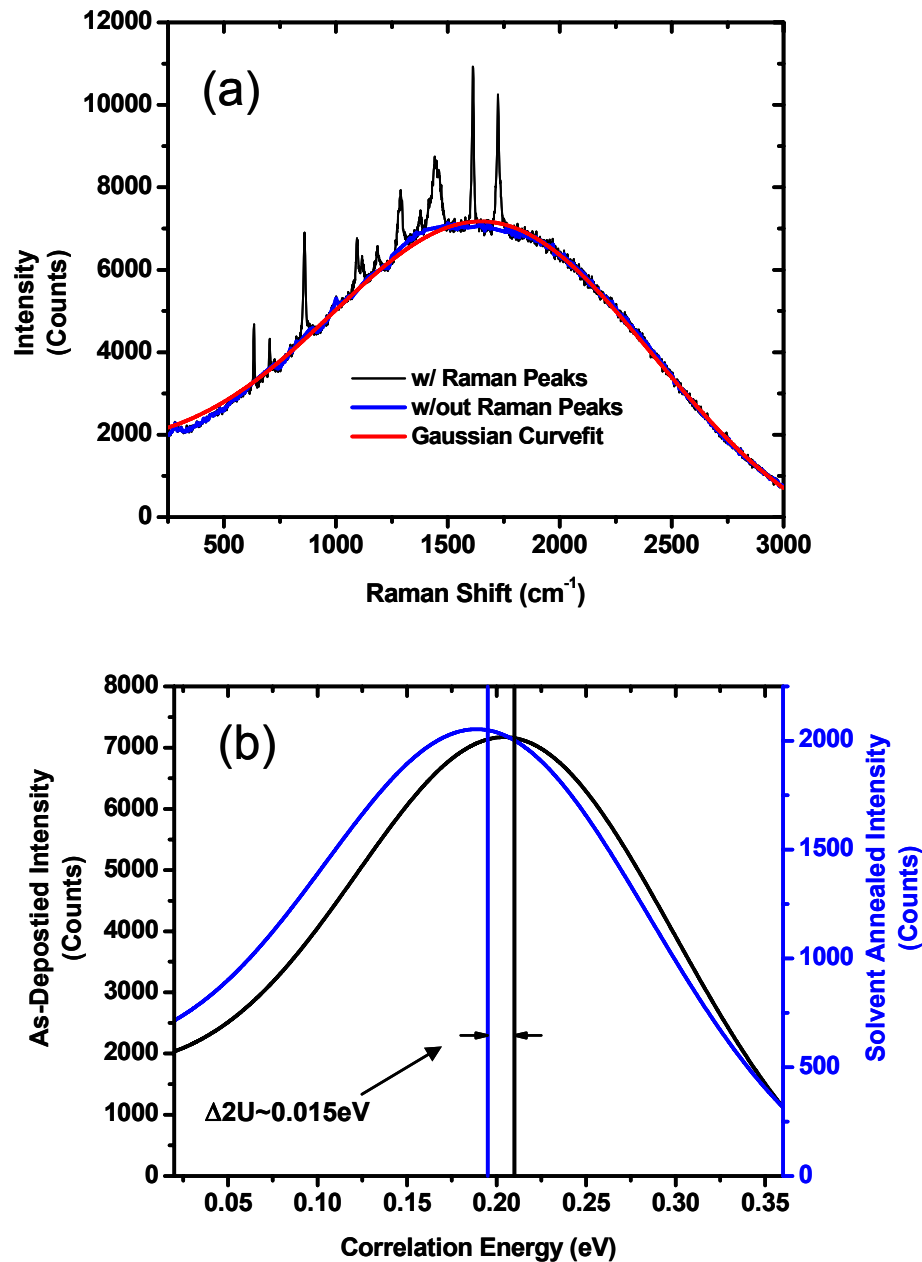


**Figure 3.11** (a) The sequence for determining the correlation energy ( $2U$ ) from the P3HT:PCBM PL peak is shown. The Raman peaks were manually removed from the broad PL spectrum and smoothing was performed. A Gaussian curve fit was obtained to identify the peak position. (b) The Gaussian fit of the PL peak for P3HT:PCBM before (black) and after (blue) solvent vapor annealing. The difference in the peak position is the change in  $2U$  or  $\sim 0.015 \text{ eV}$ .



In P3HT, the polaron-exciton confinement parameter ( $\gamma$ ) can be extracted from the energy in the absorption spectrum where  $\alpha=10^4 \text{ cm}^{-1}$  ( $E_{04}$ ) and the correlation energy using the formula:<sup>29, 47, 48</sup>

$$\gamma = (1-2U/E_{04}) \cdot \sin^{-1}(1-2U/E_{04}) \cdot [1 - (1-2U/E_{04})^2]^{-1/2} \quad \text{Eq. 3.1}$$

Substituting the energy where  $\alpha=10^4 \text{ cm}^{-1}$  ( $E_{04}$ ) from measurements in Figure 3.8(a) and Figure 3.8(b) (see also Table 3.1) and values for  $2U$  into Eq. 3.1,  $\gamma$  is found to remain relatively constant at  $\sim 2.4$ . Although the exciton delocalization is expected to increase with ordering, our result for the confinement parameter remaining relatively unchanged is not surprising. This can be attributed to the fact that the PL intensity in our solvent vapor annealed samples is very low, making it difficult to obtain precise values for  $2U$ . The low PL intensity is due to the fact that the excitation energy (1.57 eV) used here is well below the band gap of the P3HT so that the absorption is mediated by low density mid-gap states. Analysis using higher energy excitation (e.g. 2.41 eV Argon laser) closer to the band gap of P3HT would likely yield an increase in  $\gamma$ . The decrease in the values of  $2U$  and increase in  $\gamma$  are generally correlated to increased delocalization with ordering similar to what we observe with solvent vapor annealing.<sup>29, 48, 49</sup> While the confinement parameter values obtained here are higher than those found in the literature, it has been shown that increased degrees of regioregularity of P3HT (from 50% to 80% regioregularity) leads to an increase in values of  $\gamma$ .<sup>29</sup> As the material used in this work is up to 98.5% regioregular, we believe these values to be reasonable.

The evolution of the PL peak intensity as a function of the solvent vapor annealing time is plotted in Figure 3.12. Unlike the degree of confinement which was not significantly affected by the presence of PCBM or by solvent vapor annealing, the

PL intensity is strongly quenched by solvent vapor annealing in P3HT:PCBM films. Furthermore, the decrease in PL in the P3HT:PCBM films mostly occurs in the first minute of solvent vapor annealing, correlating to the improvement in the device efficiency. Although the PL intensity also decreases in P3HT films, the effect is less dramatic than in the P3HT:PCBM material.

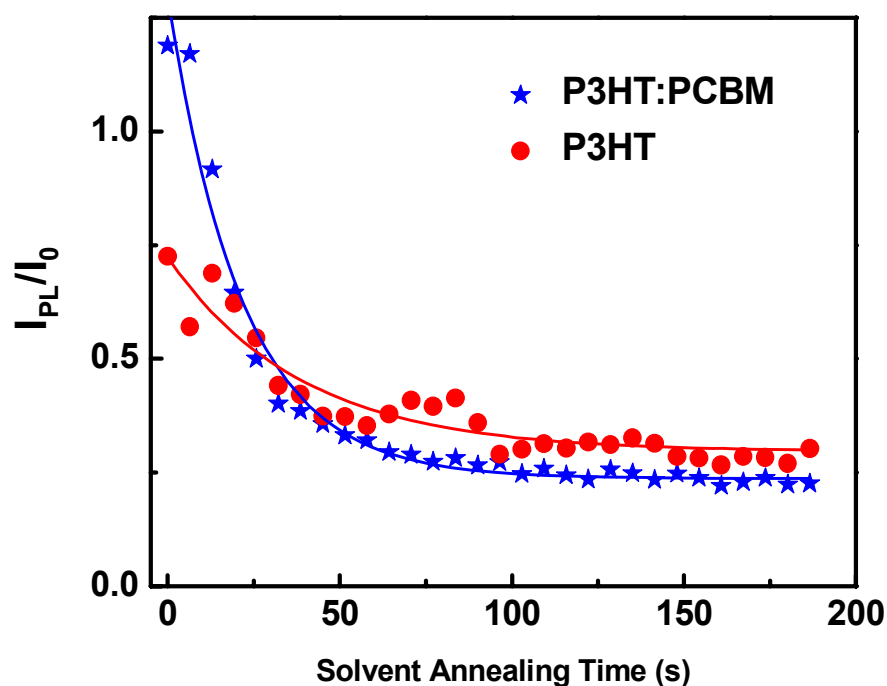


**Figure 3.12** Summary of the PL intensity versus the annealing time for pure P3HT and P3HT:PCBM.

### 3.4.5 Raman Spectroscopy

Returning to Figure 3.10, a number of Raman peaks superimposed on the broad PL spectra can be observed. Raman spectra recorded from bare substrates allow us to assign the peaks marked with stars (\*, \*\*) to PET and ITO, respectively. The  $715\text{ cm}^{-1}$ ,

1380  $\text{cm}^{-1}$  and 1440  $\text{cm}^{-1}$  Raman peaks indicated by squares are assigned to the P3HT C-S-C ring deformation, C-C skeletal stretching and C=C ring stretching, respectively.<sup>24</sup> No Raman features attributable to PCBM, such as the  $A_{1g}$  1469  $\text{cm}^{-1}$  mode of fullerenes could be resolved. In order to extract additional information from the Raman spectra, we compare the 1350-1500  $\text{cm}^{-1}$  region of P3HT and P3HT:PCBM devices before and after solvent vapor annealing in Figure 3.13(a). It can be seen from Figure 3.13(a) that while the Raman shift of the C=C peak is almost constant, interesting effects on the full width at half maximum (FWHM) of the peak can be observed. In pure P3HT, the FWHM decreases insignificantly (from 24  $\text{cm}^{-1}$  to 20  $\text{cm}^{-1}$ ) with solvent vapor annealing, as shown in Figure 3.13(b). This minor change in the FWHM is consistent with the negligible changes observed in the optical absorption spectra, sample morphology and the minor decrease in PL intensity. In contrast, in P3HT:PCBM films, the C=C signal before solvent vapor annealing is much broader (about 32  $\text{cm}^{-1}$ ) which narrows to 22  $\text{cm}^{-1}$  after solvent vapor annealing, close to the 20  $\text{cm}^{-1}$  FWHM of pure P3HT films. Once again, the relatively more dramatic decrease in the FWHM occurs within the first minute of solvent vapor annealing time. Furthermore, since the Gaussian widths of the Raman lines in heterogeneous systems are a measure of their disorder,<sup>50</sup> we can infer that solvent vapor annealing strongly reduces the disorder in P3HT:PCBM, consistent with stacking of conjugated P3HT segments.

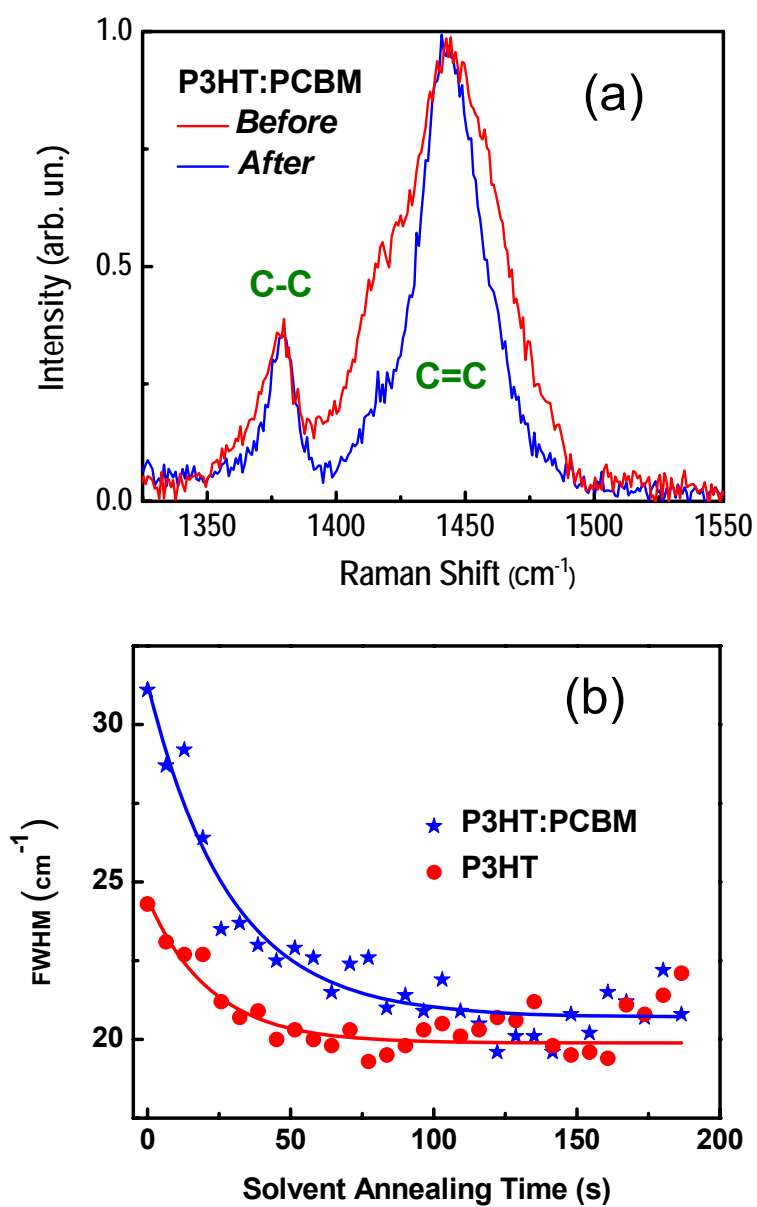


**Figure 3.13** (a) The 1350-1500  $\text{cm}^{-1}$  Raman region of P3HT and P3HT:PCBM devices before and after solvent vapor annealing. (b) Summary of the FWHM of the 1440  $\text{cm}^{-1}$  Raman C=C peak versus the annealing time for pure P3HT and P3HT:PCBM.

### 3.5 Discussion

Based on the data presented in this chapter, it is plausible that solvent vapor annealing of P3HT:PCBM leads to substantial ordering in the polymer so that the optoelectronic, morphological, PL and Raman characteristics are comparable to highly ordered P3HT. This is due to the strong reduction in disorder via segregation of PCBM into PCBM-rich regions and stacking of P3HT chains. These structural changes have a beneficial effect on the solar cell performance (see Figure 3.7) which can be explained by the enhanced transport of the carriers through ordering of the P3HT:PCBM matrix.<sup>18</sup> The manifestation of the enhanced transport due to ordering of the P3HT layer can be seen as higher dark current in Figure 3.7(a) (note that the high current region at positive voltages is primarily dominated by the dark current even under illumination). In addition to better transport, the modification of the morphology of the interface between PCBM and P3HT due to solvent vapor annealing will also play an important role in charge dissociation, as demonstrated by Bässler and co-workers<sup>51</sup> and Koehler and co-workers for thermal annealing.<sup>52</sup>

The improvement in the solar cell device efficiency may also arise from an additional mechanism occurring during solvent vapor annealing. Based on our measurements, we have developed the energy diagram shown in Figure 3.14 for the photovoltaic devices. In the as deposited P3HT:PCBM films (dotted line in the P3HT energy levels in Figure 3.14), the presence of PCBM prevents the stacking of P3HT so that the optical gap and excitonic levels are similar to those of P3HT in solution. Specifically, assuming a mid-gap energy of 4.3 eV for P3HT, the lowest unoccupied molecular orbital (LUMO) equilibrium level for unannealed P3HT is at  $E_1 [S_1, (eq)] \sim$

3.3 eV compared to the acceptor level of PCBM at  $\sim 3.75$  eV.<sup>38, 53</sup> The decrease in the optical gap (from absorption spectroscopy) indicates that the LUMO of P3HT after solvent vapor annealing is closer to the acceptor state of the PCBM, as shown in Figure 3.14. Thus, there will be a shift in the probability of the radiative recombination of the electron-hole pair (which creates the PL observed in Figure 3.10 to the charge transfer from the LUMO of the P3HT to the LUMO of the PCBM making the transition indicated by the dark arrows in Figure 3.14 more likely. While the changes in the correlation energy ( $U$ ) and polaron-exciton confinement parameter ( $\gamma$ ) after solvent vapor annealing are not substantial, they do suggest improvement in exciton delocalization. Furthermore, additional improvement in solar cell efficiency would be provided by increased absorption between 570 nm and 615 nm.

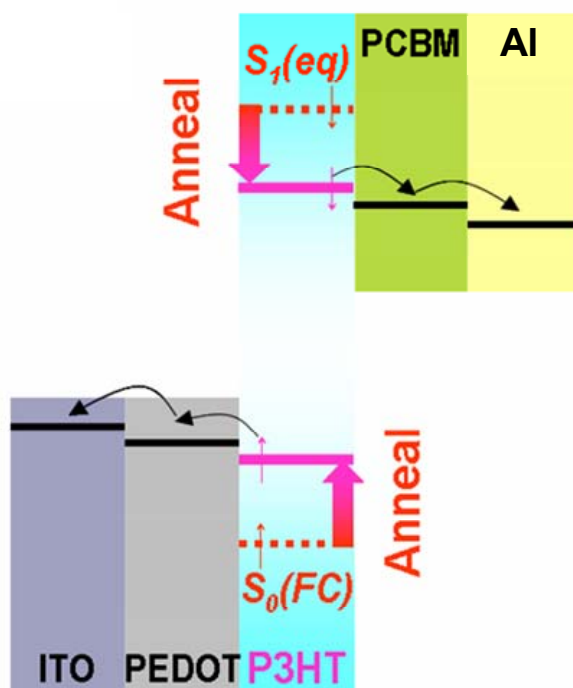


**Figure 3.14** Energy level diagram based on our measurements before and after solvent vapor annealing. The P3HT LUMO level shifts downward as indicated by the red arrows, increasing the possibility of electron transfer into PCBM and hole transfer into ITO, as indicated by the black arrows.

### 3.6 Conclusions

In conclusion, it has been demonstrated that solvent vapor annealing of P3HT:PCBM at room temperature leads to a marked increase in the ordering of P3HT, presumably due to demixing of PCBM, as also observed by transmission electron microscope (TEM).<sup>13</sup> The more ordered structure provides better transport for holes through the more crystalline P3HT and electrons via hopping through the PCBM, comparable to what occurs during thermal annealing. The dissociation of excitons and ordering of the P3HT have been observed using *in-situ* photoluminescence and Raman spectroscopies. We discovered that the morphological changes which correlate to the improvement in the efficiencies of our solar cells occur within minutes of solvent vapor annealing. Exposure to the solvent vapor for longer periods does not change the structure or the device performance. Therefore, solvent vapor annealing might be an alternative to thermal annealing for improving the P3HT:PCBM photovoltaic performance, especially for temperature sensitive substrates.

### 3.7 References

- <sup>1</sup> S.-S. Sun and N. S. Sariciftci, *Organic photovoltaics; mechanisms, materials, and devices* (Taylor & Francis, London, 2005).
- <sup>2</sup> C. J. Brabec, V. Dyakonov, J. Parisi, et al., *Organic Photovoltaics: Concepts and Realization* (Springer-Verlag, Heidelberg, 2003).
- <sup>3</sup> C. J. Brabec, N. S. Sariciftci, and J. C. Hummelen, *Advanced Functional Materials* **11**, 15 (2001).
- <sup>4</sup> N. Camaioni, G. Ridolfi, G. Casalbore-Miceli, et al., *Advanced Materials* **14**, 1735 (2002).
- <sup>5</sup> D. Chirvase, Z. Chiguvare, M. Knipper, et al., *Journal of Applied Physics* **93**, 3376 (2003).
- <sup>6</sup> D. Chirvase, J. Parisi, J. C. Hummelen, et al., *Nanotechnology* **15**, 1317 (2004).
- <sup>7</sup> G. Li, V. Shrotriya, J. S. Huang, et al., *Nature Materials* **4**, 864 (2005).
- <sup>8</sup> F. Padinger, R. S. Rittberger, and N. S. Sariciftci, *Advanced Functional Materials* **13**, 85 (2003).
- <sup>9</sup> M. Reyes-Reyes, K. Kim, and D. L. Carroll, *Applied Physics Letters* **87** (2005).
- <sup>10</sup> I. Riedel and V. Dyakonov, *physica status solidi (a)* **201**, 1332 (2004).
- <sup>11</sup> N. S. Sariciftci, L. Smilowitz, A. J. Heeger, et al., *Science* **258**, 1474 (1992).
- <sup>12</sup> S. E. Shaheen, C. J. Brabec, N. S. Sariciftci, et al., *Applied Physics Letters* **78**, 841 (2001).
- <sup>13</sup> H. Sirringhaus, N. Tessler, and R. H. Friend, *Science* **280**, 1741 (1998).
- <sup>14</sup> G. Yu, J. Gao, J. C. Hummelen, et al., *Science* **270**, 1789 (1995).
- <sup>15</sup> L. J. A. Koster, V. D. Mihailetschi, and P. W. M. Blom, *Applied Physics Letters* **88**, 093511 (2006).
- <sup>16</sup> Y. Kim, S. A. Choulis, J. Nelson, et al., *Journal Of Materials Science* **40**, 1371 (2005).
- <sup>17</sup> Y. Kim, S. A. Choulis, J. Nelson, et al., *Applied Physics Letters* **86**, N.PAG (2005).
- <sup>18</sup> X. N. Yang, J. Loos, S. C. Veenstra, et al., *Nano Letters* **5**, 579 (2005).
- <sup>19</sup> K. C. Dickey, J. E. Anthony, and Y. Loo, *Advanced Materials* **18**, 1721 (2006).



- 20 Y. Zhao, Z. Xie, Y. Qu, et al., *Applied Physics Letters* **90**, 043504 (2007).
- 21 M. Berggren, G. Gustafsson, O. Inganäs, et al., *Applied Physics Letters* **65**, 1489 (1994).
- 22 D. J. Gardiner and P. R. Graves, *Practical Raman Spectroscopy* (Springer-Verlag, Berlin, 1989).
- 23 E. Smith and G. Dent, *Modern Raman Spectroscopy - A Practical Approach* (John Wiley & Sons, Chichester, 2005).
- 24 M. Baibarac, M. Lapkowski, A. Pron, et al., *Journal of Raman Spectroscopy* **29**, 825 (1998).
- 25 J. G. Grasselli and B. J. Bulkin, *Analytical Raman Spectroscopy* (Wiley, New York, 1991).
- 26 E. Klimov, W. Li, X. Yang, et al., *Macromolecules* **39**, 4493 (2006).
- 27 U. Schmidt, A. Jauss, W. Ibach, et al., *Microscopy Today* **13**, 30 (2005).
- 28 L. S. Swanson, J. Shinar, and K. Yoshino, *Physical Review Letters* **65**, 1140 (1990).
- 29 B. Xu and S. Holdcroft, *Macromolecules* **26**, 4457 (1993).
- 30 T.-A. Chen, X. Wu, and R. D. Rieke, *Journal of the American Chemical Society* **117**, 233 (1995).
- 31 Y. H. Kim, D. Spiegel, S. Hotta, et al., *Physical Review B* **38**, 5490 (1988).
- 32 S. D. D. V. Rughooputh, S. Hotta, A. J. Heeger, et al., *Journal of Polymer Science Part B: Polymer Physics* **25**, 1071 (1987).
- 33 J. M. Tour and R. Wu, *Macromolecules* **25**, 1901 (1992).
- 34 V. Shrotriya, J. Ouyang, R. J. Tseng, et al., *Chemical Physics Letters* **411**, 138 (2005).
- 35 F. J. Giessibl, *Reviews of Modern Physics* **75**, 949 (2003).
- 36 S. Morita, R. Wiesendanger, and E. Meyer, *Noncontact Atomic Force Microscopy* (Springer, Berlin; New York 2002).
- 37 D. I. V. M. Group, *MultiMode™ SPM Instruction Manual* (Digital Instruments Veeco Metrology Group, Santa Barbara, 1999).
- 38 D. Chirvase, Z. Chiguvare, M. Knipper, et al., *Synthetic Metals* **138**, 299 (2003).

- 39 R. A. Street, Physical Review B **18**, 1880 (1978).
- 40 R. A. Street, Physical Review B **21**, 5775 (1980).
- 41 R. A. Street, Physical Review B **23**, 861 (1981).
- 42 B. C. Hess, G. S. Kanner, and Z. Vardeny, Physical Review B **47**, 1407 (1993).
- 43 A. Du Pasquier, S. Miller, and M. Chhowalla, Solar Energy Materials and Solar Cells **90**, 1828 (2006).
- 44 J. Tauc, *Amorphous and Liquid Semiconductors* (Plenum Press, London, New York, 1974).
- 45 P. J. Brown, D. S. Thomas, A. Kohler, et al., Physical Review B **67**, 064203 (2003).
- 46 X. M. Jiang, R. Österbacka, O. Korovyanko, et al., Advanced Functional Materials **12**, 587 (2002).
- 47 A. O. Patil, A. J. Heeger, and F. Wudl, Chem. Rev. **88**, 183 (1988).
- 48 J. Ruhe, N. F. Colaneri, D. D. C. Bradley, et al., Journal of Physics: Condensed Matter **2**, 5465 (1990).
- 49 T. W. Hagler, K. Pakbaz, K. F. Voss, et al., Physical Review B **44**, 8652 (1991).
- 50 M. V. Klein, in *Light Scattering in Solids*, edited by M. Cardona (Springer-Verlag, Berlin, 1975), Vol. 8.
- 51 V. I. Arkhipov, P. Heremans, and H. Bassler, Applied Physics Letters **82**, 4605 (2003).
- 52 M. Koehler, M. C. Santos, and M. G. E. d. Luz, Journal of Applied Physics **99**, 053702 (2006).
- 53 R. Valaski, L. M. Moreira, L. Micaroni, et al., Journal of Applied Physics **92**, 2035 (2002).

## Chapter 4

### Single Walled Carbon Nanotube Thin Films as Transparent and Conducting Electrodes in Organic Photovoltaic Devices

#### 4.1 Introduction

The use of indium tin oxide (ITO) in organic photovoltaics (OPVs) has been well established. Although ITO it has excellent transmissive and conductive properties, the use of physical vapor deposition (PVD) in its manufacture makes it expensive. In addition, since it utilizes rare elements such as indium, which has increased in price from \$97/kilogram in 2002 to \$855/kilogram in 2006 (an increase of almost 900%), ITO has become expensive. The increase in the price of indium along with an increase in demand for flat panel liquid crystal displays (LCDs)<sup>1</sup> has driven the cost of ITO higher at a faster than expected rate. As the market for LCDs, as well as other optoelectronic devices, including photovoltaics, continues to grow, it can be expected that supplies of indium will be depleted and prices will remain high. Since the aforementioned 10% simulated efficiency for organic photovoltaics falls short of the typical 14-16%<sup>2</sup> efficiency generated by commercially available silicon solar cells, cost becomes an even more significant factor. Thus, for the use of organic solar cells to become more widespread, an alternative to ITO must be identified.

Recently, single walled carbon nanotube (SWNT) thin films deposited from solution have been shown to have interesting optoelectronic properties.<sup>3-16</sup> Specifically, the electrical conductivity and transparency of the thin films have been shown to vary as a function of the density of SWNTs. Therefore, conducting and transparent thin films of SWNTs can be deposited. The lowest reported sheet resistance for a SWNT thin film is

$30 \text{ } \Omega/\square^{14}$  with a transparency of approximately 80% (typical ITO values are 10-30  $\Omega/\square$  at 85% transparency). Typically, however, values of 150-200  $\Omega/\square$  at a transparency approaching 80% are obtained. These values suggest that SWNT thin films may be suitable for ITO replacement in OPVs.

## 4.2 Single Walled Carbon Nanotubes

A major contribution of this thesis is the demonstration of SWNT thin films as the transparent and conducting electrode in organic photovoltaic devices. The unique optoelectronic properties of SWNT thin films make them useful for many applications. In order to understand why networks of SWNTs can be highly conducting but still remain transparent, it is important to discuss the structure and electronic properties of individual nanotubes in more detail.

A carbon nanotube is derived from graphite, the most common allotrope of carbon. Graphite is a  $sp^2$  bonded 2-dimensional layered solid with planes consisting of carbon atoms arranged in a hexagonal structure, as shown in Figure 4.1(a). The planes are weakly connected by  $\pi$  bonds which make graphite a semi-metal. Diamond is the other most common allotrope of carbon, but it is different from graphite in that it is  $sp^3$  hybridized, making it the hardest material and also a wide band gap semiconductor. The structure of diamond is shown in Figure 4.1(b) for comparison. The fullerene molecule, a nanostructured allotrope of carbon, was discussed in Chapter 1. Here, the unique properties that arise when one sheet of graphite (graphene) is rolled up to form a single walled carbon nanotube shown in Figure 4.1(c) will be discussed.

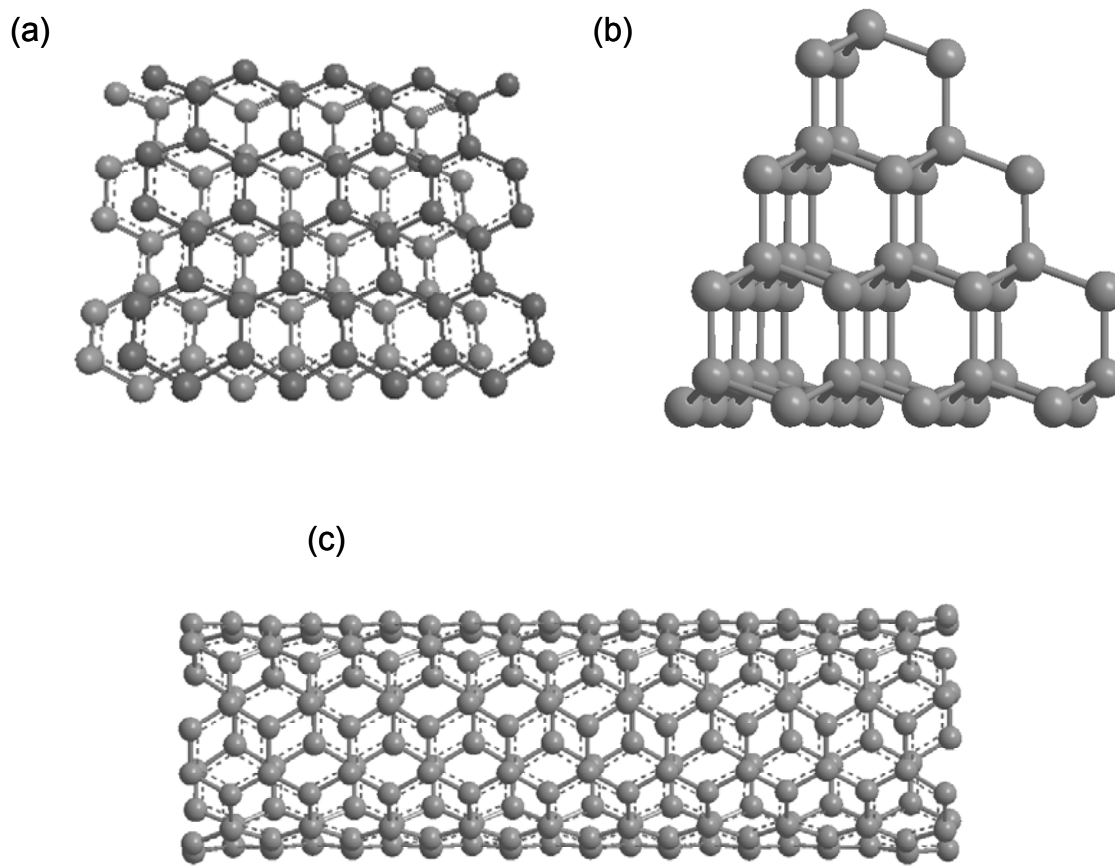


**Figure 4.1** Three allotropes of carbon: (a) graphite, (b) diamond and (c) single walled carbon nanotube.

Multi-walled carbon nanotubes were first reported by Sumio Iijima at NEC in 1991.<sup>17</sup> In 1993, Iijima<sup>18</sup> and Bethune<sup>19</sup> at IBM reported the fabrication of SWNTs by catalytic arc discharge. Individually, SWNTs exist as either metallic (conducting) or semi-conducting, depending on the chirality or “twist” of the hexagonal lattice as it is rolled into its cylindrical form. SWNTs can be found in three general configurations as shown in Figure 4.2: armchair, zig-zag and chiral.<sup>20, 21</sup>

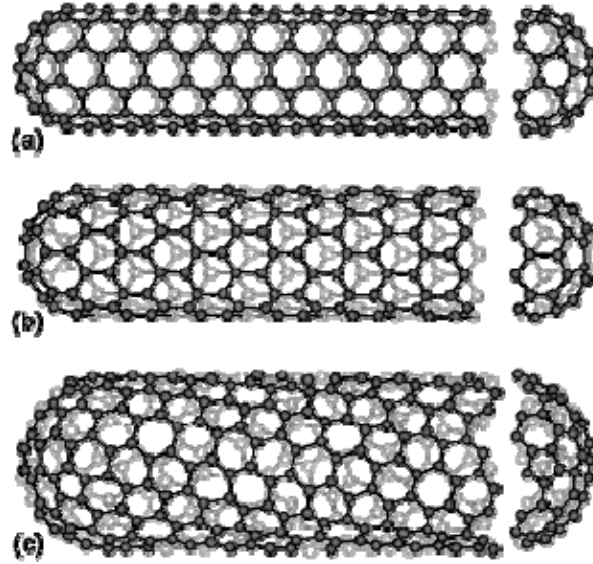


**Figure 4.2** Schematics of single wall carbon nanotubes: (a) armchair, (b) zig-zag and (c) chiral.<sup>20, 21</sup>

The different types of nanotubes can be described by the chiral vector  $(n, m)$ , where  $n$  and  $m$  are integers of the vector equation  $\mathbf{C} = n\mathbf{a}_1 + m\mathbf{a}_2$ .  $\mathbf{a}_1$  and  $\mathbf{a}_2$  are the unit vectors of the hexagonal lattice as described by the diagram in Figure 4.3.<sup>20, 21</sup> By “unwrapping” the nanotube along its axis, two lines can be drawn which define the tube axis on the graphene sheet. A vector can then be drawn,  $(11,7)$  in the diagram, which is the sum of two zigzag vectors,  $(11,0)$  and  $(0,7)$ , which connects two carbon atoms which lie on each of the axis lines. SWNTs are referred to as ‘chiral’ if their wrapping angle  $\phi$  lies between  $0^\circ < \phi < 30^\circ$ .<sup>20</sup> If the chiral vector lies along the armchair line ( $\phi=0$ ), then it is called an “armchair” nanotube. If the chiral vector lies along the zigzag line, then it is a “zigzag” SWNT.<sup>22</sup> The armchair and zigzag vector direction are indicated by the dotted lines in Figure 4.3.



of zigzag and chiral tubes are metallic. As the circumference of the nanotube is the length of the chiral vector, the diameter of the tube is the length of the chiral vector divided by  $\pi$ . Given the chiral vector  $(n,m)$ , the diameter of the tube can be calculated using the relationship

$$\begin{aligned} d &= \sqrt{3}a_{c-c}(n^2 + nm + m^2)^{1/2}/\pi \\ &= 0.0783(n^2 + nm + m^2)^{1/2} \end{aligned} \quad \text{Eq. 4.2}$$

where  $a_{c-c}$  is the carbon atom nearest-neighbor distance.<sup>20</sup> The chiral angle,  $\phi$ , is given by

$$\phi = \tan^{-1}[\sqrt{3}/(m+2n)] \quad \text{Eq. 4.3}$$

Since a single walled carbon nanotube has the structure of a single graphene sheet rolled into a cylinder, the band structure and electronic properties of SWNTs can be extrapolated from the structure and properties of graphene. The real space unit cell and reciprocal lattice for a graphene sheet is shown in Figure 4.4. The unit cell contains two carbon atoms, at positions A and B in the figure, and all other lattice points can be mapped using the lattice unit vectors  $\mathbf{a}_1$  and  $\mathbf{a}_2$ . The simplest form of the 2D energy dispersion relation for the  $\pi$ -electrons, in a tight binding approximation, is given by<sup>20</sup>:

$$E_{g2D}(k_x, k_y) = \pm \gamma_0 \left\{ 1 + 4 \cos\left(\frac{\sqrt{3}k_x a_0}{2}\right) \cos\left(\frac{k_y a_0}{2}\right) + 4 \cos^2\left(\frac{k_y a_0}{2}\right) \right\}^{1/2} \quad \text{Eq. 4.4}$$

Where  $\gamma_0$  is the C-C nearest-neighbor energy overlap integral,  $(k_x, k_y)$  are the wave vectors and  $a_0$  is the lattice constant with a value of  $1.42 \times \sqrt{3} \text{ \AA}$ .<sup>20</sup> The negative (below the Fermi level) and positive (above the Fermi level) values are for the bonding and anti-bonding bands respectively.



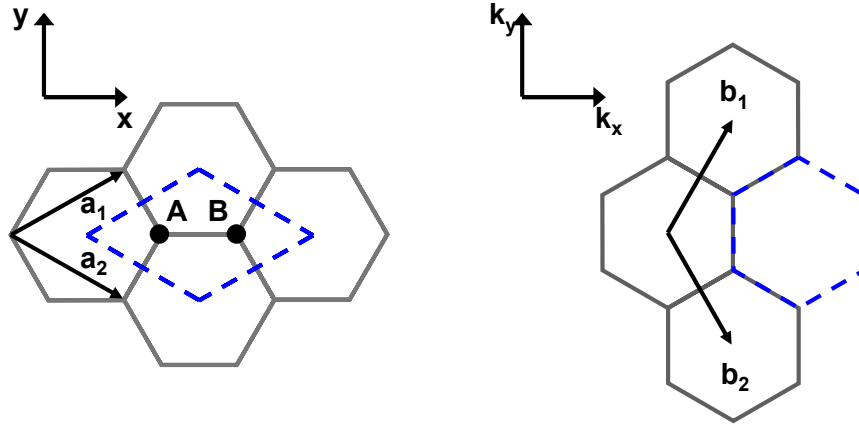


**Figure 4.4** Schematic of the structure of graphene unit cell (the areas within dashed borders) in real space (left) and reciprocal space (right).<sup>24</sup>

A graphene sheet is a zero band gap semiconductor<sup>25</sup> because at temperature = 0, it has a full valence band and an empty conduction band; however, the top of the valence band and the bottom of the conduction band have equivalent energies as can be seen in Figure 4.5 where the energy gap vanishes at the six corners of the first Brillouin zone. These points, where the valence and conduction bands meet, are referred to as **K**-points. Typically, crystalline conductors have complex Fermi surfaces where the valence and conduction bands overlap. In insulators and semi-conductors where the Fermi energy lies in the bandgap, no Fermi surface exists. In the case of the graphene, the Fermi surface consists of the six **K**-points where the density of states at the Fermi level is zero.

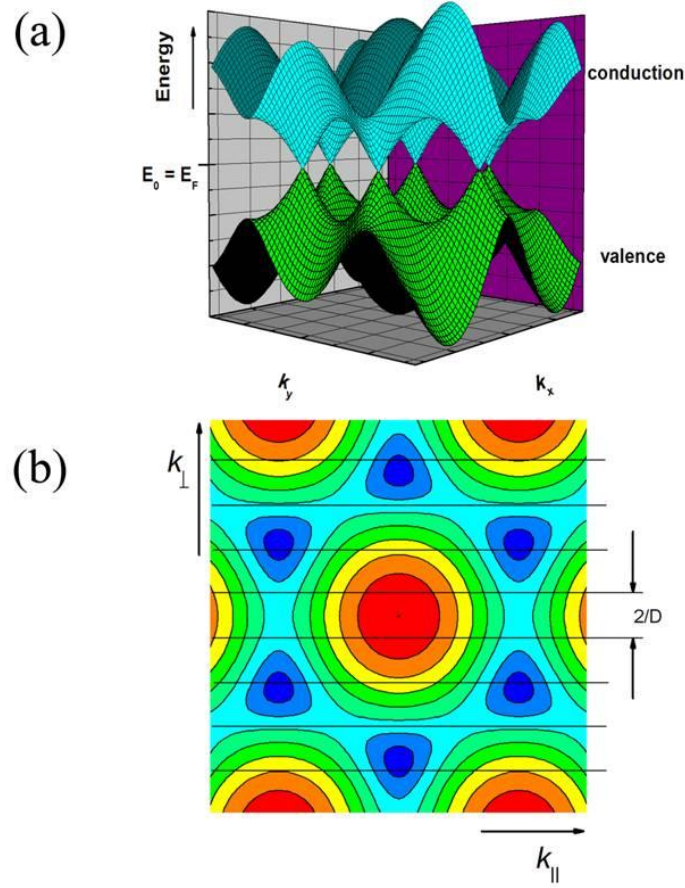


**Figure 4.5** (a) 3D energy diagram of graphene. The valence and conduction bands touch at the six points at the Fermi level called **K**-points. (b) Contour plot of the graphene valence states for a SWNT with zero chiral angle. Parallel lines are spaced  $2/D$  indicate  $k$  vectors allowed by the cylindrical boundary condition. Each line is a 1D subband. Lower energies are marked with red and higher energies are marked with blue.<sup>26</sup>

Using the electronic band structure of graphene, the electronic structure of SWNTs can be derived.<sup>27</sup> Since the structure of SWNTs is rolled up sheets of graphene, the energy modes in the circumferential direction are quantized and must satisfy the condition:

$$k_{\perp}C = 2\pi q \quad \text{Eq. 4.5}$$

where  $k_{\perp}$  is the wavenumber in the direction perpendicular to the axis of the SWNT,  $C$  is the chiral vector and  $q$  is an integer. In the direction parallel to the axis of the SWNT

( $k_{||}$ ) the electrons move freely with a continuous energy distribution. Thus, when drawn in the reciprocal space of graphene, the quantization results in a discrete number of parallel lines which represent the allowed modes or subbands. For armchair SWNTs the number of allowed wavenumbers in the circumferential direction is defined by:<sup>20</sup>

$$n\sqrt{3}k_x a_0 = 2\pi q \quad \text{Eq. 4.6}$$

Thus, the bands run in the  $k_y$  direction. Substitution of Eq. 4.6 into Eq. 4.4 results in the energy dispersion relation for the armchair SWNT:

$$E_{armchair}(k_y) = \pm \gamma_0 \left\{ 1 + 4 \cos\left(\frac{q\pi}{n}\right) \cos\left(\frac{k_y a_0}{2}\right) + 4 \cos^2\left(\frac{k_y a_0}{2}\right) \right\}^{1/2} \quad \text{Eq. 4.7}$$

For zigzag SWNTs the number of allowed wavenumbers in the circumferential direction is defined by:<sup>20</sup>

$$nk_y a_0 = 2\pi q \quad \text{Eq. 4.8}$$

Thus, the bands run in the  $k_x$  direction. Substitution of Eq. 4.8 into Eq. 4.4 results in the energy dispersion relation for the zigzag SWNT

$$E_{zigzag}(k_x) = \pm \gamma_0 \left\{ 1 + 4 \cos\left(\frac{\sqrt{3}k_x a_0}{2}\right) \cos\left(\frac{q\pi}{n}\right) + 4 \cos^2\left(\frac{q\pi}{n}\right) \right\}^{1/2} \quad \text{Eq. 4.9}$$

The spacing of the bands ( $\Delta k$ ) is determined by the diameter of the SWNT through the relationship  $\Delta k = \frac{2\pi}{|C|} = \frac{2}{d}$ . Examples for armchair, zigzag and chiral SWNTs are shown in Figure 4.6. If the bands intersect the **K**-points of the Brillouin zone of graphene then the SWNT will be metallic. Hence, it can be seen in Figure 4.6(a) that the bands of armchair SWNTs will always intersect **K**-points and always be metallic. In the case where the bands do not intersect the **K**-points the SWNT will behave as a

semiconductor. As the bandgap is determined by the distance the subband passes the  $\mathbf{K}$ -point, the bandgap will be inversely proportional to the diameter. Thus, as seen Figure 4.6(b) and (c), the electronic properties for zigzag and chiral SWNTs will depend on the chirality and diameter of each SWNT.

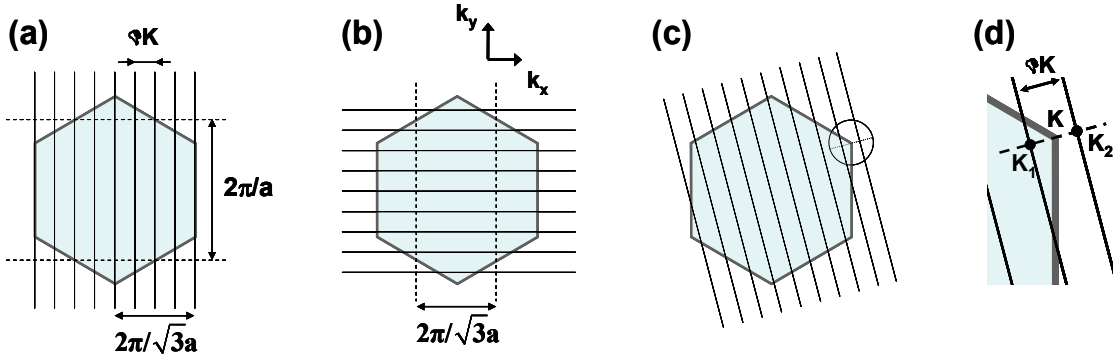


**Figure 4.6** Schematic of reciprocal space for (a) armchair, (b) zigzag and (c) chiral SWNTs. For (a) armchair SWNTs the  $\mathbf{K}$ -lines are parallel in the  $k_y$  direction, always intersect the  $\mathbf{K}$ -points and are thus always metallic. For (b) zigzag SWNTs the  $\mathbf{K}$ -lines are parallel in the  $k_x$  direction, only intersect the  $\mathbf{K}$ -points when the condition in Eq. 4.1 ( $n-m=3q$ ) is met and are metallic when this is the case. The  $\mathbf{K}$ -lines for (c) chiral SWNTs have many orientations, will also intersect the  $\mathbf{K}$ -points when the condition in Eq. 4.1 is met and are metallic in this case. The circular inset in (c) is enlarged in figure (d). It shows the relationship of allowed  $\mathbf{K}$ -lines to Fermi level. The points of closest approach to  $\mathbf{K}$  are  $\mathbf{K}_1$  and  $\mathbf{K}_2$ .<sup>24</sup>

Figure 4.7 shows the density of states for two zigzag SWNTs: (a) a semiconducting (10,0) SWNT and (b) a metallic (9,0) SWNT. The van Hove singularities characteristic of 1D energy bands can be seen at the edge of each energy band. Figure 4.7(a) shows the absence of occupied states at the Fermi level resulting in an energy gap in a semiconducting SWNT, while Figure 4.7(b) shows the finite density of states at the Fermi energy, resulting in a metallic tube.<sup>23</sup>

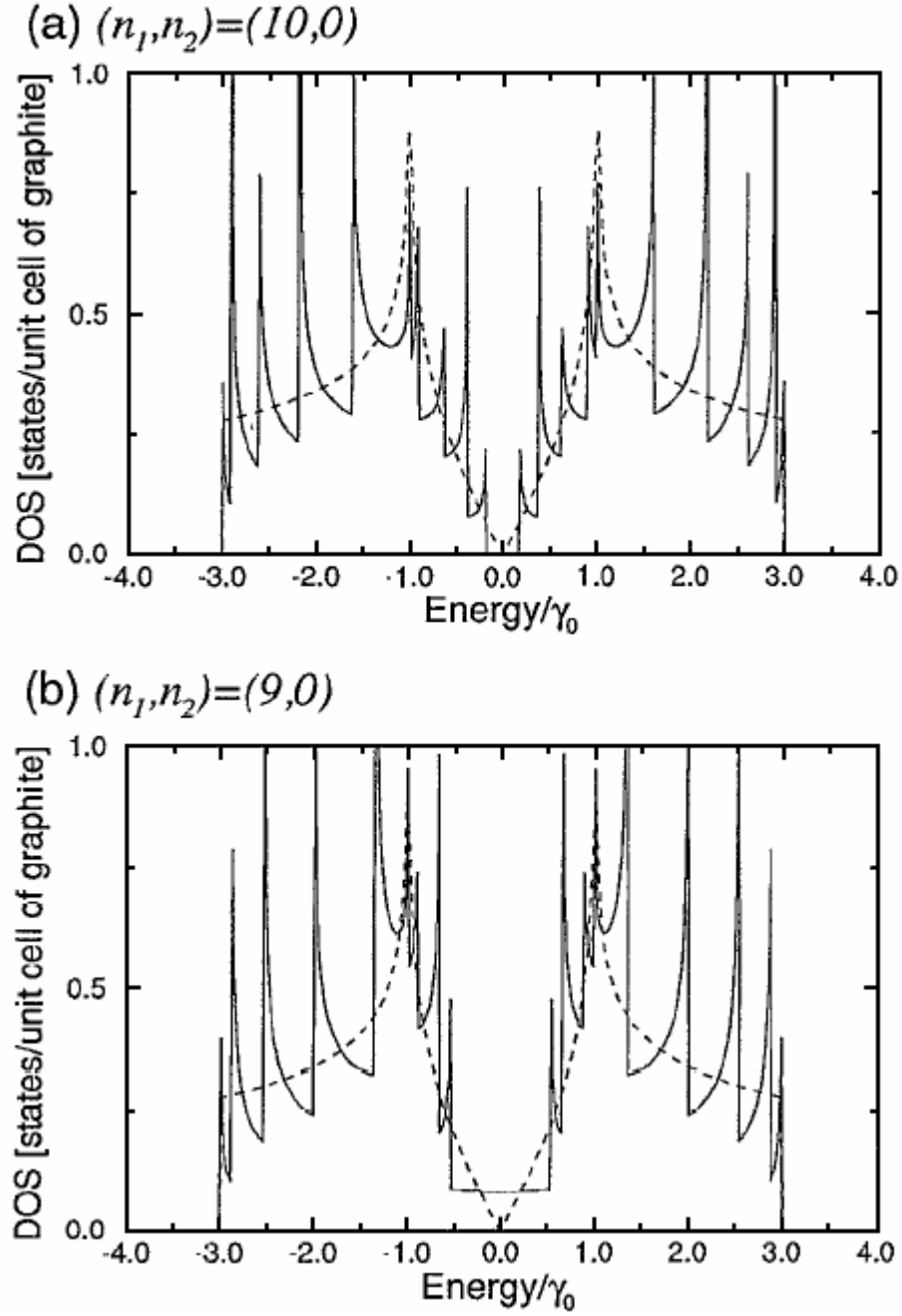


**Figure 4.7** Electronic density of states for (a) (10,0) zigzag SWNT and (b) (9,0) zigzag SWNT. The SWNT represented in (a) shows a small energy gap between the first singularities with no density of states at the Fermi level and is thus semi-conducting, whereas (b) shows a finite density of states at the Fermi level and is thus metallic. The dotted line is the density of states for 2D a graphene sheet.<sup>23</sup>

### 4.3 Review of Single Walled Carbon Nanotube Thin Films

As discussed in the previous section, SWNTs exist as either metallic or semi-conducting, depending on their chirality. As a result of their one dimensional structure and covalently bonded  $sp^2$  configuration, metallic SWNTs have been shown to carry currents with densities exceeding  $10^9$  A/cm<sup>2</sup>,<sup>28</sup> substantially higher than the current densities in metals (e.g.  $\sim 10^4$  A/cm<sup>2</sup> for copper wire at 20°C), making them useful for applications such as interconnects<sup>29</sup>. Alternatively, semi-conducting SWNTs have been shown to function as field effect transistors (FETs) at room temperature.<sup>30</sup> While the use of individual SWNTs has shown promise, all known synthesis methods<sup>20,21,31</sup> result in a mixture of metallic and semiconducting SWNTs. In addition, SWNT bundles form during growth<sup>32</sup>, making the separation and utilization of individual SWNTs difficult. Thus, fabricating reproducible and uniform devices from individual SWNTs has proven to be challenging.

An alternative to individual SWNT electronics is to fabricate thin films from dispersed SWNTs. In 2003, Snow et al. demonstrated that low density random networks of SWNTs behave as p-type semiconductors with field-effect mobilities of  $\sim 10$  cm<sup>2</sup>/V s, which is higher than materials such as amorphous silicon,<sup>12</sup> commonly used in thin film transistors (TFTs). Since SWNTs have an aspect ratio of  $\sim 10^3$ , conduction at a very low volume fraction occurs via percolation between sticks. In 2004 Wu et al. utilized a simple vacuum filtration process to produce uniform transparent and conducting SWNT thin films, which can be deposited on a variety of substrates<sup>14</sup>. Continued work in this field has led to the fabrication of SWNT thin films which have transmittance of  $\sim 80\%$  at wavelengths ranging from ultraviolet, visible and infrared.

Furthermore, the films have high conductivities with sheet resistance as low as  $120 \Omega/\square$ .<sup>33</sup> These conductivity values are comparable to ITO. Therefore, it is feasible that SWNT thin films could be replaced for ITO in realistic applications such as the transparent and conducting electrode in OPVs. An advantage of SWNT thin films of ITO would be, if similar performance could be achieved, is that they can be processed from solution on cheap substrates.

#### 4.3.1 Purification of SWNTs

In order to fully utilize the extraordinary properties of SWNTs, the starting raw materials must be purified, especially for optoelectronic applications. The need for purification arises from the fact that as-produced SWNTs contain catalyst, amorphous carbon and polyhedral graphite as by-products from the synthesis process. Extensive procedures for the purification of SWNTs have been developed in our group and are described elsewhere.<sup>26</sup> However, the salient features of the purification process are described here.

To begin, we obtained commercially available SWNTs produced using the high pressure carbon monoxide (HiPCO)<sup>31</sup> process from Carbon Nanotechnologies, Inc. These SWNTs were selected because they are readily available at a reasonable cost and the sidewalls are generally free of amorphous carbon scale<sup>31</sup> that is frequently found on SWNTs produced using laser<sup>32</sup> or arc-discharge<sup>18, 19, 34</sup> methods. Thus, purification was generally limited to the removal of some amorphous and graphitic carbon, and carbon encapsulated iron catalyst particles. The purification also introduces defects (usually vacancies resulting from etching in acid) in the SWNTs which are passivated by

carboxyl [-COOH] groups. Our purification method is that of Zhou et al.<sup>35</sup> and involves two steps. The first step involves annealing raw SWNTs in air at approximately 225°C for 24 hours to oxidize the iron catalyst particles by reducing the amorphous carbon encapsulation layer around the catalyst particle. The formation of FeO<sub>x</sub> allows it to more readily react with HCl. The second step involved sonication and stirring the SWNTs in 6M to 12M hydrochloric acid (HCl) at approximately 80°C. The HCl reacts with the oxidized iron particles, resulting in iron salts which are readily filtered out in solution. The solution is then filtered through a 1µm Teflon filter paper and repeatedly rinsed with deionized water until a pH ~ 7 is achieved. This process is repeated until the desired purity was achieved.

In order to assess the purity of the SWNTs after each iteration of the purification process, thermal gravimetric analysis (TGA) and transmission electron microscopy (TEM) were utilized. TGA is a simple technique which measures the weight change of a material as a function of temperature. Figure 4.8 shows the TGA curves for the HiPCO SWNTs used in this work before and after purification. The TGA curve for the as received SWNTs (blue curve in Figure 4.8) shows a slight increase in weight up to ~290°C, consistent with oxidation of the iron catalyst particles. The subsequent decrease in weight is due to the decomposition of the SWNTs at ~422°C (determined by the inflection point of the curve). The residual catalyst content indicated by the flat portion of the curve above ~500°C was found to be ~25% for the as-received HiPCO SWNTs. After purification (red curve in Figure 4.8) the TGA curve above 500°C shows that virtually all of the catalyst has been removed. Our TGA revealed that the decomposition of SWNTs occurs at ~530°C and ~2% residual catalyst remains above



~700°C. From Figure 4.8, it can be seen that the decomposition temperature of purified SWNTs is higher than for as-received ones. This is attributed to the fact that catalyst particles decrease the decomposition temperature by promoting the oxidation reaction.<sup>35</sup>

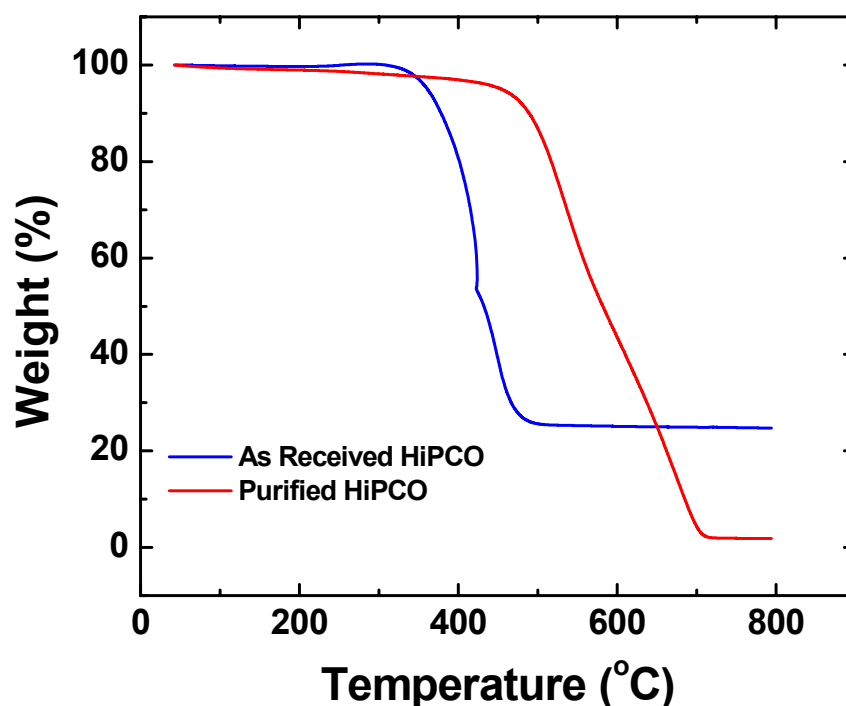


**Figure 4.8** TGA curves for as received and purified HiPCO SWNTs showing that the catalyst content in the raw SWNTs is ~25% compared to being only ~2% after purification. Also, the decomposition temperature of purified SWNTs is higher.

TGA provides indirect evidence for the removal of catalyst; therefore direct imaging through transmission electron microscopy (TEM) analysis was performed on raw and purified SWNT samples. The as-received SWNTs contain large amounts of catalyst particle which are readily visible in Figure 4.9(a). In contrast, virtually all of the catalyst particles have been removed in Figure 4.9(b) after purification. These and

other detailed analysis performed in our group indicates that the SWNTs used in this work are highly pure.

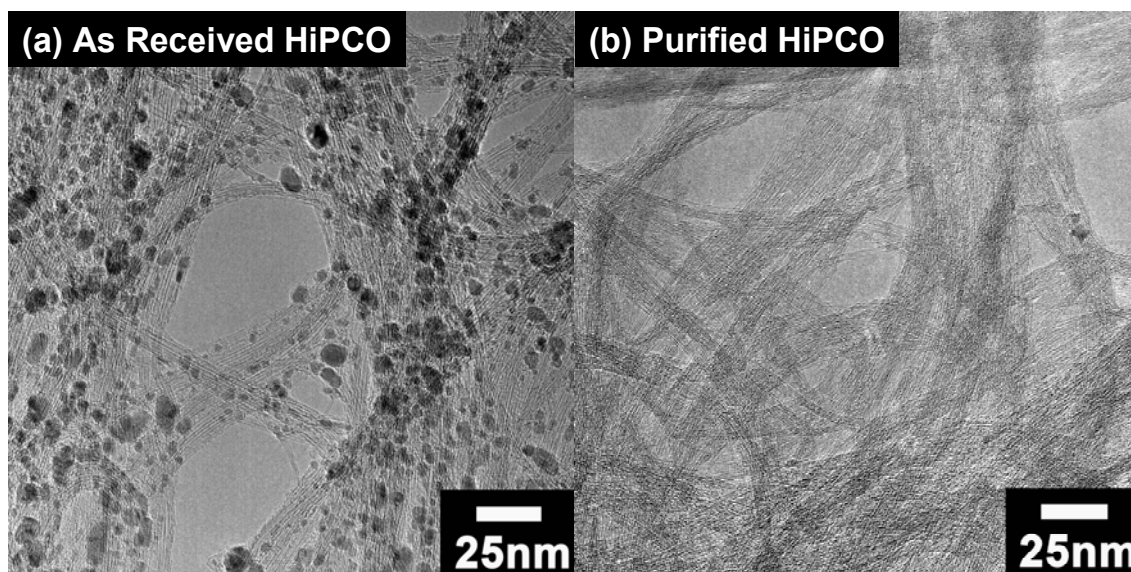


**Figure 4.9** TEM images of HiPCO SWNTs (a) before and (b) after purification.<sup>26</sup>

#### 4.3.2 Preparation of SWNT Thin Films

While many methods for the preparation of SWNT thin films<sup>3-16, 36</sup> have been developed, we have adopted the vacuum filtration method developed by Wu et al.<sup>14</sup> because it utilizes an inexpensive vacuum filtration system which allows for uniform deposition of the thin films on a variety of substrates. Furthermore, it is possible to easily control the film density by manipulating the volume filtered or the concentration of SWNTs in the suspension. The vacuum filtration method involves five basic steps:

- 1) Dispersion of SWNTs in a solution of sodium dodecyl sulfate (SDS) and water.
- 2) Vacuum assisted filtration of the dispersion using a methylcellulose ester (MCE) filter.

- 3) Removal of the SDS by rinsing with water.
- 4) Compressive loading and transfer of the SWNT thin film on glass.
- 5) Dissolution of the MCE membrane in acetone.

The dispersion of the SWNTs in solution is critical for optimizing the electrical and optical properties of the SWNT thin films. SWNTs are hydrophobic with very large Van der Waal's attraction amongst the particles. Thus, the SWNTs tend to form bundles and have low levels of solubility in most solvents. Bundles are detrimental for optoelectronic properties because they have a high optical cross section, decreasing the transmission. Further, large bundles make it difficult to obtain smooth, thin homogeneous films with repeatable optoelectronic properties. Therefore, it is necessary to create stable solutions of individual SWNTs or very small bundles through the use of a surfactant. Perhaps the most prevalent surfactant used in the dispersion of SWNTs is SDS,<sup>37-40</sup> typically used in a ratio of 1 wt% in deionized (DI) water.

An image of the vacuum filtration apparatus is shown in Figure 4.10. A vacuum pump pulls the SWNT suspension through the MCE 0.2 $\mu$ m pore filter placed between the glass funnel and glass filter as shown in Figure 4.10. The MCE membrane captures suspended SWNTs, allowing the water and SDS to pass through. The density of the SWNT thin film is controlled in two ways: by changing the amount of solution filtered or by changing the concentration of SWNT in the suspension. As SWNTs accumulate on the MCE filter, solution flow will continuously favor less saturated regions allowing for homogeneous thin film formation on the filter paper.

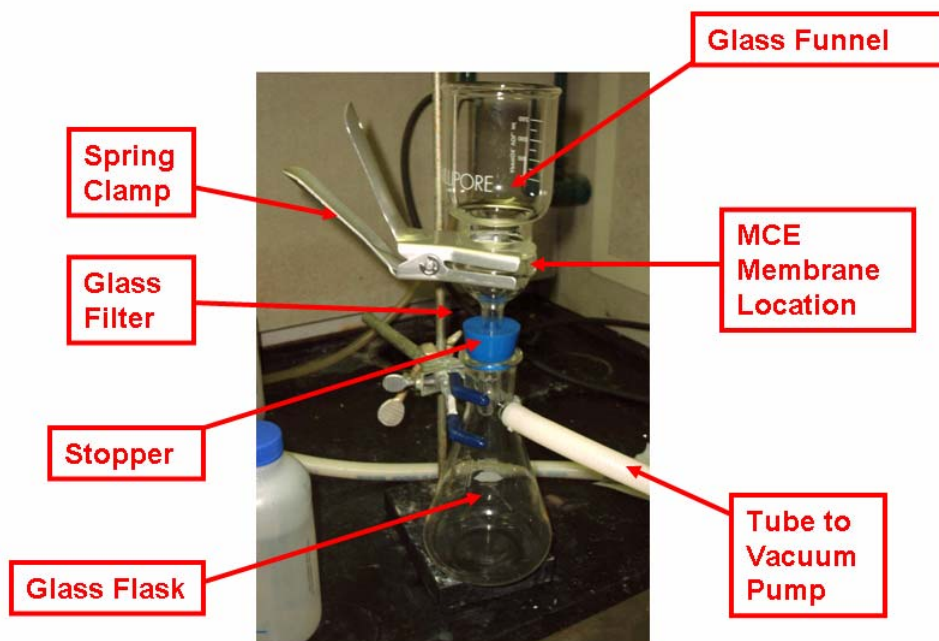


**Figure 4.10** Image of the vacuum filtration apparatus used to prepare the SWNT thin films.<sup>26</sup>

Once the SWNT suspension has completely passed through the MCE filter, the filter is allowed to dry, which prevents re-dispersion of the SWNTs when rinsing. Then the SWNTs on the filter membrane are repeatedly rinsed with DI water to remove the residual SDS. Figure 4.11 is a schematic of the thin film deposition process onto substrates. The SWNT thin film on the MCE membrane is placed film down onto a substrate and smoothed using a cylindrical weight to remove bubbles and ensure adhesion. The assembly is then covered with drying paper and glass, and placed under compression in a vacuum oven at 70°C for at least 1 hour. Once dry, the substrate, SWNT thin film and MCE membrane are placed in an acetone bath where the MCE membrane dissolves. The remaining thin film is then rinsed with methanol and dried with nitrogen.

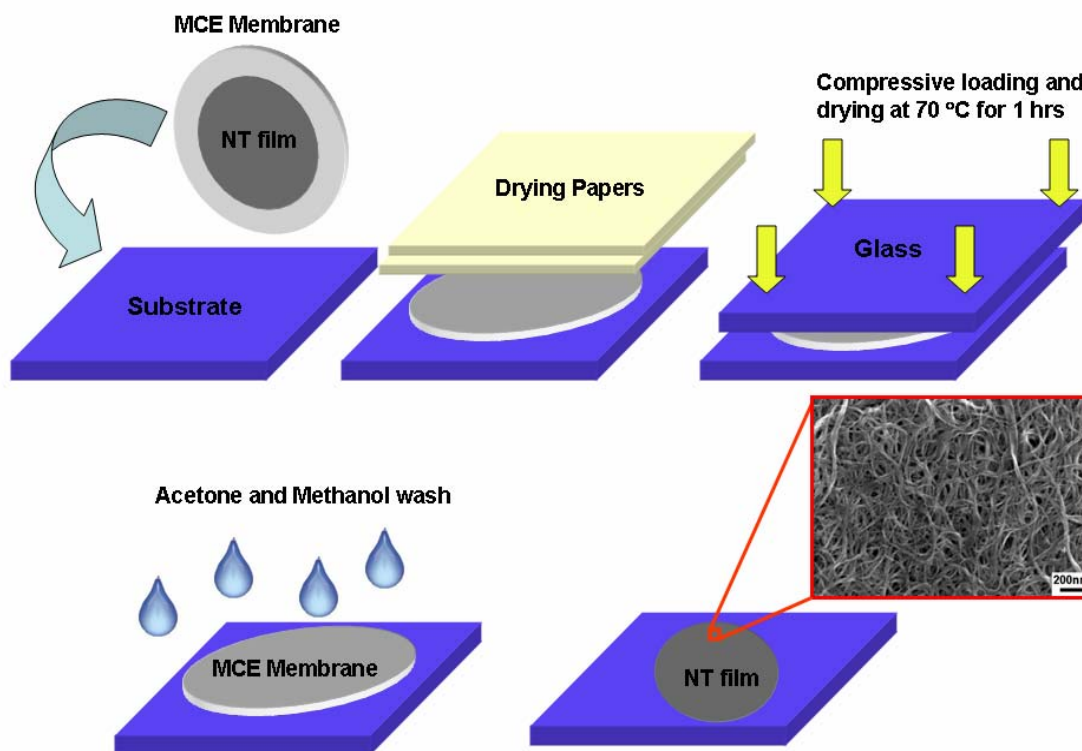


**Figure 4.11** Schematic of the SWNT thin film deposition process. After filtration, the MCE membrane is covered with a glass slide and drying papers, compressively loaded and dried at 70 °C for at least 1 hour. The membrane is then dissolved in acetone and washed with methanol. The as-deposited films are dried with nitrogen prior to processing them for devices.<sup>26</sup>

### 4.3.3 Characterization of SWNT Thin Films

The matrix of SEM images shown in Figure 4.12 demonstrate how the SWNT thin film density can be varied by manipulating the filtration volume and/or the SWNT concentration using the vacuum filtration method. It is clear from this figure that higher concentration and higher filtrate volume films are denser, which leads to higher conductivity, but lower transparency. As the objective of this work was to utilize

SWNT thin films as a replacement for ITO, a balance between the transparency and conductivity was achieved through the determination of the conductivity threshold.

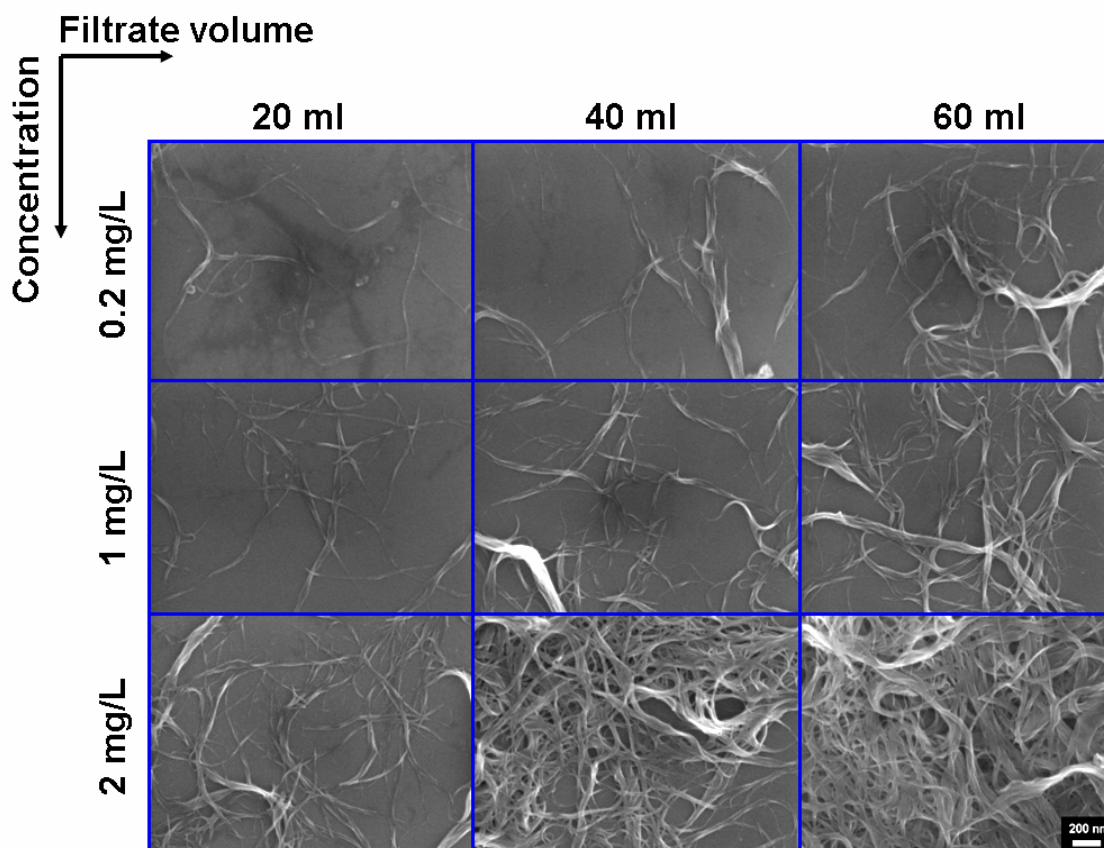


**Figure 4.12** Scanning electron micrographs of SWNT thin films showing how different filtration volumes and SWNT concentrations affect the film density.<sup>26</sup>

Extensive work relating percolation theory to the electrical properties of SWNT thin films was performed by others in our group and details can be found elsewhere.<sup>13, 26</sup> Utilizing this knowledge, the preparation and characterization of SWNT thin films for this work were limited to concentrations and/or filtrate volumes above the metallic SWNT percolation threshold where the most conductive films are produced. Figure 4.13 shows a plot of the relationship between the conductivity and the relative fraction of the voids occupied by the SWNTs (volume fraction). Using the fit indicated by the

curve obtained from the percolation theory in Figure 4.13, the percolation threshold was found to be  $\Phi_C \approx 5.5 \times 10^{-3}$ . Thus, a very small fraction of the substrate needs to be covered with SWNTs to achieve percolation. SWNT thin films fabricated below this threshold have a high sheet resistance. It can also be seen that above the percolation threshold, the relationship between conductivity and SWNT volume fraction is super linear. Therefore, SWNT thin films deposited from a 2mg/L concentrated suspension which were sufficiently conducting were utilized as transparent and conducting electrodes for OPVs.

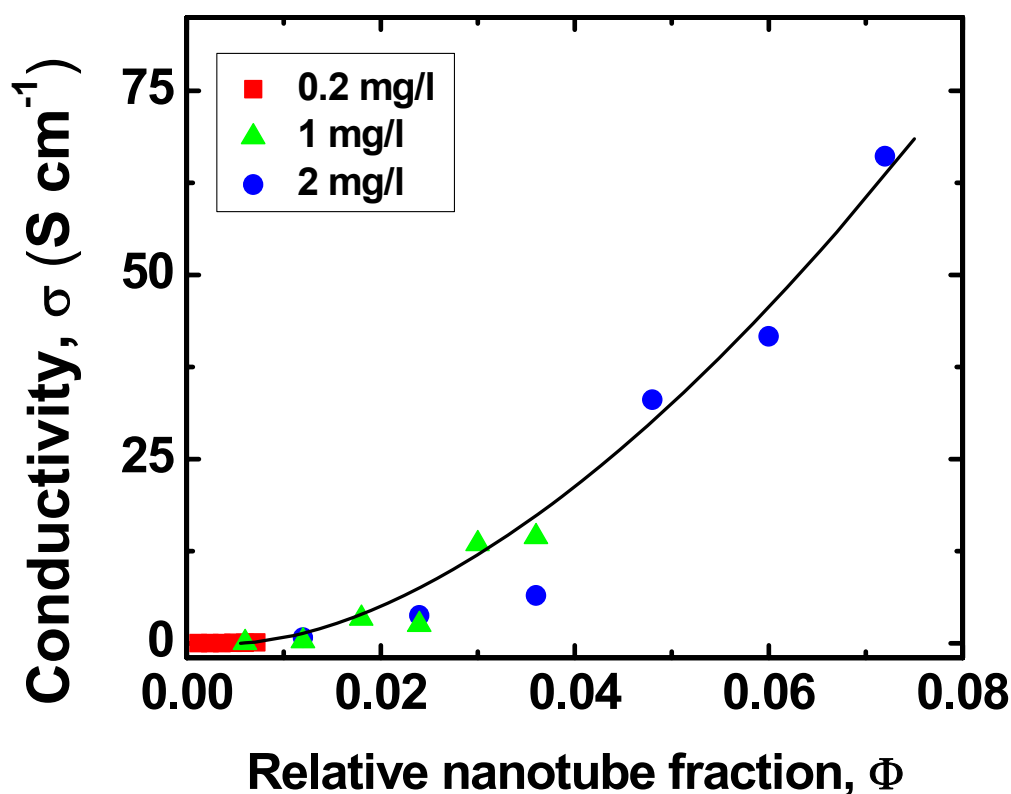


**Figure 4.13** Plot of the relationship between the conductivity of various SWNT thin films and the relative volume fraction of the SWNTs. The curve is a fit using the percolation theory.<sup>26</sup>

Six SWNT thin films of different thicknesses, ranging from 30-200nm, were deposited by varying the filtration volume of the 2mg/L SWNT suspension. The filtration volume was varied in 10ml increments from 10 to 60 mL. The UV-Vis transmission spectra of the six films are shown in Figure 4.14(a). The data in the figure shows that the transmission is relatively consistent across the entire spectrum from  $\lambda=250$  to 850 nm. It is also clear from Figure 4.14(b) that overall transmission decreases roughly linearly with increasing film thickness (increasing filtrate volume). The transmission of SWNT thin films remained unchanged with wavelength over the entire range. ITO, on the other hand, is opaque below  $\lambda=300$  nm. The thinnest SWNT thin films (30mL) were found to be more transparent than ITO.



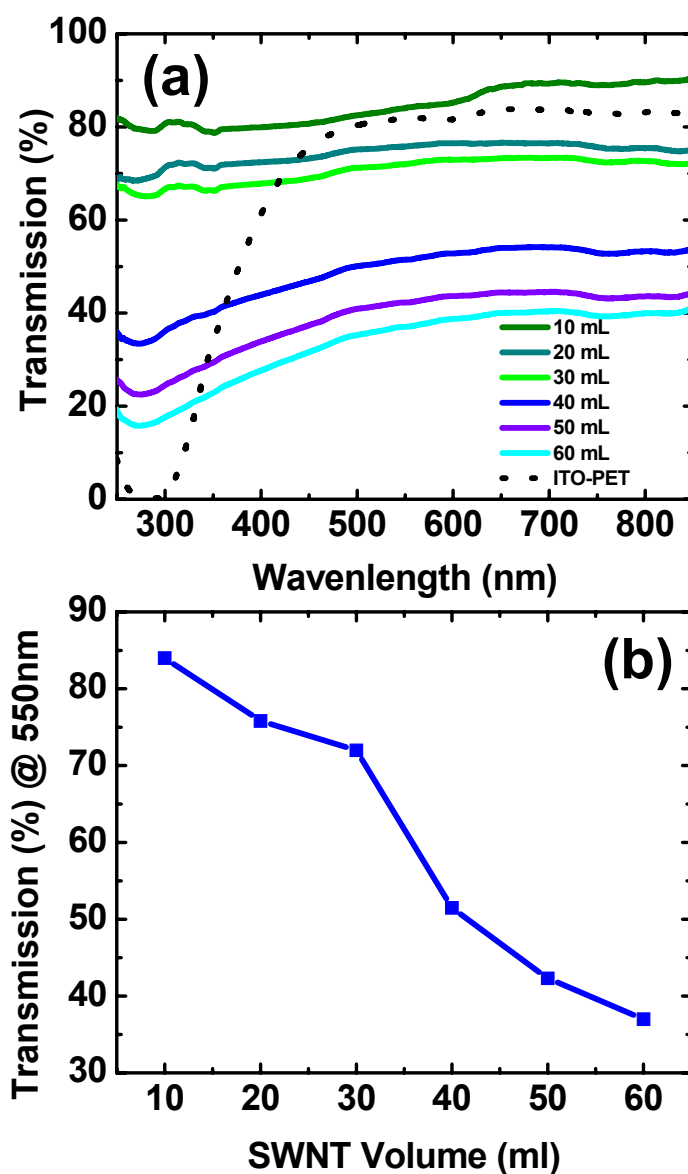


**Figure 4.14** (a) UV-Vis and (b) transmission characteristics at  $\lambda=550$  nm for SWNT thin films deposited from filtration volumes ranging from 10 mL to 60 mL with 2mg/L suspension.

Surface resistivity measurements were obtained by performing a  $\pm 1$  V I-V scan at a sweep rate of 100 mV/s between two gallium contacts of diameter  $D = 1.5$  mm and separated by a distance  $L = 3$  mm. The formula used to calculate surface resistivity was  $\rho = (V/L)/(I_s/D)$ , where  $V$  is the voltage and  $I_s$  is the current across the measured

area.<sup>41</sup> The  $V/I_s$  ratio was obtained from the slope of the I-V scans, which were perfectly linear over the voltage range tested. A plot of resistivity as a function of the filtrated volume is shown in Figure 4.15(a). It can be seen in this figure that in general the resistivity decreases as the solution volume increases due to the increase in density of the SWNT thin films. The lowest resistivity measured was  $178 \Omega/\square$  for the 50 mL SWNT compared to  $25 \Omega/\square$  for the ITO-Glass substrates.

Figure 4.15(b) shows transmittance as a function of resistivity for the SWNT thin films at  $\lambda=550$  nm. The linear relationship is consistent with the increased density and number of percolating pathways amongst the SWNTs.

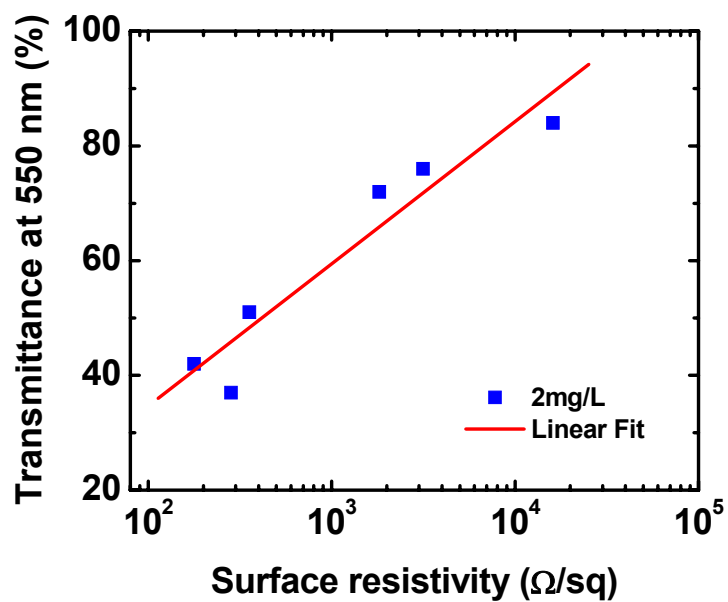
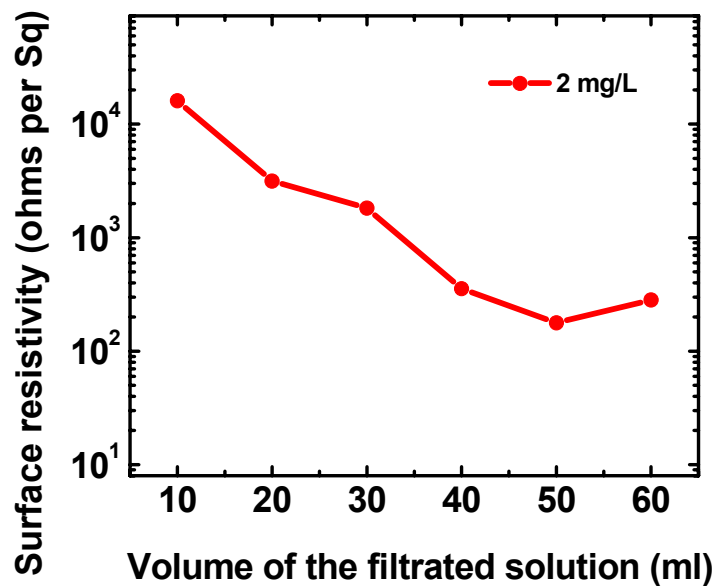


**Figure 4.15** (a) SWNT thin film surface resistivity as a function of filtration volume and (b) SWNT thin film transmittance versus sheet resistance for the thin films in (a).

#### 4.4 SWNT Thin Films as Transparent and Conducting Electrodes in OPVs

The transparent and conducting electrode utilized in most OPVs is ITO coated glass. In addition to the high cost and supply limitations discussed earlier in this chapter, recent studies<sup>42</sup> have pointed out that the conductivity of ITO is a source of series resistance which decreases the short-circuit current, fill factor and power conversion efficiency of photovoltaic devices, especially large area devices. Further, the crystal structure of ITO makes it fragile and rigid, and thus, not a good choice for use on flexible substrates such as PET. The primary objective of the work performed in this part of the thesis was to demonstrate OPVs with SWNT thin films as the transparent and conducting electrodes. Thus, providing an alternative to ITO that is solution processed and flexible.

Bulk heterojunction OPVs with the structure shown in Figure 4.16 were prepared by drop casting a 2.5 g/L solution of P3HT:PCBM 1:1 in chlorobenzene. A layer of poly(ethylenedioxy) thiophene:poly(styrene) sulfonate (PEDOT:PSS) (PEDOT:PSS: MeOH 1:2) was spin-coated on the SWNT-glass and on ITO-glass reference substrates. Gallium-Indium (Ga-In) eutectic (as described in Chapter 2) was used as the top electrode. The photoactive area tested was  $0.07 \text{ cm}^2$ . A rubber o-ring of 3mm diameter was used to contain the Ga-In droplet and control the back contact area. As discussed in Chapter 2, Ga-In melts at  $15.7^\circ\text{C}$ , and is very convenient for making contacts without the need of a metal evaporator. Unlike mercury, it is non-toxic, and has a work function of 4.2 eV, slightly lower than the 4.3 eV of the commonly used aluminum. The lower work function may result in higher built-in potential, which can enhance electron-hole pair dissociation.

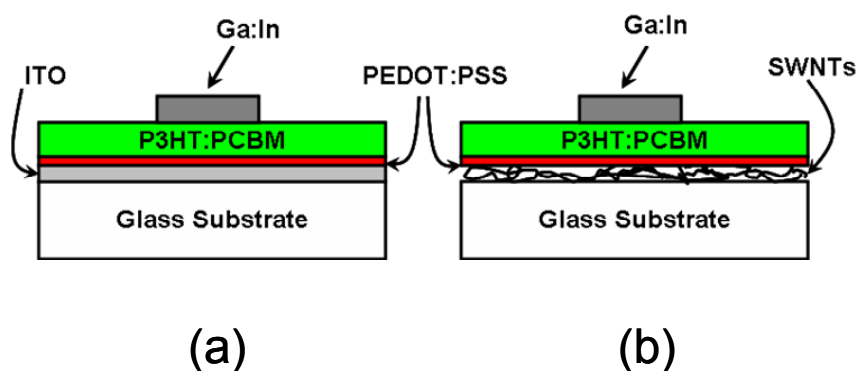


**Figure 4.16** Schematic of P3HT:PCBM OPV, with ITO (a) and SWNT thin film (b) as the hole collecting electrodes.

The photovoltaic characteristics of the SWNT and ITO reference devices were evaluated. The devices were optimized by annealing up to 100°C in air by illumination while monitoring the evolution of photovoltaic device characteristics (see Chapter 2 for discussion regarding *in situ* annealing) until maximum efficiency was achieved. Figure 4.17 shows the efficiency, fill factor, short-circuit current ( $I_{sc}$ ), and open-circuit voltage ( $V_{oc}$ ) of the devices at various light intensities. It can be seen from this figure that only the 50ml SWNT thin film device and ITO reference device showed noticeable efficiencies. The low current density and fill factor in the other SWNT devices suggest decreased shunt resistance in the devices, probably the result of vertically oriented SWNTs or the presence of large bundles.

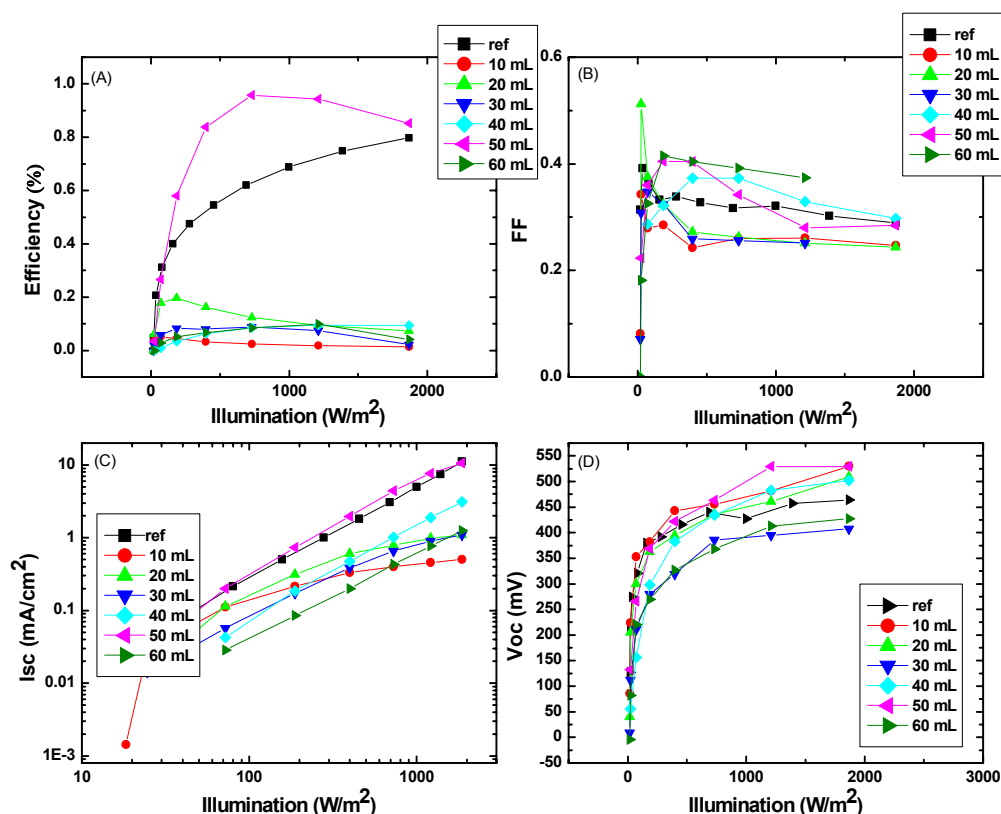


**Figure 4.17** (a) Efficiency, (b) fill factor (FF), (c) short-circuit current ( $I_{sc}$ ) and (d) open-circuit voltage ( $V_{oc}$ ) at various illumination intensities for P3HT:PCBM OPVs with SWNT thin films and ITO as a hole collecting electrode.

The current density versus voltage (I-V) in dark and under illumination ( $100\text{mW/cm}^2$ ) with ITO and the 50ml SWNT thin film devices, respectively, are plotted in Figure 4.18. The significantly higher dark current under forward bias (positive voltage on transparent and conducting electrode) indicates distinct diode behavior. The log I-V characteristics are shown in the inset of Figure 4.18. The fill factor and open-circuit voltage for these devices were lower than the best published results, which are attributed to the fact that the devices were fabricated and measured in air and used Ga-In as the electrode material. The best published results were generally for devices

fabricated and/or measured in inert environments such as argon or nitrogen. In addition, these devices had yet to be optimized. Thicker than optimum (800 vs. 100 nm) P3HT:PCBM thin films by drop casting were used here to avoid short-circuit problems. Nevertheless, the drop cast reference cells on glass-ITO/PEDOT:PSS, of the same thickness from the same solution, yielded a similar fill factor of 0.3 but lower photocurrents of  $5\text{mA/cm}^2$  compared to  $6.65\text{ mA/cm}^2$  at  $100\text{mW/cm}^2$  of white light. Hence, the cells using SWNT thin films for hole collection had a higher conversion efficiency of 0.99%, vs. 0.69% for the reference cells.

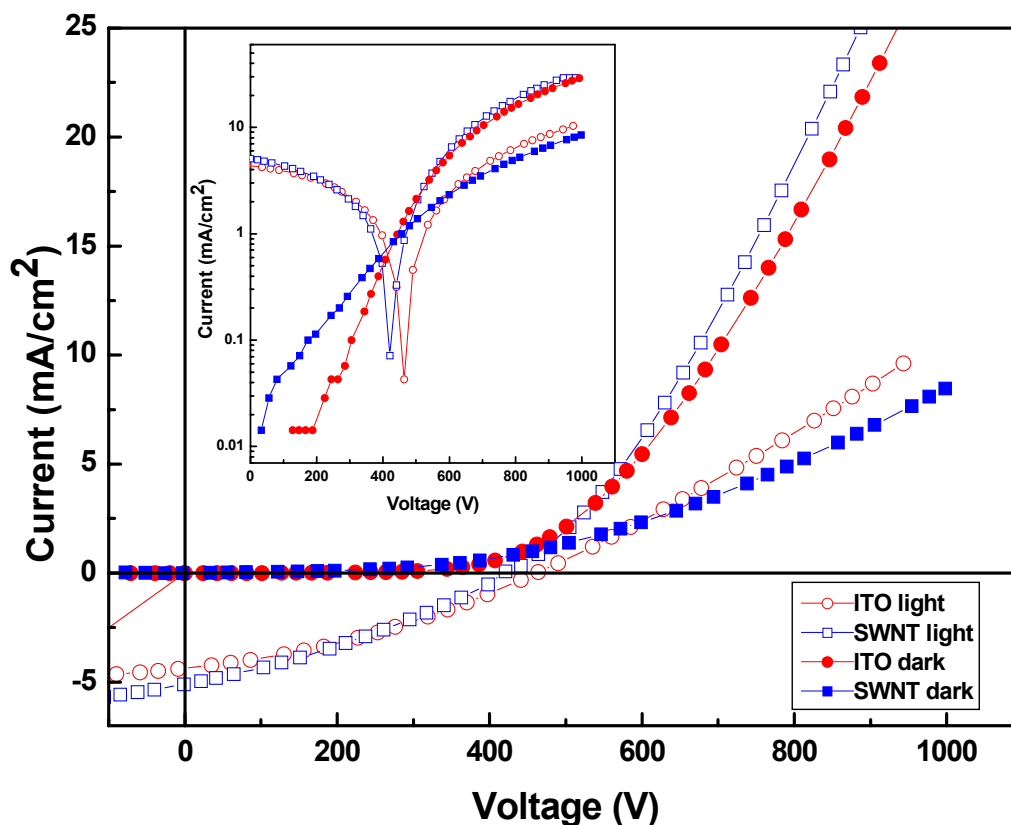


**Figure 4.18** I-V curves at  $100\text{mW/cm}^2$  halogen white light and in the dark of reference solar cell on ITO-glass and the best solar cell using a SWNT thin film. Log I-V characteristics are shown in the inset.

In order to confirm that the improved efficiency in the devices is attributed to the incorporation of the SWNT thin film electrode and not PEDOT:PSS, additional cells were fabricated without the PEDOT:PSS layer on SWNT electrodes. Our experiments revealed that for thin P3HT:PCBM films (2.5g/L), the devices shorted in the absence of PEDOT:PSS. However, working cells with efficiency values lower than our best devices were obtained for thicker P3HT:PCBM films (10 g/L). On the other hand, devices fabricated using only PEDOT:PSS coated on glass as the anode layer without SWNT thin films yielded extremely low currents. This suggests that SWNT thin film electrodes play an essential role in hole collection and in-plane conductivity of our photovoltaic devices. One interpretation is that since SWNTs are a mixture of metallic and p-doped nanotubes, PEDOT:PSS is necessary to adjust the SWNT work function for hole collection and avoid device shorting by having the metallic nanotubes transport electrons from the PCBM network to the transparent electrode. The charge transfer and transport in the SWNT/P3HT:PCBM/Ga-In system can be understood from the energy diagram shown in Figure 4.19. Excitons are generated in the P3HT, and hole transfer is possible through the PEDOT and the conduction band of the semiconducting SWNTs (s-SWNTs). Electrons are injected in the lowest unoccupied molecular orbital of PCBM, then collected by the Ga-In contact. In theory, electron transfer is also possible in the metallic SWNTs (*m*-SWNTs), which could account for some exciton dissociation. However, in this device configuration, the SWNT network is not in direct contact with the top Ga-In electrode, making electron collection unlikely. Thus, in this case, the SWNTs only serve as a hole conducting network.



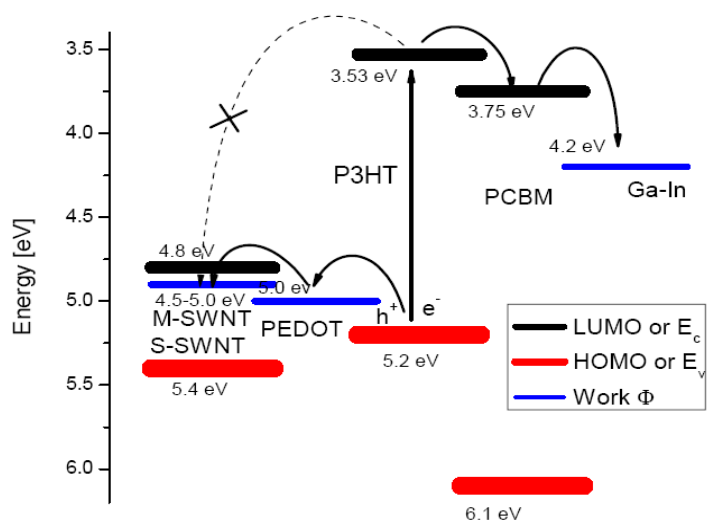


**Figure 4.19** Energy level diagram adjusted in relation to the vacuum level for the SWNT/PEDOT:PSS/P3HT:PCBM/Ga-In device. The arrows indicate hole and electron flows. *m*-SWNTs and *s*-SWNTs refer to metallic and semiconducting SWNTs, respectively. Energy diagram was constructed using References <sup>43-45</sup>

Although the maximum UV-Vis transmission was found in the 10 ml sample (see Section 4.3.3), we obtained the best photovoltaic characteristics with the 50 ml sample (thickness  $\approx 300$  nm), the one having the lowest surface resistivity. We also observed a general trend of an increase in performance with the increase in SWNT thickness. A comparison of the photovoltaic characteristics of devices fabricated on ITO and transparent and conducting SWNTs is given in Table 4.1. It can be clearly seen that the photovoltaic performance of the SWNT devices is significantly improved relative to those with ITO.

**Table 4.1** Solar cell parameters at 100 mW/cm<sup>2</sup> illumination for the reference cell on ITO-PET substrate and the best solar cell on SWNT-glass substrate.

Values @ 100 mW/cm <sup>2</sup>	ITO-glass drop cast reference	Best SWNT-Glass Drop cast
% efficiency	0.69	0.99
FF	0.32	0.3
I <sub>sc</sub> (mA/cm <sup>2</sup> )	5	6.65
V <sub>oc</sub> (mV)	426	500

We attribute these results to the formation of a 3D network consisting of a SWNT skeleton and voids in the films. Although the very thin films are highly transparent, they lack the sheet conductivity due to insufficient surface coverage [see Figure 4.20(b) and refer back to Figure 4.15(b)] to efficiently collect the holes. The conductivity of the SWNT films increases with film thickness while the transparency decreases. The enhancement in conductivity is attributed to the formation of a continuous 3D network that allows efficient current flow primarily through interconnected metallic SWNTs. A closer observation of the SEM image in Figure 4.20(a) reveals the presence of voids in the SWNT thin film 3D network. The substrate is clearly visible at the bottom of these voids as indicated by the arrows in Figure 4.20(a).

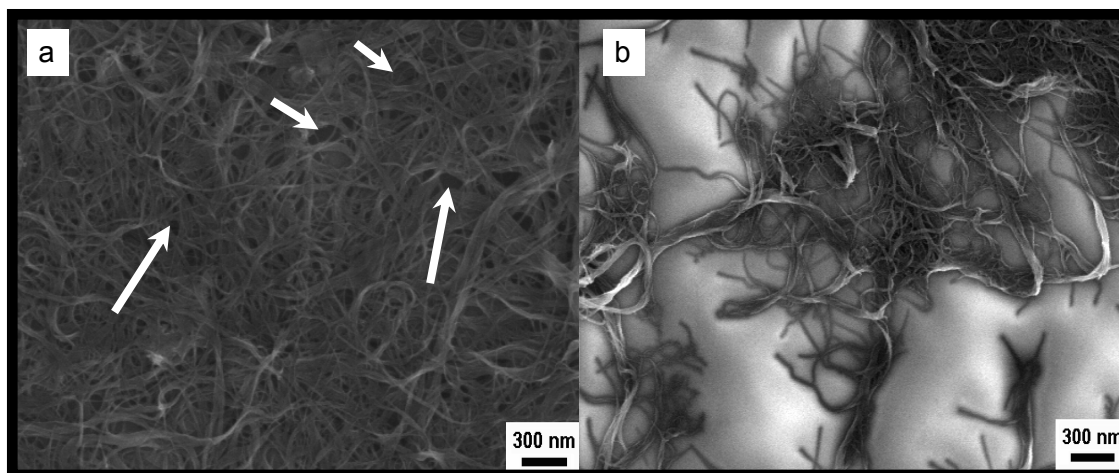


**Figure 4.20** SEM images of SWNT films deposited on Glass, from 50 ml SWNT solution (a) and 10 ml SWNT solution (b). The arrows on image (a) indicate the presence of voids that illustrate the three-dimensional nature of the coating.

The presence of the voids is an important factor in understanding the results. They suggest that the PEDOT:PSS and P3HT + PCBM mixture infiltrate the voids when deposited on top of the SWNT thin films. Thus, some of the PEDOT: PSS and P3HT +

PCBM is essentially deposited on the surface of the glass substrate while being in intimate electrical contact with the SWNTs. Therefore, some of the polymer nanocomposite is directly exposed to the illumination that is transmitted through the glass substrate. That is, although the overall transparency of the 50 mL film is lower in comparison to ITO, the presence of the voids in the 3D SWNT network provides sufficient exposure of the nanocomposite to the illumination to efficiently create excitons at the P3HT/PCBM interface and collect holes at the SWNT electrode. We attribute the main limitation in efficiency to the excessive thickness of the devices (800 nm). Attempts to use spin-coating instead of drop-casting were unsuccessful, as they resulted in shorted devices. We believe that higher efficiencies will be possible through better engineering of the SWNT thin films. That is, through improvement of the in-plane conductivity of thinner SWNT films.

#### **4.5 Birefringence in SWNT Thin Film OPVs**

Low density networks of SWNTs have been shown to be transparent and conducting.<sup>3, 5, 6, 9, 10, 13, 15, 46, 47</sup> Further, as demonstrated above and by others<sup>9</sup>, thin films of SWNTs are a viable alternative to ITO for use as the hole collecting electrode in OPVs. However, these studies have only considered the characteristics of OPVs with illumination under a normal angle of incidence. As the practical use of most photovoltaic devices would likely be under illumination from angles other than normal, the use of SWNT thin films as a transparent and conducting electrode under these conditions has been investigated. By evaluating transmittance of SWNT thin films at

different angles of incidence, evidence of optical anisotropy in SWNT networks was found.

Transparent and conducting SWNT thin films (10 to 80ml at 2mg/L) on glass were deposited using the methodology described in Section 4.3.2. Transmittance values for these films were obtained at various angles of incidence from 0-70°; the results for two films of very different densities (20ml and 60ml) are presented in Figure 4.21(a). By plotting the transmittance where  $\lambda=550\text{nm}$  as a function of the angle of incidence [Figure 4.21(b)], it can be seen that the transmittance values for SWNT thin films decrease approximately according to the cosine law:

$$T_{\text{SWNT}}(\lambda, \theta) \approx T_{\text{SWNT}}(\lambda, \theta=0) \cdot \cos(K \cdot \theta) \quad \text{Eq. 4.10}$$

Where  $K \approx 0.6 \text{ rad}^{-1}$  across the entire spectrum. In contrast, Figure 4.21(b) shows that the corresponding transmittance of a 100nm thick ITO layer on glass is virtually independent of  $\theta$ . It should be noted that at normal incidence, the 10ml SWNT thin film has approximately the same thickness and refractive index (1.7-1.8 at  $\lambda=550\text{nm}$ ) as the ITO. Therefore, SWNT thin films appear to optically anisotropic.

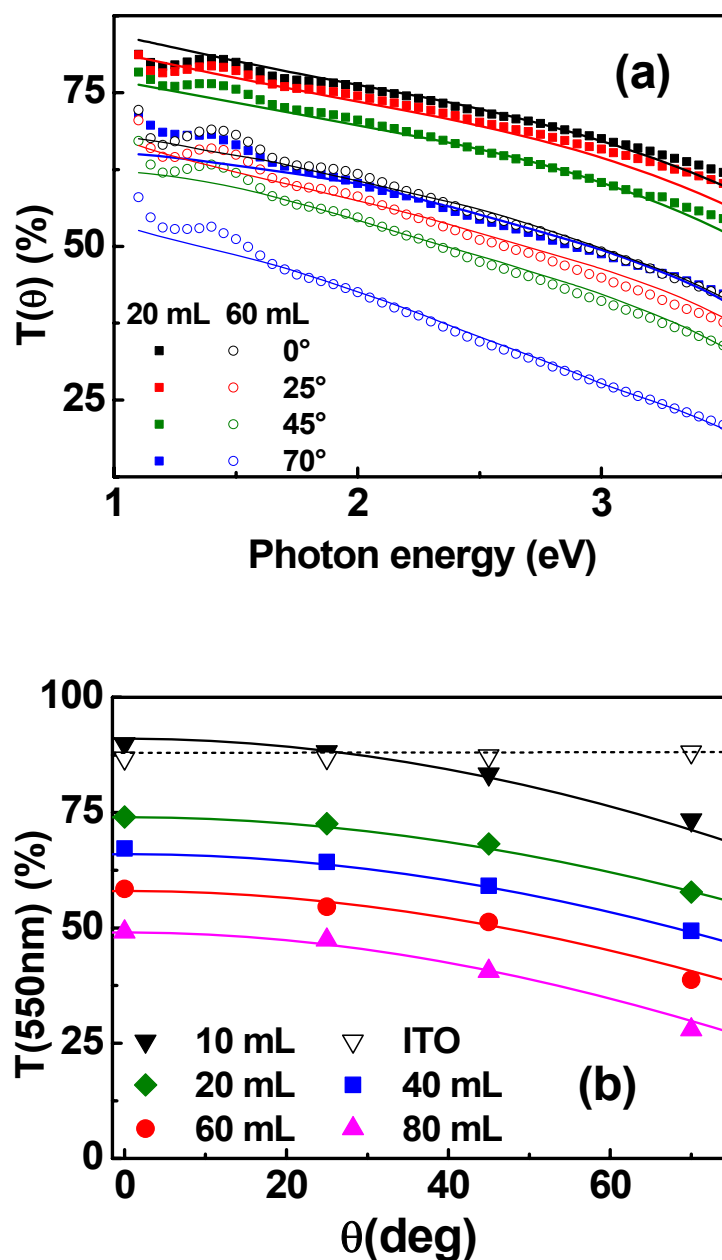


**Figure 4.21** (a) Transmittance of ITO and SWNT thin films on glass as a function of the photon energy ( $E$ ) at four incidence angles  $\theta=0-70^\circ$ . (b) Angular dependency of the transmittances for ITO and SWNT thin films at  $\lambda=550\text{nm}$  showing the cosine dependence of  $\theta$  for SWNT thin films and independence of  $\theta$  for ITO.

OPVs were assembled on top of the SWNT thin films by spin coating at 600 rpm  $\sim 200\text{nm}$  of P3HT:PCBM 1:1 and thermally evaporating aluminum electrodes on top. The devices were thermally annealed at  $120^\circ\text{C}$  for 5 minutes. A reference device

on ITO was prepared in the same manner. A device holder mounted on a precision goniometer was utilized for efficiency measurements at varying angles of incidence.

Figure 4.23(a) shows the relative power conversion efficiencies ( $\eta$ ) as a function of  $\theta$  for the ITO reference device and the one with a 40ml SWNT thin film (i.e. the SWNT thin film leading to optimal efficiency) as the hole collecting electrode. Decreases in efficiency with increasing angle of incidence can be seen for both types of electrodes. However, consideration of the OPV system as a whole demonstrates the anisotropic behavior of the SWNT thin films.

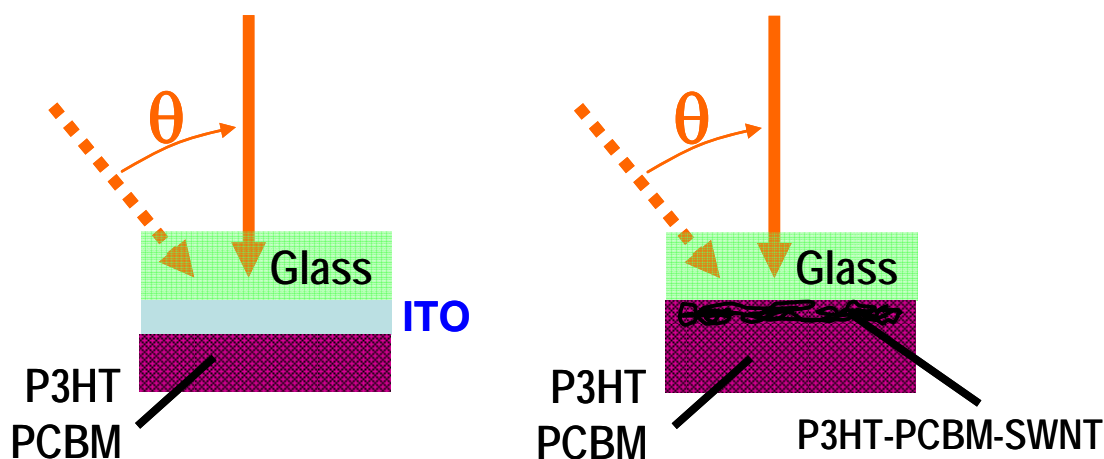


**Figure 4.22** Schematic of an OPV using ITO and a SWNT thin film as transparent electrode and the angular dependency of its transmission.

As shown in Figure 4.22, the amount of light illuminating the P3HT:PCBM active layer depends on the transmittance ( $T$ ) of the electrode, composed of the supporting glass substrate and the hole collecting thin film. In the framework of a thick film approximation,  $\eta$  can be expressed as:

$$\eta(\theta) \sim T(\theta) \approx [1 - R(\theta)] \exp[-\alpha(\theta) d] \quad \text{Eq. 4.11}$$

Since P3HT has a much higher refractive index than both glass and ITO, the angular dependence of reflectance ( $R$ ) is mainly due to the P3HT-ITO interface (for ITO

electrodes) or by the P3HT-glass interface (for SWNT thin film electrodes, which exhibit a poor reflectance due to roughness and light scattering). Thus, for both interfaces reflectivity varies similarly as a function of the angle of incidence as  $R(\theta) \approx 1 - \cos(\theta)$  at  $\theta \approx 0-70^\circ$ .

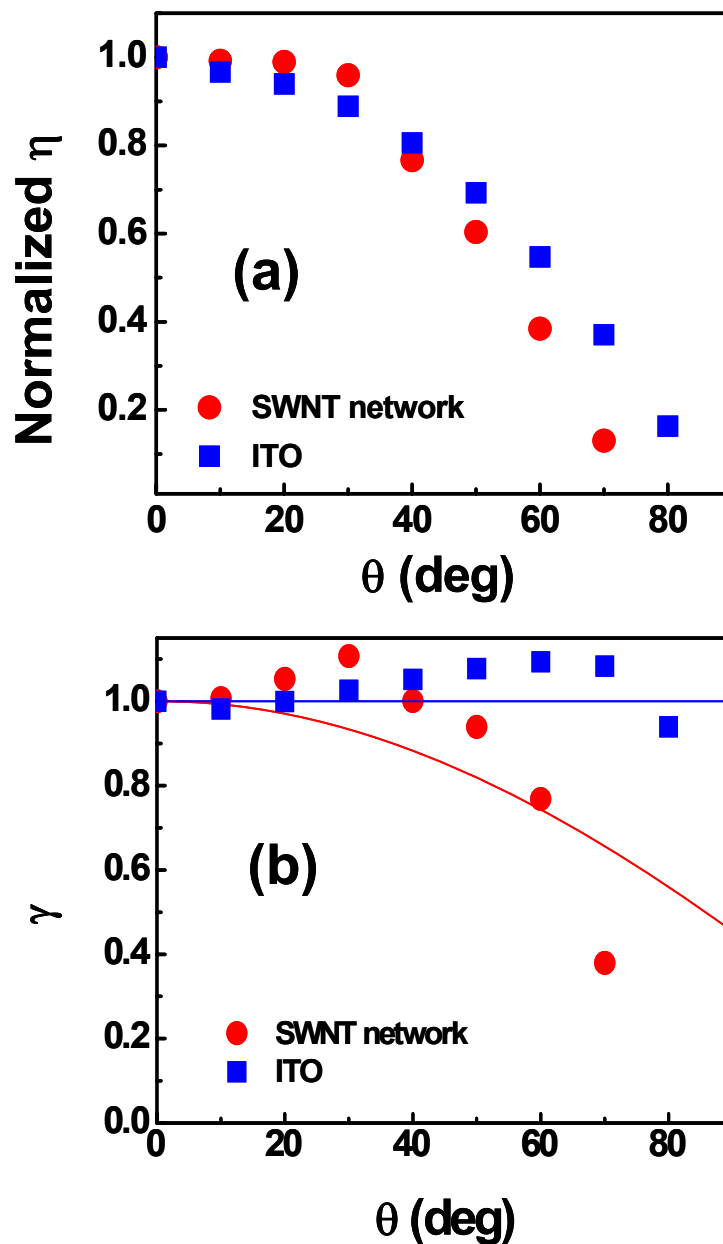


**Figure 4.23** Angular dependency of the relative efficiency ( $\eta$ ) of OPVs using SWNT thin film and ITO as a hole collecting electrode, plotted as (a)  $\eta$  and (b)  $\gamma = \eta/(\eta_0 \cos\theta)$ .

Therefore, defining  $\eta_0$  as the efficiency at normal incidence, the quantity  $\gamma = \eta(\theta) / \eta_0 / \cos(\theta)$  has approximately the same angular dependency of  $\exp[-\alpha(\theta) d]$ , where  $\alpha$  is the absorption coefficient of the electrode and  $d$  its thickness. Since  $\alpha$  depends only on the extinction coefficient  $k = \text{Imag}(\varepsilon^{1/2})$ , any angular dependence of  $\gamma$  reflects the angular dependence of  $\varepsilon(\theta)$  and is indicative of the anisotropy of the transparent, SWNT thin film hole-collecting electrode. Indeed, as shown in Figure 4.23(b),  $\gamma$  is almost independent of  $\theta$  for the OPV using an ITO electrode, while  $\gamma \approx \cos(K \cdot \theta)$  (with  $K$  defined by Eq. 4.10). for the SWNT-based solar cells.

This is the consequence of the fact that in SWNT thin films the complex portion of  $\varepsilon$  increases with  $\theta$  because at visible photon energies,  $\varepsilon_{//} > \varepsilon_{\perp}$ . This optical anisotropy has been studied in detail in our group by Dr. Giovanni Fanchini. The derivation for determining  $\varepsilon_{//} > \varepsilon_{\perp}$  is complex and not directly related to the main topic of this thesis and therefore not included here. The experimental and theoretical work confirming the anisotropic nature of SWNT thin films has been described in a manuscript<sup>48</sup> which is presently under consideration for publication and can be referred to for further information.

#### 4.6 Hole Mobility

The use of SWNT thin films as a hole collecting electrode in OPVs yielded efficiencies higher than ITO reference devices most likely due to increased exciton formation and charge collection resulting from the interpenetration of the P3HT:PCBM composite into the voids of the 3D SWNT network. While P3HT has a reasonably high hole mobility of  $\sim 10^{-3} \text{ cm}^2/\text{V s}$ <sup>49</sup> and a field effect mobility of  $\sim 10^{-1} \text{ cm}^2/\text{V s}$ <sup>50, 51</sup>,



SWNT thin films have been shown to have a field effect mobility of  $\sim 10 \text{ cm}^2/\text{V s}$  for low density networks ( $\sim 1 \text{ } \mu\text{m}^{-2}$ ) and  $>100 \text{ cm}^2/\text{V s}$  for higher density networks ( $\sim 10 \text{ } \mu\text{m}^{-2}$ ).<sup>12</sup> Thus, the interpenetration of the P3HT:PCBM into the SWNT network should improve the transport properties of the OPV through increased hole mobility and may contribute to the results described in Section 4.4.

To measure the hole mobility of SWNT/P3HT:PCBM layers, hole injection only ITO/SWNT/P3HT:PCBM/Au devices were fabricated. This was done by drop casting a 2.5 g/L P3HT:PCBM 1:1 chlorobenzene solution on 30, 40 and 50 mL SWNT thin films, and on ITO (for reference). Gold contacts (cathode) with an area of  $0.24 \text{ cm}^2$  were sputtered on top of the devices. The work function of gold (5.1 eV) in relation to the LUMO (3.75 eV) of PCBM creates a barrier height of 1.35 eV, which prevents electron injection. Alternately, the barrier height between ITO and the HOMO of P3HT is less than 0.5 eV. Thus, only holes are injected into the P3HT:PCBM and are the majority charge carriers in this configuration. The devices were annealed and processed in the same manner as described in Chapters 2 and 3. Figure 4.24 shows the current-voltage ( $J$ - $V$ ) relation for these devices. It can be seen that at low voltage ( $0.1 \text{ V} < V < 1 \text{ V}$ ), the  $J$ - $V$  relationship is ohmic ( $J \propto V$ ) as indicated by the dotted line with a slope close to one in Figure 4.24. The dotted line fit can be represented by Eq. 4.12 and often occurs at low bias since the low density of injected holes has a negligible influence on the induced field in comparison to the applied voltage.<sup>44, 52, 53</sup> The ohmic trend is represented by:

$$J_{ohm} = qn_p\mu\frac{V}{d} \quad \text{Eq. 4.12}$$

Where  $J_{Ohm}$  is the current density,  $q$  is the charge of the carriers,  $n_p$  is the density of the holes ( $\text{cm}^{-3}$ ),  $\mu$  is the mobility of the carriers,  $V$  is the applied voltage and  $d$  is the thickness of the P3HT:PCBM layer.

As the voltage is increased, the number of injected holes increases so that the field induced by the holes is substantial compared to the applied bias. In this voltage region, ( $1 \text{ V} < V < 3 \text{ V}$ ), the current is limited by the space-charge (SCLC) in the material so that the  $J$ – $V$  characteristics in Figure 4.24 are better described by the Mott-Gurney square law<sup>52, 54</sup> (also known as Child's law for solids – see derivation and explanation in Appendix B):

$$J_{SCL} = \frac{9}{8} \varepsilon_0 \varepsilon \theta \mu_h \frac{V^2}{d^3} \quad \text{Eq. 4.13}$$

where  $\varepsilon \approx 3$  is the relative dielectric constant of the organic film,  $\varepsilon_0$  is the vacuum dielectric constant,  $\mu_h$  is the hole mobility,  $\theta$  is the trapping factor, and  $d = 800 \text{ nm}$  is the polymer film thickness measured by SEM.

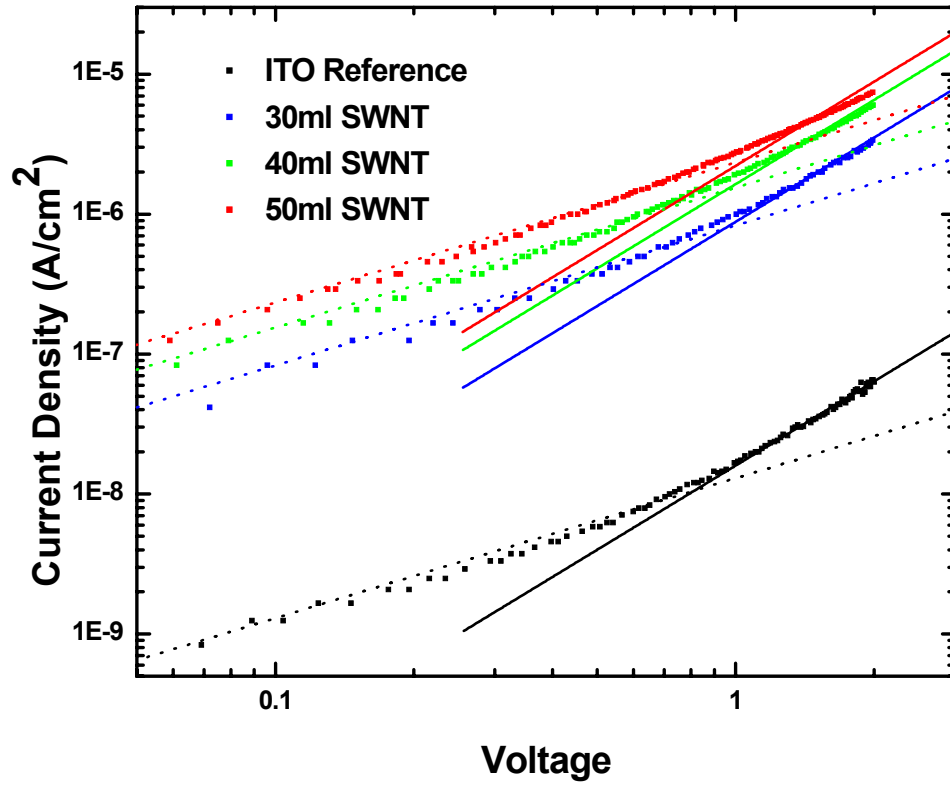


**Figure 4.24** Log-log plot of the J-V characteristics of hole injection P3HT:PCBM devices with the incorporation of SWNT networks on ITO and ITO only.

Assuming  $\theta = 1$  (trap free), we obtain  $\mu_h = 2.72 \times 10^{-6} \text{ cm}^2/\text{V}\cdot\text{s}$  for P3HT:PCBM, in agreement with values reported in the literature for devices of similar thickness and optimization.<sup>44</sup> In the case of SWNT-P3HT:PCBM devices we obtain mobility values that are approximately two orders of magnitude higher as shown in Table 4.2. In addition, we observe an increase in the mobility with SWNT film thickness. It must be noted that our experimental set up did not allow measurements beyond 2V which is not ideal as SCLC becomes more prominent at  $\sim 3\text{V}$ . Nevertheless, as demonstrated by the solid line (slope = 2) in Figure 4.24, 2V adequately demonstrates the transition from

ohmic behavior to the space-charge limited regime. It should also be noted that the calculated hole mobility values were based on the assumption that the films were trap free (that is,  $\theta=1$ ), unrealistic for solution processed materials. For the purposes of determining the mobility, and more importantly the variation in mobility amongst the devices, this assumption is reasonable. The presence of traps has a greater impact on the transition voltage from ohmic to the space-charge limited regime, rather than on the mobility values.

**Table 4.2** Hole mobilities for P3HT:PCBM with SWNT network electrodes and ITO reference electrodes.

	Reference	30 ml	40 ml	50 ml
$\mu_h$ (cm <sup>2</sup> /Vs)	$2.72 \times 10^{-6}$	$1.49 \times 10^{-4}$	$2.81 \times 10^{-4}$	$3.78 \times 10^{-4}$

## 4.7 Conclusions

The unique electronic structure of single walled carbon nanotubes (SWNTs) allow them to be utilized in a variety of applications. Processing SWNTs by purifying, dispersing and depositing them as networks or thin films onto substrates allows them to be transparent and conducting. Furthermore, by controlling the density of SWNT networks on substrates, it is possible to tune their optoelectronic properties. The results presented in this Chapter suggest that SWNT thin films can be used as the transparent and conducting hole collecting electrode in OPVs. The interpenetration of the P3HT:PCBM nanocomposite in the 3D network of SWNTs may be a source of further improvement in OPV characteristics as a result of improved hole collection resulting from exciton dissociation occurring closer to a nanocomposite-SWNT interface and improved hole transport through the matrix itself. Since the transmission and conductivity of the SWNT thin films can easily be varied as a function of network density, and since the work function of SWNTs has been reported to be between 4.5 and 5 eV, SWNT thin films are a promising alternative to ITO, especially for use in flexible electronic devices where solution deposition allow for the processing of thermally sensitive substrates.

## 4.8 References

- 1 2007 U.S. Geological Survey Mineral Commodity Summary.
- 2 [http://en.wikipedia.org/wiki/Solar\\_cell](http://en.wikipedia.org/wiki/Solar_cell).
- 3 C. M. Aguirre, S. Auvray, S. Pigeon, et al., Applied Physics Letters **88**, 183104 (2006).
- 4 Artukovic, E, Kaempgen, et al., Nano Letters **5**, 757 (2005).
- 5 A. Du Pasquier, H. E. Unalan, A. Kanwal, et al., Applied Physics Letters **87** (2005).
- 6 Hu, L, Hecht, et al., Nano Letters **4**, 2513 (2004).
- 7 K. Lee, Z. Wu, Z. Chen, et al., Nano Lett. **4**, 911 (2004).
- 8 J. Li, L. Hu, L. Wang, et al., Nano Lett. **6**, 2472 (2006).
- 9 M. W. Rowell, M. A. Topinka, M. D. McGehee, et al., Applied Physics Letters **88**, 233506 (2006).
- 10 N. Saran, K. Parikh, D. S. Suh, et al., J. Am. Chem. Soc. **126**, 4462 (2004).
- 11 E. S. Snow, P. M. Campbell, M. G. Ancona, et al., Applied Physics Letters **86**, 033105 (2005).
- 12 E. S. Snow, J. P. Novak, P. M. Campbell, et al., Applied Physics Letters **82**, 2145 (2003).
- 13 H. E. Unalan, G. Fanchini, A. Kanwal, et al., Nano Lett. **6**, 677 (2006).
- 14 Z. Wu, Z. Chen, X. Du, et al., Science **305**, 1273 (2004).
- 15 D. Zhang, K. Ryu, X. Liu, et al., Nano Letters **6**, 1880 (2006).
- 16 Y. Zhou, A. Gaur, S. H. Hur, et al., Nano Lett. **4**, 2031 (2004).
- 17 S. Iijima, Nature **354**, 56 (1991).
- 18 S. Iijima and T. Ichihashi, Nature **363**, 603 (1993).
- 19 D. S. Bethune, C. H. Kiang, M. S. Devries, et al., Nature **363**, 605 (1993).
- 20 M. S. Dresselhaus, G. Dresselhaus, and P. C. Eklund, *Science of Fullerenes and Carbon Nanotubes* (Academic Press, San Diego, 1996).

- 21 R. Saito, G. Dresselhaus, and M. S. Dresselhaus, *Physical Properties of Carbon Nanotubes* (Imperial College Press, London, 1998).
- 22 J. W. G. Wildoer, L. C. Venema, A. G. Rinzler, et al., *Nature* **391**, 59 (1998).
- 23 R. Saito, M. Fujita, G. Dresselhaus, et al., *Applied Physics Letters* **60**, 2204 (1992).
- 24 L. C. Venema, *Electronic Structure of Carbon Nanotubes* (Ios Pr Inc, 1995).
- 25 A. K. Geim and K. S. Novoselov, *Nature Materials* **6**, 183 (2007).
- 26 H. E. Unalan, Ph.D. thesis, Department of Materials Science and Engineering, Rutgers University, 2006
- 27 N. Hamada, S.-i. Sawada, and A. Oshiyama, *Physical Review Letters* **68**, 1579 (1992).
- 28 G. Li, V. Shrotriya, J. S. Huang, et al., *Nature Materials* **4**, 864 (2005).
- 29 E. Pop, D. Mann, J. Reifenberg, et al., *Intl. Electron Devices Meeting*, 253 (2005).
- 30 S. J. Tans, A. R. M. Verschueren, and C. Dekker, *Nature* **393**, 49 (1998).
- 31 M. J. Bronikowski, P. A. Willis, D. T. Colbert, et al., *Journal of Vacuum Science & Technology a-Vacuum Surfaces and Films* **19**, 1800 (2001).
- 32 A. Thess, R. Lee, P. Nikolaev, et al., *Science* **273**, 483 (1996).
- 33 Y. Zhou, L. Hu, and G. Grüner, *Applied Physics Letters* **88** (2006).
- 34 C. Journet, W. K. Maser, P. Bernier, et al., *Nature* **388**, 756 (1997).
- 35 W. Zhou, Y. H. Ooi, R. Russo, et al., *Chemical Physics Letters* **350**, 6 (2001).
- 36 M. A. Meitl, Y. X. Zhou, A. Gaur, et al., *Nano Letters* **4**, 1643 (2004).
- 37 M. F. Islam, E. Rojas, D. M. Bergey, et al., *Nano Lett.* **3**, 269 (2003).
- 38 M. D. Lay, J. P. Novak, and E. S. Snow, *Nano Lett.* **4**, 603 (2004).
- 39 M. J. O'Connell, S. M. Bachilo, C. B. Huffman, et al., *Science* **297**, 593 (2002).
- 40 C. Richard, F. Balavoine, P. Schultz, et al., *Science* **300**, 775 (2003).
- 41 ESD STM 11.11-2001 Standard. Surface resistance measurement of static dissipative planar materials, 2001.

- 42 J. Xue, S. Uchida, B. P. Rand, et al., *Applied Physics Letters* **84**, 3013 (2004).
- 43 M. Al-Ibrahim, S. Sensfuss, J. Uziel, et al., *Solar Energy Materials and Solar Cells* **85**, 277 (2005).
- 44 D. Chirvase, Z. Chiguvare, M. Knipper, et al., *Synthetic Metals* **138**, 299 (2003).
- 45 B. J. Landi, S. L. Castro, H. J. Ruf, et al., *Solar Energy Materials and Solar Cells* **87**, 733 (2005).
- 46 G. Fanchini, H. E. Unalan, and M. Chhowalla, *Applied Physics Letters* **88**, 191919 (2006).
- 47 B. B. Parekh, G. Fanchini, G. Eda, et al., *Applied Physics Letters* **90**, 121913 (2007).
- 48 G. Fanchini, S. Miller, B. B. Parekh, et al., Submitted for consideration.
- 49 S. S. Pandey, W. Takashima, S. Nagamatsu, et al., *Japanese Journal of Applied Physics* **39**, L94 (2000).
- 50 Z. Bao, A. Dodabalapur, and A. J. Lovinger, *Applied Physics Letters* **69**, 4108 (1996).
- 51 H. Sirringhaus, P. J. Brown, R. H. Friend, et al., *Nature* **401**, 685 (1999).
- 52 L. A. Dissado and J. C. Fothergill, *Electrical Degradation and Breakdown in Polymers* (Peter Peregrinus Ltd., London, 1992).
- 53 A. Rose, *Physical Review* **97**, 1538 (1955).
- 54 N. F. Mott and R. W. Gurney, *Electronic Processes in Ionic Crystals* (Oxford University Press, New York, 1940).



## Chapter 5

### Conclusions and Future Work

#### 5.1 Conclusions

Organic photovoltaics (OPVs) have shown great promise as a source of inexpensive renewable energy because the photoactive components can be deposited from solution utilizing inexpensive methods such as spin and roll coating. To date, however, thermal annealing is required to fully optimize the morphology of the photoactive components in solar cells. Further, other components in OPVs, such as the transparent and conducting electrode require expensive materials and processes to fabricate, and are not well suited for low temperature substrates and flexible applications. The primary objective of the research conducted in this dissertation was to move towards a truly flexible OPV device processed entirely at room temperature.

The basic materials and processing techniques required to fabricate flexible OPVs at room temperature have been developed and are described. A method for quickly and effectively fabricating and characterizing poly(3-hexylthiophene):phenyl-C<sub>61</sub>-butyric acid methyl ester (P3HT:PCBM) OPVs was also developed and described in this thesis. Specifically, the main discoveries of the dissertation are the use of solvent vapor annealing at room temperature to enhance the performance of OPV devices and the replacement of indium tin oxide (ITO) with transparent and conducting SWNT thin films as the hole collecting electrode. Both of these discoveries will bring the goal of room temperature processed, inexpensive and flexible OPVs closer to reality. The specifics of the contributions of this work towards meeting the above mentioned objective are described in detail in Chapters 2, 3 and 4. Here, we summarize the most

important conclusions from each of the chapters and provide details of additional work required to achieve the objective.

- **Use of gallium-indium (Ga-In) electrodes in OPVs (Chapter 2):** The use of Ga-In eutectic as an electrode in P3HT:PCBM OPVs was demonstrated. With a melting temperature of 15.7°C, Ga-In eutectic is a liquid at room temperature which allows it to be rapidly applied to devices without the need for vacuum equipment. Further, Ga-In eutectic has a work function of  $\sim 4.2$  eV, which is very close to that of aluminum, making it ideal for use as the electron collecting electrode. The use of an o-ring for containment of the electrode allowed for easy adjustment of the device area which is dictated by the electrode area and allowed for the rapid fabrication and testing of OPV devices.
- **Halogen lamp in place of solar simulator (Chapter 2):** In lieu of an expensive solar simulator, a special apparatus (developed in Professor Aurelien Du Pasquier's laboratory), using an inexpensive halogen light source and incorporating the Ga-In eutectic electrodes described above, was used to rapidly characterize P3HT:PCBM OPVs. A method to correct for the spectral mismatch between the solar spectrum and the halogen light was proposed and utilized. Baseline processing parameters for the fabrication of P3HT:PCBM OPVs were also established.
- **Solvent-vapor annealing to optimize the structure of P3HT:PCBM OPVs (Chapter 3):** In Chapter 2, the importance of thermal annealing as a method for optimizing P3HT:PCBM was demonstrated. However, as one of the objectives of this thesis was to move towards the development of a truly flexible photovoltaic

device, thermal annealing is not ideal because it may damage inexpensive, flexible substrates. Thus, as an alternative to thermal annealing, the improvement of photovoltaic efficiency via exposure of organic P3HT:PCBM devices to solvent vapor at room temperature was demonstrated. *In situ* photoluminescence (PL) and Raman spectroscopy, in conjunction with *ex situ* optical absorption and atomic force microscopy, were used to provide insight into the nanoscale morphological changes which occur during solvent vapor annealing. It was found that in 1:1 composites of P3HT:PCBM, suppression of PL, narrowing in line-width of the  $1442\text{ cm}^{-1}$  P3HT Raman peak, and strong modifications in the optical absorption spectra were observed during solvent vapor annealing, while minimal changes occurred in pure P3HT films. The spectral modifications were attributed to de-mixing of PCBM and subsequent stacking of P3HT in coplanar conjugated segments, similar to what is observed during thermal annealing.

- **SWNT thin films (Chapter 4):** The transparent and conducting hole collecting electrode is an integral component in OPVs, as well other optoelectronic devices. The current standard in transparent and conducting electrodes is indium tin oxide (ITO), which is expensive and inflexible. SWNT thin films, which are transparent and conducting, were deposited using a solution based vacuum filtration method. By varying the density of SWNTs in the 3D network, conductivity and transparency of the thin films were controlled. A resistivity of  $178\ \Omega/\square$  was achieved, which is of the same order as that of ITO ( $\sim 25\ \Omega/\square$ ). Because a transparent and conductive SWNT thin film utilizes a very low volume

fraction of SWNTs and is entirely solution processible, it is expected to be relatively inexpensive in the long run compared to ITO.

- **SWNT thin films in organic photovoltaic devices (Chapter 4):** P3HT:PCBM OPVs utilizing SWNT thin films as transparent and conducting electrodes for hole collection were fabricated and characterized. A power conversion efficiency of  $\sim 1\%$ , with a fill factor of 0.3 and a short-circuit current of  $6.5 \text{ mA/cm}^2$  under  $100 \text{ mW/cm}^2$  halogen light source was achieved. These values are comparatively higher than reference cells of similar thickness made on ITO-glass substrates. This is attributed to the three-dimensional nature of the interface between the SWNTs and the P3HT:PCBM nanocomposite. Additionally, the hole mobility of P3HT:PCBM was shown to improve from  $\sim 10^{-6} \text{ cm}^2/\text{Vs}$  on ITO alone to  $\sim 10^{-4} \text{ cm}^2/\text{Vs}$  because the P3HT:PCBM interpenetrates the 3D SWNT network reducing the hole diffusion length. Our results indicate that solution processed SWNT thin films are a viable alternative to ITO for photovoltaic devices, eliminating an expensive vacuum deposition step in the fabrication of organic solar cells.

## 5.2 Suggestions for Future Research

- **Functionalized SWNT thin films:** A precise explanation for the origin of the open-circuit voltage in P3HT:PCBM OPVs, and in similar systems, has not been developed. A partial explanation may be the difference in the workfunctions of the electrodes (see Section 1.2.4.2 in Chapter 1). By attaching different functional groups, such as bromine and chlorine, to SWNTs it may be possible to vary the workfunction of SWNT thin films. A detailed analysis of the SWNT thin film

workfunction should be made using Kelvin probe microscopy. The inclusion of functionalized SWNT thin films with varying workfunctions, as the hole collecting electrode, in OPVs could then lead to a better understanding of the origin of the open-circuit voltage.

- **Hole mobility measurements:** By measuring the current-voltage (I-V) characteristics of a semi-conductor when currents are space charge limited, useful information such as charge carrier mobility and concentration can be extrapolated. A major limitation of the work performed in this thesis was the ability to measure I-V characteristics well into the space charge limited regime. The hole mobility for SWNT/P3HT films should be determined using the space charge limited model for both thermally and solvent vapor annealed films. This may give further insight in to the origin of efficiency improvements from the use of SWNT thin film electrodes in OPVs.
- **Time-resolved photoluminescence (PL) measurements:** A detailed understanding of the recombination and charge transfer mechanisms are especially important in understanding the optoelectronic properties of OPVs. Another major limitation of this work was the ability to make time-resolved photoluminescence measurements necessary to understand the dynamics of photoexcited carriers in the P3HT:PCBM system. A detailed time-resolved PL study of this system, varying the component concentrations and annealing methods (thermal and solvent vapor), should be undertaken. By measuring the radiative recombination lifetime of photogenerated excitons under various morphological conditions, a greater understanding of the optimal P3HT:PCBM

processing conditions may be achieved. In conjunction with a thorough understanding of the charge carrier mobility (see previous bullet), time-resolved PL measurements will help discern improvements in OPV performance resulting from improved charge carrier generation versus those from improved charge transport.

- **Solvent vapor annealing with different solvents:** Solvent vapor annealing was shown to improve the characteristics of P3HT:PCBM OPVs in Chapter 3. However, this work was limited to the use of chloroform and chlorobenzene for solvent vapor. The perceivable difference between the two was chloroform tended to anneal slightly faster. Since regioregular P3HT tends to coplanar stacking (and, hence, demixing of the PCBM), the size of the solvent molecule and vapor pressure may effect the ability of a particular solvent to intercalate into the matrix and allow this morphology to develop. The very high vapor pressure and small molecular size of chloroform in contrast with chlorobenzene would support this. Many other solvents, including toluene, dichlorobenzene and xylene, have been used as solvents for the deposition of P3HT:PCBM and may produce similar annealing effects as chloroform and chlorobenzene. Detailed *in-* and *ex-situ* studies, similar to the one reported in Chapter 3, of other solvents should be conducted, considering the vapor pressure, the size of the solvent molecule and the resulting morphology. This may provide insight in to the mechanism by which solvent vapor annealing improves the performance of OPVs. In addition, the *in-situ* study in Chapter 3 should be repeated with different laser energies to obtain clearer values of the confinement parameter with annealing.

## Appendix A

### Tauc Method for Optical Band Gap Measurements

#### A.1 Tauc Gap and Tauc Plot

In Chapter 3 a Perkin-Elmer Lambda 20 transmittance spectrophotometer and Jobin-Yvon UVISEL spectral ellipsometer were utilized to obtain optoelectronic measurements of P3HT:PCBM composites. From these measurements, an estimate of the optical band gap using the Tauc method was obtained. While under certain conditions P3HT may be described as semi-crystalline, it lacks the long-range order associated with traditional crystalline materials. The summarization of the derivation of the Tauc gap which follows is based on the relaxation of basic assumptions used in explaining the optical properties of crystalline materials and provides a reasonable method for estimating the optical band gap of P3HT.

The complex index of refraction,  $N = n + ik$ , and the complex dielectric function,  $\varepsilon = \varepsilon_1 + i\varepsilon_2$ , where the refractive indices  $n$  and  $k$  and the dielectric constants  $\varepsilon_1$  and  $\varepsilon_2$  are real functions of the photon frequency,  $\omega$ , can be used to concisely describe the optical properties of an isotropic absorbing material. The dielectric constants and refractive indices are related to each other as follows:

$$\varepsilon_1 = n^2 - k^2, \quad \text{Eq. A.1}$$

$$\varepsilon_2 = 2nk \quad \text{Eq. A.2}$$

The optical properties of crystalline semiconductors can be explained in terms of one-electron excitations and assuming conservation of momentum. Similarly, the optical

properties of amorphous materials may be deduced from the general one-electron expression for the imaginary part of the dielectric constant:<sup>1-4</sup>

$$\omega^2 \varepsilon_2(\omega) = C \sum_i \sum_f \left| \langle f | P | i \rangle \right|^2 \delta(E_f - E_i - \hbar\omega) \quad \text{Eq. A.3}$$

Where  $P$  is the momentum operator and the sum is over all initial valence band states,  $i$ , and final conduction band states,  $f$ , separated by an energy gap  $\hbar\omega$ . Conservation of energy is described by the  $\delta$  function. Assuming a constant matrix element, this reduces to:

$$\omega^2 \varepsilon_2(\omega) = C \int_0^{\hbar\omega} g_c(E) g_v(E - \hbar\omega) d\omega \quad \text{Eq. A.4}$$

Where  $C$  is a constant, and  $g_c(E)$  and  $g_v(E - \hbar\omega)$  are the one-electron density of states of the conduction and valence bands, respectively. The assumption of  $k$  conservation is absent, as disorder in the system causing scattering is sufficient to create uncertainty in the momentum vector ( $\mathbf{k}$ ) of the electron. In order to solve the above integral, assumptions about the shapes of the valence and conduction bands must be made: if the density of states of the conduction band,  $g_c(E)$ , is featureless and considered a step function, then the integral depends on the density of valence band states.<sup>1,2</sup> Assuming the band edges are parabolic and thus the density of states have a square root energy dependence,<sup>1,2</sup> then Eq. A.4 reduces to:

$$\omega^2 \varepsilon_2(\omega) = B(\hbar\omega - E_0)^2 \quad \text{Eq. A.5}$$

where  $E_0$  is the optical band gap and  $B$  is a constant proportional to the joint density of states.

The absorption coefficient ( $\alpha$ ) as a function of the frequency can be stated as follows:



$$\alpha = \frac{4\pi k}{\lambda} = \frac{2\pi\epsilon_2(\omega)}{n\lambda} \quad \text{Eq. A.6}$$

By manipulating Eq. A.5 and Eq. A.6, the following relationship can be obtained:

$$\alpha\hbar\omega \propto (\hbar\omega - E_0)^2 \quad \text{Eq. A.7}$$

By plotting the square root of the product of the absorption coefficient and photon energy,  $(\hbar\omega\alpha)^{1/2}$ , versus  $E$ , the optical band gap may be estimated by fitting the linear region of the curve and intersecting the  $x$ -axis, where  $\alpha = 0$ , as shown in Figure A.1.

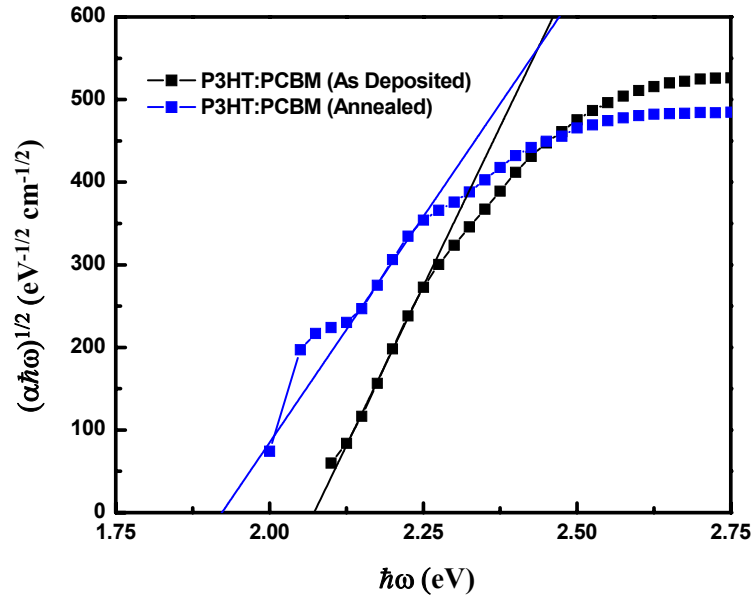


**Figure A.1** The dependence of  $(\alpha\hbar\omega)^{1/2}$  on photon energy for P3HT:PCBM from which the optical band gap is estimated. The  $x$ -intercept of the fitted line gives the optical band gap of the material.

The gap derived using equation Eq. A.7 is referred to as the Tauc gap and Figure A.1 is referred to as a Tauc plot.

## A.2 References

- <sup>1</sup> G. A. N. Connell, *Optical Properties of Amorphous Semiconductors* (Springer, Berlin, 1979).
- <sup>2</sup> N. Savvides, *Journal of Applied Physics* **59**, 4133 (1986).
- <sup>3</sup> J. Tauc, *Amorphous and Liquid Semiconductors* (Plenum Press, London, New York, 1974).
- <sup>4</sup> N. F. Mott and E. A. Davis, *Electronic Processes in Non-crystalline Materials* (Clarendon Press, Oxford, 1979).

## Appendix B

### Mott-Gurney Square Law (Child's Law for Solids)

#### B.1 Derivation of the Mott-Gurney Square Law

In Chapter 4, we used the space charge limited current (SCLC) relationship to extract the mobility of holes. Here, we describe the basis of the SCLC relationship. When bias applied to a bulk organic semiconductor is increased to the point that the density of injected holes is greater than the intrinsic density, the current flow through the material becomes space-charge-limited. This is the point where the charge from the holes becomes equivalent to the capacitance of the material times the applied bias. In such a case, assuming that the diffusion is negligible, trap density is low, contacts are ohmic and the mobility is field independent, the Mott-Gurney square law for SCLC can be derived as follows.<sup>1-3</sup>

Starting with the equation for the total current density, from drift, diffusion and displacement of carriers:

$$J = n_p e \mu E - e D_n \frac{dn}{dx} + \epsilon_0 \epsilon_r \frac{dE}{dt} \quad \text{Eq. B.1}$$

Where  $n_p$  is the hole density,  $\mu$  is the hole mobility,  $D_n$  is the diffusion coefficient for holes,  $\frac{dn}{dx}$  is the charge carrier density gradient through the material,  $\frac{dE}{dt}$  is the rate of change of the electric field, and other symbols have their usual meaning. Under steady-state conditions  $dE/dt = 0$  and Eq. B.1 can be reduced to:

$$J = n_p e \mu E - e D_n \frac{dn}{dx} \quad \text{Eq. B.2}$$

From Poisson's equation:

$$\frac{dE}{dx} = \frac{ne}{\varepsilon_0 \varepsilon_r} \quad \text{Eq. B.3}$$

Eq. B.2 can be manipulated to:

$$J = \varepsilon_0 \varepsilon_r \mu E \frac{dE}{dx} - \varepsilon_0 \varepsilon_r D_n \frac{d^2 E}{dx^2} \quad \text{Eq. B.4}$$

In the SCLC regime, the charge accumulation is assumed to be constant throughout the material and the electric field is substantial in relation to the field at the electrodes. Thus, the electric field is assumed to be constant across the material and the diffusion term can be neglected, resulting in:

$$J = \varepsilon_0 \varepsilon_r \mu E \frac{dE}{dx} \quad \text{Eq. B.5}$$

Rearranging the terms:

$$EdE = \frac{J}{\varepsilon_0 \varepsilon_r \mu} dx \quad \text{Eq. B.6}$$

Integrating both sides:

$$\int_0^E EdE = \frac{J}{\varepsilon_0 \varepsilon_r \mu} \int_0^x dx \quad \text{Eq. B.7}$$

Yields, after rearranging the terms:

$$E = \sqrt{\frac{2J}{\varepsilon_0 \varepsilon_r \mu}} x \quad \text{Eq. B.8}$$

Using the current density to voltage relationship,  $V = \int_0^d Edx$ , substituting Eq. B.8, and given material thickness,  $d$ , the following integral can be solved as:

$$V = \int_0^d \sqrt{\frac{2J}{\varepsilon_0 \varepsilon_r \mu}} x dx, \quad \text{Eq. B.9}$$

$$V = \frac{2}{3} \sqrt{\frac{2J}{\epsilon_0 \epsilon_r \mu}} d^{3/2} \quad \text{Eq. B.10}$$

Rearranging the terms results in the Mott-Gurney Law:

$$J_{SCL} = \frac{9}{8} \epsilon_0 \epsilon_r \mu \frac{V^2}{d^3} \quad \text{Eq. B.11}$$

## B.2 References

- <sup>1</sup> N. F. Mott and R. W. Gurney, *Electronic Processes in Ionic Crystals* (Oxford University Press, New York, 1940).
- <sup>2</sup> D. A. Clymer and M. A. Matin, in *Photonic Devices and Algorithms for Computing VII*, edited by K. M. Iftekharuddin and A. A. Awwal (SPIE, 2005), Vol. 5907, p. 219.
- <sup>3</sup> L. A. Dissado and J. C. Fothergill, *Electrical Degradation and Breakdown in Polymers* (Peter Peregrinus Ltd., London, 1992).

## Appendix C

### Procedures for the Fabrication and Characterization of P3HT:PCBM Organic Photovoltaic (OPV) Devices

#### C.1 Fabrication of P3HT:PCBM OPVs

Here we describe the basic procedure for the fabrication of P3HT:PCBM OPVs. The steps involved in this process include: 1) the cleaning and preparation of the substrate and bottom contact, 2) P3HT:PCBM solution preparation and deposition and 3) evaporation of the top contact. Cleanliness is always a factor in the performance of electronic devices. Therefore, gloves should always be worn during fabrication and testing. It should be noted that some of the procedures outlined in this appendix may differ slightly from those described in the chapters. These procedures represent those resulting in optimal results as of the writing of this thesis.

##### C.1.1 Cleaning and Preparation of the Substrate and Bottom Contact

The substrate and bottom contact material used in this work was polished float glass coated on one side with indium tin oxide (ITO) with a sheet resistance of  $\sim 15\Omega/\square$ . It was purchased from Delta Technologies, Ltd, part no. CG-61IN-S215, and comes in 50 x 75 mm sheets.

1. The ITO-glass should be carefully scored into 25 x 25 mm squares using a diamond scribe and a straight edge. The ITO-glass can then be broken along the scores.
2. To protect the integrity of the ITO, place substrate material in a glass Petri dish with the ITO side up. The ITO side can be determined by measuring the resistance using a multimeter.

3. Cover the substrates with HPLC grade acetone and bath sonicate for at least 5 minutes. Rinse the substrates with de-ionized (DI) water.
4. Cover the substrates with HPLC grade methanol and bath sonicate for at least 5 minutes. Rinse the substrates with DI water.
5. Dry the substrates with dry nitrogen gas.
6. Place 2 to 3 strips of Kapton (polyamide) tape, ~2 mm wide, on the ITO as shown in the figure below. Ensure the tape is firmly adhered to the ITO surface as it will act as a mask during the etching process.



7. Etch the exposed ITO by submerging the substrate in an aqueous solution of 20% HCl, 5% HNO<sub>3</sub> and a few drops of liquid detergent (to promote wetting) and heating to approximately 55°C. The exposed ITO layer should be removed in approximately 5 minutes, depending on the precise solution temperature. Substrates should be immediately rinsed thoroughly with DI water to remove excess acid.
8. Substrates should be cleaned again as described in steps 3 through 5 above.
9. Dry substrates in a vacuum oven at 110°C for 30 minutes.

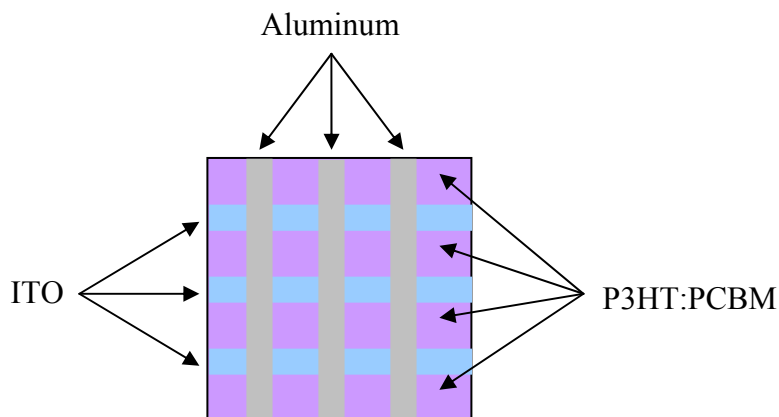
### C.1.2 P3HT:PCBM Solution Preparation and Deposition

1. Spin coat aqueous PEDOT:PSS solution (Baytron P from H.C. Starck, Inc.) at 3000 rpm for 180 seconds on the substrates (ITO side up!).
2. Allow the substrates to dry for 30 minutes at room temperature.
3. Place substrates in glove box ante-chamber and leave under vacuum for 30 minutes.
4. Dry substrates on a hot plate at 110°C in a nitrogen or argon filled glove box for 30 minutes.
5. Carefully weigh 10 mg of P3HT and 8-10 mg of PCBM. In the glove box, add the P3HT and PCBM to 1 ml of chlorobenzene in a small vial. Using a heat gun or hairdryer, warm (not too hot) the solution slightly to promote dissolution of the materials. Make sure the vial is tightly capped to prevent evaporation of the chlorobenzene.
6. Stir the contents using a magnetic stirrer on medium speed for 24 hours. Stirring in excess of 24 hours appears to result in the degradation of device performance.
7. Statically spin coat the P3HT:PCBM solution on the substrates at 600 rpm for 40 seconds.
8. Allow the samples to sit in the glove box for 1 day.
9. Thermally anneal the samples on a hot plate in the glove box at 140°C for 4 minutes.
10. Turn off the hot plate and allow the samples to cool for 1 hour. This prevents delamination of the P3HT:PCBM from the glass substrate.



### C.1.3 Evaporation of Top Contact

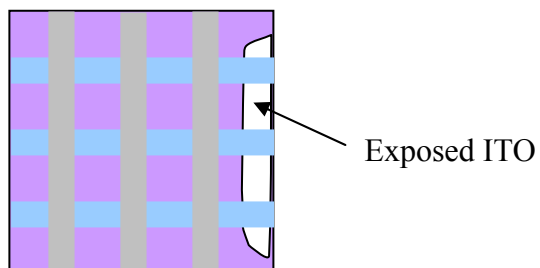
1. P3HT:PCBM OPVs are subject to degradation with time, and exposure to moisture and oxygen. Therefore, evaporation and testing of devices should be completed as soon as possible after cooling.
  2. Open the thermal evaporator and prepare it for the aluminum deposition.
  3. Place device (active side down) on the shadow mask for making strips. Orient the devices so the deposited aluminum will be perpendicular to the ITO strips.
- The final appearance of the device should as shown in the figure below.



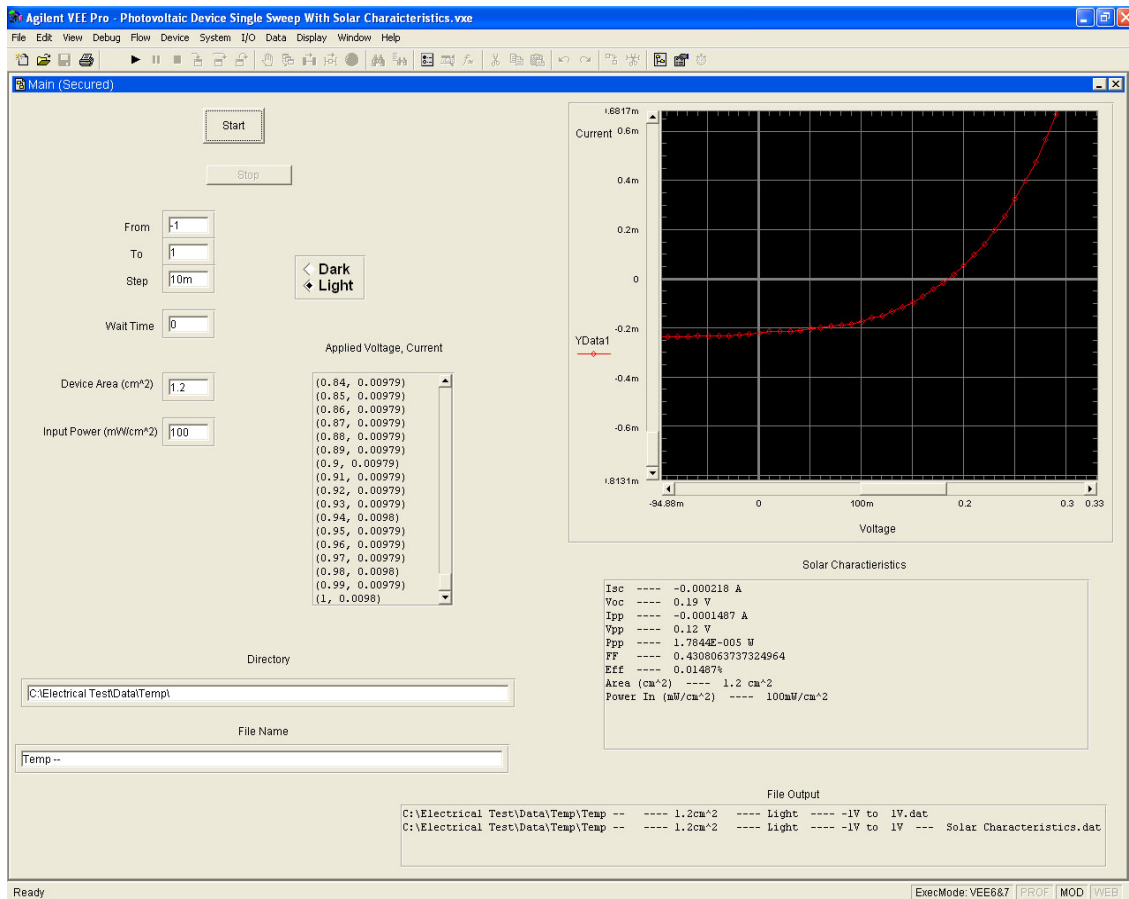
4. Pump down the evaporator until the pressure is  $\sim 10^{-6}$  torr.
5. Evaporate approximately 100nm of aluminum at a rate of no more than 1nm/sec to ensure a smooth film.
6. Remove the devices for testing.

### C.2 Characterization of P3HT:PCBM OPVs

1. The ITO strips will have a thin layer of P3HT:PCBM covering them. Using a q-tip dipped in chloroform, wipe away a small portion of the film exposing the ITO strips as shown in the figure below.



2. Align the device in the testing apparatus (see image at Appendix D.1) so each of the two metallic probes are in contact with an aluminum strip (cathode) and an ITO strip (anode).
3. Two cables should be connected to the HP 4140B pA meter/DC Voltage Source: one to the BNC connector labeled  $V_{\text{output}}$  and one to the BNC connector  $I_{\text{input}}$ . The  $V_{\text{output}}$  cable is then attached to the anode of the device and the  $I_{\text{input}}$  cable is attached to the cathode.
4. Turn on the solar simulator. Center the testing apparatus and device under the illumination spot from the solar simulator.
5. Open the photovoltaic testing program (written in Agilent VEE Pro). See screen image of program below.



Typical testing criteria are as follows, but may depend on device specifics:

From: -1V

To: +1V

Step: 10mV

Wait time: 0

Area: varies with each device

Input power: 100mW/cm<sup>2</sup> (one sun)

- Running the program will provide two files: one containing the current-voltage characteristics and one containing the efficiency, fill factor, short-circuit current and open-circuit voltage.

## Appendix D

### Equipment and Apparatus

The equipment used for the OPV work in this thesis was mostly commissioned and/or maintained by the author. All electronic test equipment was controlled with a computer via IEEE 488 interface (GPIB). Programs for the solar simulator and the current meter/DC voltage source were written in Agilent VEE Pro by Mr. Alokik Kanwal.

#### D.1 Solar Simulator



**Figure D.1** Newport solar simulator with AM 1.5 output up to  $200 \text{ mW/cm}^2$  (2 suns). A special apparatus was fabricated and affixed to a goniometer to facilitate testing of OPV devices.

## D.2 Current Meter/DC Voltage Source



**Figure D.2** Hewlett Packard 4140B pA Meter/DC Voltage Source used to apply bias to and measure current across OPV devices under light and dark conditions.

### D.3 Thermal Evaporator

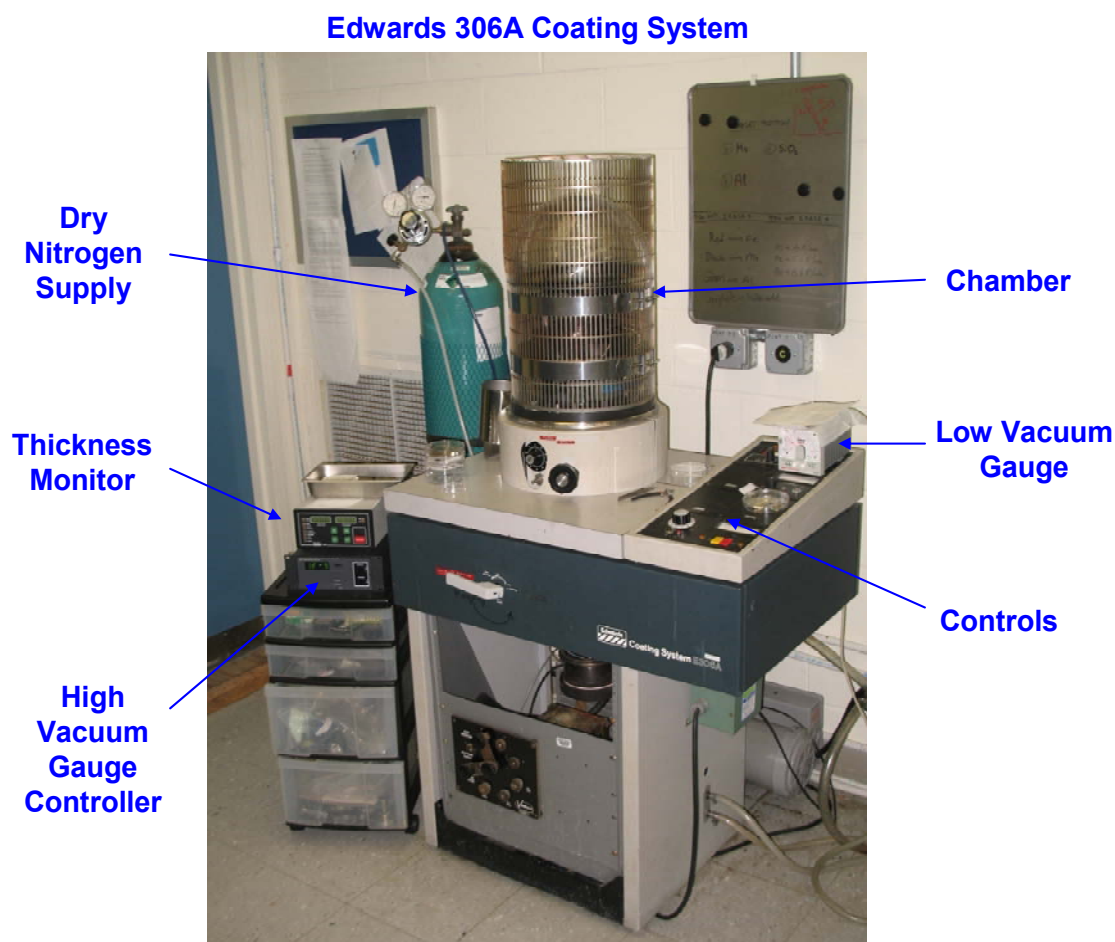


**Figure D.3** Edwards 306A Coating System (thermal evaporator) used to deposit aluminum contacts on OPV devices. It should be noted that this equipment was not working when acquired. It was completely rebuilt and commissioned by the author as part of the work contained in this dissertation.

#### D.4 External Quantum Efficiency Apparatus



**Figure D.4** External quantum efficiency apparatus utilizes monochromatic light to measure the incident photon to current conversion efficiency by wavelength.

## D.5 Glove Box

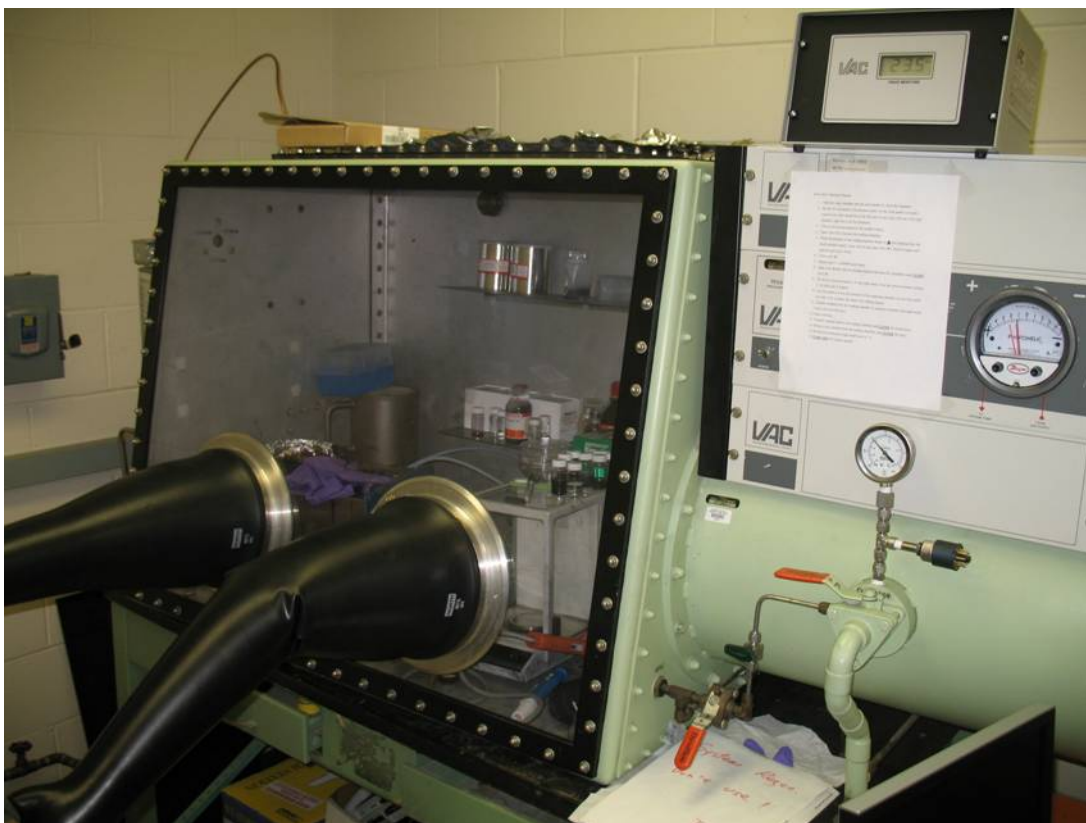


**Figure D.5** Nitrogen filled glove box used for the preparation of solutions, spin coating and annealing of OPV devices.



## D.6 Atomic Force Microscope



**Figure D.6** Digital Instruments Nanoscope IV atomic force microscope used to obtain height, amplitude and phase images of OPV device surfaces.

## Curriculum Vita

### Steven Lawrence Miller

#### Education:

2008	Ph.D. Expected, Materials Science and Engineering, Rutgers University
2006	M.S., Materials Science and Engineering, Rutgers University
2004	B.A., Physics (minor: mathematics), Rutgers University
1991	M.B.A., Finance/Accounting, University of California at Irvine
1987	B.A., Economics, University of California at Irvine

#### Work Experience:

2004-2007	Graduate Research Assistant, Department of Materials Science and Engineering, Rutgers University
2004-2007	Teaching Assistant, Department of Materials Science and Engineering, Rutgers University
1987-2004	Successful positions in finance and accounting. Certified Public Accountant in 1996.

#### Publications:

- A. Du Pasquier, H.E. Unalan, A. Kanwal, S. Miller, and M. Chhowalla, "Conducting and transparent single-wall carbon nanotube electrodes for polymer-fullerene solar cells," *Applied Physics Letters* **87**, 203511 (2005).
- A. Du Pasquier, S. Miller, and M. Chhowalla, "On the use of Ga-In eutectic and halogen light source for testing P3HT-PCBM organic solar cells," *Solar Energy Materials and Solar Cells* **90**, 1828 (2006).
- S. Miller, G. Fanchini, Y. Lin, C. Li, C. Chen, W. Su, and M. Chhowalla, "Investigation of nanoscale morphological changes in organic photovoltaics during solvent vapor annealing," *Journal of Materials Chemistry* **18**, 306 (2008).
- G. Fanchini, S. Miller, B. Parekh, and M. Chhowalla, "Optical anisotropy in transparent and conducting single-walled carbon nanotube thin films," Submitted for publication (2007).

V. Gupta, G. Fanchini, S. Miller, J. Al-Sharab, and M. Chhowalla, "Effect of Growth Parameters and Si-doping on Boron Carbide Nanostructures," Submitted for publication (2007).

G. Eda, Y. Lin, S. Miller, C. Chen, W. Su, and M. Chhowalla, "Transparent and Conducting Reduced Graphene Oxide Thin Films as Electrodes for Organic Photovoltaics," Submitted for publication (2008).